UNIVERSITÀ DEGLI STUDI DI CATANIA

IN CONVENZIONE CON

UNIVERSITÀ DEGLI STUDI DI PALERMO

DOTTORATO DI RICERCA IN

SCIENZA DEI MATERIALI E NANOTECNOLOGIE - XXXII CICLO

FABIO RICCO GALLUZZO

STUDY ON THE PERFORMANCE OPTIMIZATION OF THIN FILM SILICON AND BIFACIAL PHOTOVOLTAIC MODULES THROUGH OUTDOOR VARIABLES

TUTOR: PROF.SSA M. G. GRIMALDI

DOTT. S. A. LOMBARDO

COORDINATORE: PROF.SSA M. G. GRIMALDI

TESI PER IL CONSEGUIMENTO DEL TITOLO DI DOTTORE DI RICERCA

"If you can dream it, you can do it"

Walt Disney

IMM Institute for Microelectronics and Microsystems
Consiglio Nazionale delle Ricerche

UNIVERSITÀ DEGLI STUDI DI CATANIA

IN CONVENZIONE CON

UNIVERSITÀ DEGLI STUDI DI PALERMO

DOTTORATO DI RICERCA IN

SCIENZA DEI MATERIALI E NANOTECNOLOGIE - XXXII CICLO

FABIO RICCO GALLUZZO

STUDY ON THE PERFORMANCE OPTIMIZATION OF THIN FILM SILICON AND BIFACIAL PHOTOVOLTAIC MODULES THROUGH OUTDOOR VARIABLES

Abstract

Main object of this Ph.D. work has been the performance optimization of thin film Silicon and bifacial photovoltaic (PV) devices, by means of an in-depth study of their behavior by varying the outdoor variables affecting their electrical performance.

The first part of such work has been focused on the study of performance instability phenomena affecting tandem amorphous/microcrystalline Si mini - modules under variable working conditions in terms of illumination, voltage stresses (both in DC reverse bias and in direct bias in Maximum Power Point) and temperature. An accurate analysis of the causes of such phenomena has been carried out, by thoroughly studying the effects on the performance of such PV devices in actual outdoor operation, due to variations of

solar spectrum and of solar cell operating temperature. The relevant role played by the latter outdoor variable on the power conversion efficiency of such devices has been highlighted and demonstrated.

Considering the crucial importance which the study of electrical behavior of high efficiency bifacial PV devices is currently assuming, essentially due to the fast development and diffusion of such promising devices, the second part of this work has concerned the performance optimization of bifacial PV systems. For such purpose, a novel analytical model to accurately predict the electrical performance of bifacial PV modules, usable for any geographical location, has been developed and its accuracy validated through experimental tests outdoor. This has allowed, on one hand, to analyze in-depth the behavior of bifacial devices and their performance optimization, by varying the main outdoor variables which determines such performance in real operating conditions. On the other hand, it has been possible to predict the electricity generation of bifacial PV systems with and without solar trackers for different geographical locations, by highlighting whether and where the solar tracker adoption is convenient for optimizing the performance of these systems.

This Doctoral thesis consists of eight chapters, in which the main topics are treated as specified below.

Chapter 1 constitutes an introduction to such work. Initially, the crucial importance of the renewable energy sources' exploitation for a sustainable development is highlighted and discussed, by introducing the efforts made so far in such context and the future challenges. Subsequently, attention is paid to the photovoltaic technology, which is one of the most attractive and advanced renewable energy technologies. An overview on the current development and future perspectives of such technology is presented. Here, the different generations of PV devices available today (both in the market and at research and pre-commercial demonstration phase) are described, by highlighting the ones considered most promising. Afterwards, a focus is made on the PV devices which are the main subject of this thesis, namely tandem amorphous/microcrystalline Si solar cells and silicon based high efficiency bifacial solar cells. The main features of such devices and the related open issues are introduced. Finally, the motivations which have led to the present thesis study and what are its fundamental goals are described.

Chapter 2 summarizes the main findings of previous studies in the scientific literature regarding performance instability phenomena of amorphous silicon-based solar cells, in order to present an overview on this topic and facilitate the reading of the following chapter 3. After a focus on the well-known Staebler-Wronski Effect and on the main thermal effects able to influence the performance of the mentioned solar cells (by allowing their recovery/improvement), a synthesis of the already known basic dynamics allowing to improve the electrical performance of such cells is provided. In this regard, we focus on the effects (observed during experiments indoor) triggered by the application of DC reverse bias stresses to such PV cells under illumination. Finally, some instability effects observed on the mentioned devices, induced by solar spectrum variations, are illustrated.

Chapter 3 is focused on the results of new experimental activities, carried out in this work on tandem a-Si/μc-Si photovoltaic mini - modules, with the main goal of further investigating the performance instability

phenomena found in the literature on a-Si based solar cells (summarized in chapter 2). Firstly, we carefully explain the aims of such activities and we describe the experimental setups prepared and used, in addition to the experimental methods applied. Subsequently, the main findings of the experiments performed are highlighted and discussed in depth. Initially, we present the results of the experiments performed by subjecting different groups of specimens of the mentioned mini - modules to different reverse bias DC stress conditions (both outdoor under the sunlight, and indoor under the illumination provided by a solar simulator). Here we show the effects induced on the specimens by such stress conditions and we discuss on the convenience to apply them. Then, we show and discuss performance instability phenomena observed on stabilized specimens working outdoor in their Maximum Power Point, under variable temperature and illumination conditions. Finally, the causes of such phenomena are individuated and thoroughly analyzed, by studying the effects on the mini – modules performance induced by solar cell temperature and solar spectrum variations.

Chapter 4 outlines the major conclusions based on the experimental research activities carried out on tandem a-Si/μc-Si photovoltaic mini - modules, illustrated and discussed in the previous chapter 3. In particular, we focus on the relevant rule played by the PV cell temperature variations on the electrical performance of the mentioned devices, by highlighting the power conversion efficiency improvements due to the cell thermal annealing, obtainable in hot climates.

Chapter 5 concerns a state of the art regarding the modeling of bifacial photovoltaic devices performance and their behavior. An introductory section contains general considerations about the relevance of accurately predicting the electrical performance of the mentioned devices and illustrates the fundamental general structure of the main models so far proposed in the scientific literature. In the following sections, an overview regarding the optical, thermal and electrical modeling of bifacial solar devices is provided, as proposed in different studies in the literature. Contextually, the main findings of such studies, concerning the behavior foreseen for bifacial PV devices (by varying the main parameters able to affect their performance), are summarized. Finally, a focus is made on the accuracy so far achieved by the main models in the literature.

Chapter 6 is dedicated to the activities of development and experimental validation of a novel model for predicting the performance of bifacial photovoltaic module and to the presentation of the main simulation results provided by such model. Initially, the model proposed is described. Afterwards, the main validation results of such model are shown, by highlighting the very good agreement observed among the simulated results and the experimental ones (obtained by experiments performed outdoor in Sicily, on a bifacial Silicon mini - module consisting of four solar cells in series). Contextually, the results obtained by varying the main parameters affecting the electrical performance of a bifacial PV module (i.e. its elevation from the ground, its tilt angle, and the ground reflectivity) are illustrated and commented in detail.

Chapter 7 concerns the energy generation prediction of bifacial and mono-facial PV strings with and without solar tracker, installed at different geographical locations. Once the needed upgrades to the model presented in chapter 6 and the main assumptions for the calculation of the mentioned energy generation are

specified, the most relevant results provided by the model are presented and discussed. In particular, we present a detailed investigation on perimeter effects able to influence a bifacial PV string performance as well as on the effect induced by the latitude on such performance. Contextually, the convenience of adopting uniaxial horizontal solar tracker for the mentioned PV strings is investigated too.

Chapter 8, as conclusive section of this Doctoral thesis, summarizes the most relevant findings of such Ph.D. work, based on the global set of the experimental activities carried out, providing novel information to understand the electrical behavior both of tandem amorphous/microcrystalline silicon PV mini - modules and high efficiency silicon based bifacial PV devices and systems. Finally, some recommendations and possible future developments of this work are provided.

This work has been prevalently carried out in collaboration with the researchers of the Energy Conversion Device Group of CNR-IMM Catania Headquarter under the supervision of Dr. Salvatore Antonino Lombardo.

Concerning the PV devices manufacturing and providing, the research activity has benefited from the collaborations with Enel Green Power and in particular with the 3SUN R&D group leaded by Dr. Cosimo Gerardi.

The Ph.D. candidate Fabio Ricco Galluzzo, during the Ph.D. course, attended numerous educational and seminar activities on characterization techniques of materials and devices, both at the University of Catania and at the University of Palermo.

Acknowledgments

I would like to express my deepest gratitude to my tutor and coordinator of the Ph.D. course Prof. Maria Grazia Grimaldi and to my supervisor Dr. Salvatore A. Lombardo who guided me during the Ph.D. period, by making my intense research activity highly productive and stimulating.

The work described in this thesis was prevalently carried out in collaboration with the researchers of the Energy Conversion Device Group of CNR-IMM Catania Headquarter leaded by Dr. Salvatore A. Lombardo. A special thanks is so directed to such researchers.

My acknowledgments go also to Enel Green Power and in particular to the 3SUN R&D group leaded by Dr. Cosimo Gerardi, for manufacturing and providing the PV devices tested.

I would like to thank also all Laboratory of Optics and OptoelectroniX (LOOX) research team of the University of Palermo, with whom I also cooperated.

Moreover, a special thanks go to my friend and colleague Dr. Andrea Scuto, for its precious cooperation and sincere friendship.

At last but not least, I would like to express my heartfelt and deepest thanks to all my family and specially to my partner Marianna and my parents, for all their loving and patient support and encouragement.

I dedicate this work to my special grandmother, who has always believed in me and in my capabilities.

CONTENTS

CHAPTER 1 INTRODUCTION

1.1 Renewable energy: a need for sustainable development

Recently, the United Nations General Assembly (UN), by remarking the importance of the energy supply issue, unanimously has declared that the decade 2014-2024 must be the "*Decade of Sustainable Energy for All*", in order to ensure energy access at affordable prices, in a reliable and sustainable way for all [1].

Currently, a sustainable energy development is necessary to preserve the environment, by fighting the current climate changes due to the widespread use of fossil fuels as a main energy source, both for emerging countries, whose energy demand is growing rapidly and irrepressibly, and for economically developed countries.

Consistently with the *Paris Agreement* [2], the global warming limitation, in the perspective of containing dangerous and harmful effects related to climate change, imposes a rapid changing of the energy system, besides an adequate modification of the existing production and consumption models. In this scenario, an increase in the renewable energy sources exploitation gets a crucial importance for combating climate change. In fact, the increase in the renewable energy sources share allows to limit the use of non-renewable sources, in particular fossil fuels, for electricity and heat production, as well as in the transport sector, so that greenhouse gas emissions can be diminished overall [3].

Nowadays many related energy and climate policies exist to promote the evolution of low-carbon energy technologies, also with the goal of stimulating innovation in this sector. For instance, in the European context, the Directive 2009/28/EC [4] has set binding national targets to contribute to the overall objective of achieving 20% renewable energy by 2020, in the fulfillment of the European Union total energy needs. In such context, the largest European research and innovation program *Horizon 2020* [5] is born, in which among others the *Energy* area is included, by underlining the strategic importance of research and innovation in the energy field to achieve the goals set.

Recently, in June 2018, the European countries have reached an agreement for a more ambitious target, binding at European level and relating to renewable energy, of 32% at least of the gross final consumption, by 2030 [6].

It should be noted that, also thanks to the aforementioned climate and energy policies, Europe has historically played an important role in the use of renewable energy; however, this scenario could change soon, as a consequence of the greater investments for the "clean energy" sources exploitation which the

developing countries are doing, compared to those currently made by the most economically advanced countries.

In fig. 1.1 an overview of new global investments in renewable energy, for the years 2005-2017 and by considering different technologies, is shown. From this figure, we can observe that in recent years, the new investments in renewable energy have been dominated by those aimed at the solar energy exploitation (mainly to be converted into electricity via the PV technology); in particular, in 2017, investments in solar energy amounted to 57% of total investments in renewable energy, compared to 50% in 2016 [3],[7].

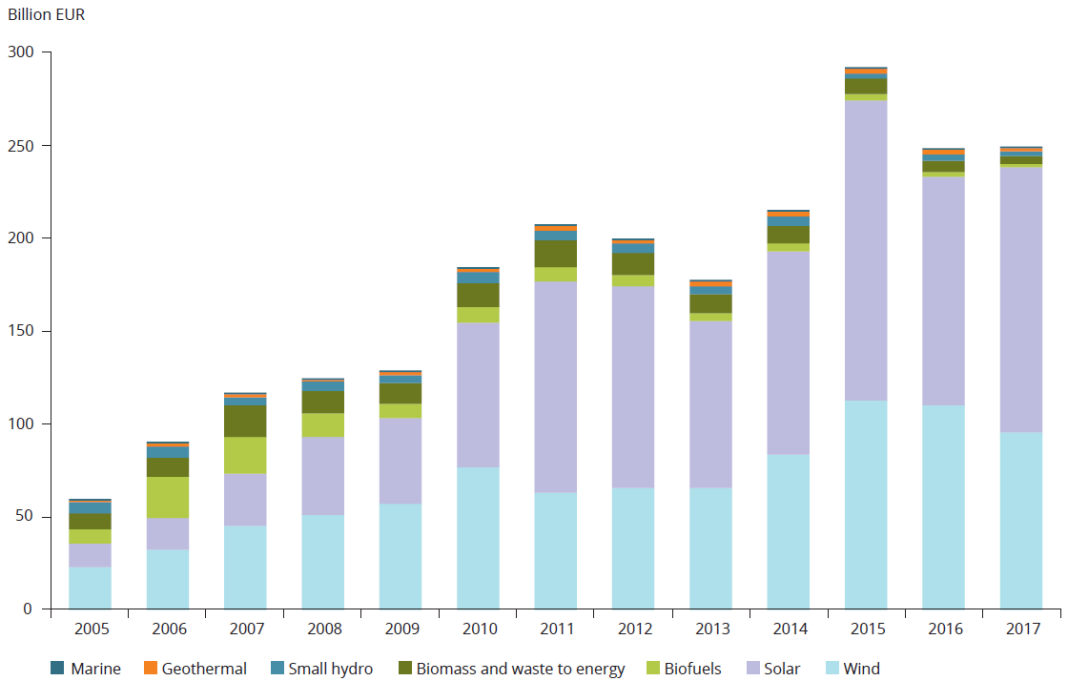

Fig. 1.1 - Overview of new global investments in renewable energy, by considering different technologies, from 2005 to 2017. Source: [7].

Although considerable efforts have been carried out so far to promote the exploitation of renewable sources for fulfilling the world energy needs (as it has been pointed out above), further efforts, both in terms of economic investments, and especially political, social and cultural commitment, have to be made to ensure a sustainable economic development, based on respect for the environment. Such efforts should be based on scientific research and constant technological innovation, mainly aimed at improvement and refinement of the existing energy conversion systems.

1.2 Photovoltaics: development and perspectives

In the last twenty years on a global scale a dizzy growth in the electricity generation from renewable sources has occurred, by achieving in 2017 an overall capacity of 2179 GW (with an increase of 166 GW, compared to 2016) [3]. Such growth has been due to both the increasing attention paid to the environmental pollution issues and related policies (as described in the previous section 1.1) and to the energy crisis, linked to the considerable reduction of fossil fuel reserves, and continuous increase in the electricity demand.

Among the different renewable sources usable for electricity generation, solar energy is of considerable interest; in fact, the sun is an important source of clean and renewable energy which does not alter the environmental balance, it is free, available everywhere and able to produce, in a single day, the energy used in the world in a whole year. However, it should be noted that to make competitive photovoltaic energy (namely, direct conversion of solar radiation into electricity), challenges still remain open. These challenges concern technical issues related to the uncertainty and low energy density of the solar source, in addition to low efficiency of the energy conversion systems available today.

Currently, photovoltaic (PV) technology is one of the most advanced renewable energy technologies and it is having significant growth worldwide, essentially as a consequence of considerable decrease in costs, economies of scale, in addition to opportunities for technological innovation.

In fig. 1.2, the growth in recent years, in terms of overall solar photovoltaic capacity in the European and world context, is remarked.

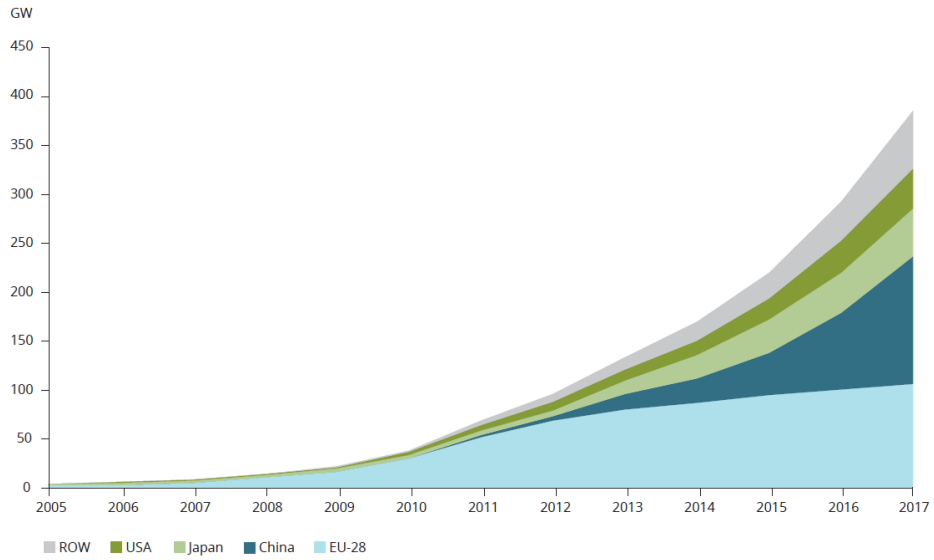

Fig. 1.2 - Increase observed in the period 2005-2017, in terms of overall PV capacity in the European context (EU-28), China, Japan, USA and the rest of the world (ROW). Source: [3], [8].

Consistently with recent scientific literature on various types of photovoltaic (PV) devices existing nowadays, with specific reference to materials used, commercial maturity and market penetration, essentially it is possible to identify three generations of PV devices, as listed below [9]:

- *first generation PV devices* which, to make p-n junctions, use the traditional crystalline silicon technology (based on the production of mono or multi-crystalline silicon wafers) and to date are widely available on the market;

- *second generation PV devices*, well known as "thin film devices" (by considering the thin layers of semiconductor material used, having a few micrometers thickness), which are currently spreading on the market;

- *third generation PV devices* which prevalently to date are at research and pre-commercial demonstration phase, although, in some cases, are starting to be commercialized.

It is probably useful to note that this classification begins to be outdated, and in some contexts the distinction among the three categories *bulk* (or *wafer based*), *thin film* e *novel concept* is preferred.

With reference to the development of first and second generation PV devices, it should be noted that those based on the crystalline silicon still dominate the market, even if in the last years an increasing diffusion of thin-film photovoltaic devices has been observed [10]. Although the latter devices have some positive aspects, such as reduced manufacturing costs and production possibilities as flexible and light structures, their power conversion efficiencies are currently lower than those of the most recently produced crystalline silicon devices (as it is possible to observe from Fig. 1.3).

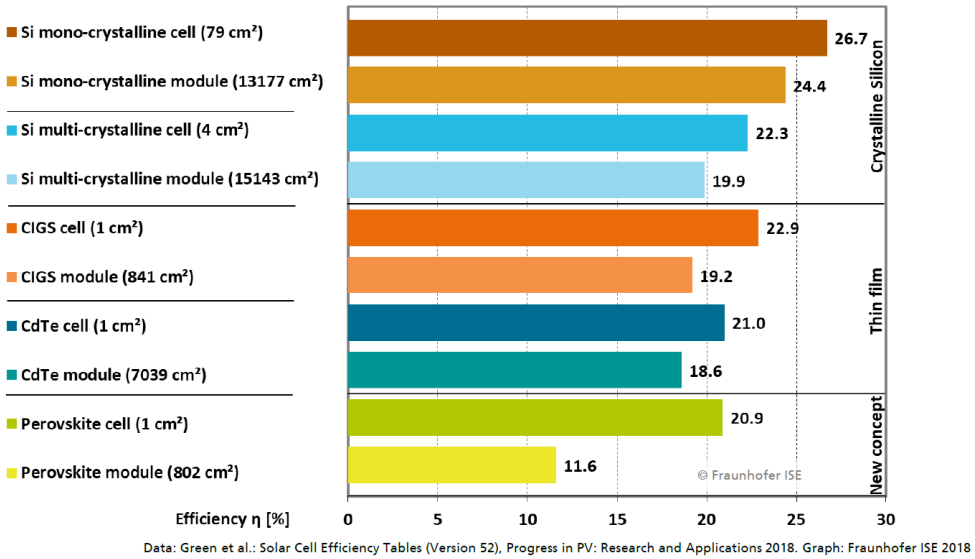

Fig. 1.3 – Comparison among power conversion efficiency values of different types of PV devices (by considering the best solar cells and modules developed in the labs). Source: [10], [11].

With reference to third generation PV devices, it should be noted that some of them, such as multi-junction solar cells, have allowed to achieve efficiency levels significantly higher than those of conventional crystalline silicon cells. Such a result has been achieved essentially thanks to the multi-

junction structure which makes it possible a solar spectrum splitting, with different wavelength ranges managed by different PV materials overlapped, and globally an exploitation of a wider range of the AM 1.5G solar spectrum, respect to a classic single-junction solar cell. In this regard, it is important to remember that, as it was calculated by C. H. Henry in 1980 [12], an ideal multi-junction cell structure with 36 energy gaps would achieve a maximum efficiency of 72%, at a concentration of 1000 suns with the cell at 300 K, which is considerably higher than the upper theoretical limit referred to the efficiency of a p-n single-junction solar cell, equals to 30%, as calculated in 1961 by William Shockley and Hans J. Queisser for an energy gap of 1.1 eV [13]. However, the multi-junction cells entail considerable production costs [9], [14]. Instead, other third generation PV devices, such as the so-called "dye-sensitized solar cells" and thin film kesterite / CZTS PV cells, seem to promise considerable savings on production costs, but currently they have quite low power conversion efficiencies [11], [15], [16]. Finally, it is noteworthy that in the context of *novel concept* PV devices, the so-called Perovskite solar cells are rapidly developing and promise the achievement of high conversion efficiencies at reduced costs, even if at the moment significant issues related to the stability of such cells remain [17].

The power conversion efficiency world record, above 26%, referring to a single cell based on the use of crystalline silicon, has been recently achieved in March 2017 [11]. Such an extraordinary result has been achieved through the so-called *HJ-IBC technology* ("*Silicon heterojunction solar cell with interdigitated back contacts"*) which, unlike conventional crystalline silicon cells, uses monocrystalline cells appropriately combined with amorphous silicon layers, by constructing on the cell rear side a particular pattern consisting of piles of amorphous silicon layers p + and n + suitably intercalated [18]. It is important to note here that such an efficiency record is almost 90% of the above mentioned upper theoretical Shockley-Queisser limit [13].

In this scenario, it is highly significant that new generation photovoltaic technologies are being developed on the basis of the "old" crystalline silicon. These technologies (among which for instance the cells known as PERC, n-PERT BJ, PERL[1] have also to be mentioned), have the common goal to significantly increase the device power conversion efficiency, by maintaining at the same time the cost-effectiveness linked to the prevalent use of well-established processes [19].

Recently, an increasing attention has been paid to silicon based high efficiency *bifacial solar cells and modules*, both from many world manufacturers of PV devices and from the scientific community, mainly as a consequence of the potential of such devices. In fact, they make it possible to generate more electricity respect to traditional mono-facial PV devices, essentially for the albedo radiation which is suitably collected and exploited by the bifacial solar cell rear side. It is interesting to note that, also if currently most of commercially available solar devices are of mono-facial type, according to [20], a

[1] acronyms of *"Passivated-Emitter and Rear Cell"*, *"n-type (Si) Passivated Emitter Rear Totally diffused Back-Junction"*, *"Passivated Emitter and Rear Locally-diffused"*, respectively.

considerable growth is foreseen in the bifacial devices market penetration, with a market share rise related to bifacial modules higher than 35% in 2028 (as shown in more detail in fig. 1.4).

In the next sections, an introduction will be presented regarding the PV devices which are the main subject of this thesis, namely tandem amorphous/microcrystalline Si solar cells (see section 1.3) and silicon based high efficiency bifacial solar cells (see section 1.4), by focusing on the main features of such devices and the related open issues.

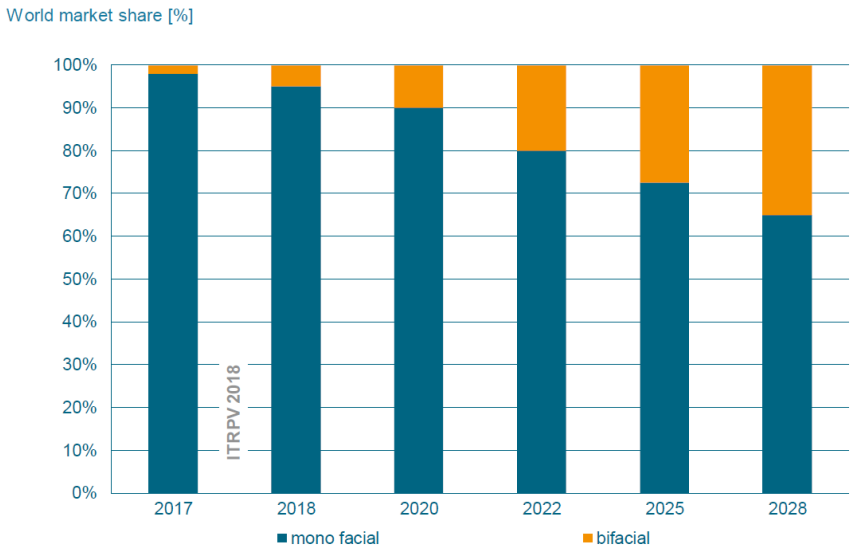

Fig. 1.4 – Current and foreseen global market shares of c-Si bifacial PV modules (equipped with bifacial solar cells and transparent back cover) and mono-facial modules. Source: [20].

1.3 Tandem amorphous/microcrystalline Si solar cells: main features and issues

Tandem amorphous/microcrystalline Si solar cells are a particularly interesting kind of thin-film PV devices, based on the use of amorphous silicon. As it is well-known, substantially the structure of such cells consists of a hydrogenated amorphous silicon (a-Si:H) solar cell overlapped to a microcrystalline Silicon (µc-Si) cell, by forming a multi-junction solar cell (according to the schematic representation in fig. 1.5).

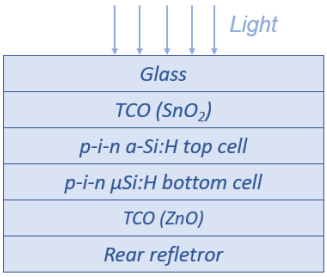

Fig. 1.5 - Schematic representation (layers' sequence) of a tandem amorphous/microcrystalline Si solar cell.

Typically, the intrinsic layer in the a-Si upper cell have a thickness of the order of few hundred nanometers, while the one in the µc-Si cell is about one thousand nanometers thick; furthermore, the a-

Si:H and μc-Si doped layers have a thickness of the order of some tens of nanometers. The Transparent Conductive Oxide (TCO) layer on the cell front side is designed so that the light transmittance is increased and the ZnO TCO layer on the cell rear side essentially allows a series resistance decrease and an improvement of the reflectivity at the cell rear side [21].

Basically, the main positive aspect of the abovementioned tandem structure, compared to the single-junction a-Si or μc-Si solar cell traditional structure, consists in the solar spectrum splitting, with the thin a-Si top cell absorbing the blue light portion of the spectrum and the thicker μc-Si bottom cell managing the red and infra-red light portions, so that globally a greater portion of the AM 1.5G solar spectrum can be exploited for the solar energy conversion into electricity.

A further important advantage of the tandem structure, respect to a conventional a-Si solar cell, is linked to the possibility to maintain, via suitable light trapping strategies, the amorphous silicon layer thin enough to allow, in addition to a manufacturing cost reduction, a limitation of the so-called "*LID"* (i.e. the *Light induced Degradation* effect[2]) which typically significantly affects a-Si PV devices.

It is important to note that, although the microcrystalline solar cell has a more stable behavior when it is exposed to light, in comparison with the upper a-Si:H cell [22], the latter is anyway subjected to the so called *Staebler-Wronski effect* [23]. As it is well-known from the literature, such an effect in the amorphous silicon based solar cells determines a performance worsening of the PV cell, consequently to its light exposure, which substantially involves a reduction of its overall power conversion efficiency, compared to the initial cell performance. Such a worsening is due to the so-called "dangling bond" defects, whose density increases compared to the initial one, as a main consequence of the solar cell light exposure. Nevertheless, the a-Si:H based solar cells have been a commercially practicable technological solution, since, via an adequate light soaking (i.e. a prolonged light exposure), it is possible to achieve a partial stabilization of the aforementioned defects concentration [24], [25].

Interesting recent studies in the literature [21], [26–31], carried out on non-stabilized samples of both single-junction solar cells and amorphous / microcrystalline silicon tandem cells, have allowed to demonstrate, via indoor tests, the following. As it will be described in detail in Chapter 2, by subjecting these cells to reverse bias DC stresses, under appropriate light and temperature conditions, it is possible to achieve, in addition to a slowdown of the cell aging kinetics, even an improvement of their performances, compared to those of the unstressed cell. Such a performance improvement has been observed in terms of solar cell main electrical parameters improvement, with evident increases in its overall power conversion efficiency. The improvement extent is a function of different factors and, in particular, depends on stress time, level of the stress voltage applied to the cell (hence intensity of the external electric field), irradiance level and cell temperature [27], [31].

[2] namely, the efficiency reduction related to light exposure of a solar cell.

It has been hypothesized that the observed performance improvements can be linked to a phenomenon of charged impurities (probably hydrogen ions) migration, induced by the external electric field applied, at the interface between the p type hydrogenated amorphous silicon layer and the TCO substrate of an a-Si:H solar cell. Substantially, such a migration phenomenon would be able to trigger variations in the defect state existing in the amorphous silicon layer [31]. Moreover, in the specific case of a-Si:H / μc-Si:H tandem cells, in whose structure an interface similar to the aforementioned type exists (see fig. 1.5), power conversion efficiency improvements can be explained as described below. The microcrystalline silicon layer constitutes a sort of hydrogen tank (since it contains a hydrogen density greater than that in the TCO layer), from which a migration of hydrogen ions towards the a-Si:H cell can be stimulate, by applying an external electric field, even with significantly lower intensity than that requested to induce similar performance benefits in an a-Si: H single-junction cell (see [21]).

Subsequent and more recent studies (which are one of the main subjects and advancements of this thesis work and whose findings will be illustrated and discussed in detail in Chapter 3) have been performed through tests, both outdoor and indoor, on a-Si:H / μc-Si:H mini - modules (for instance, see [32]); this latter studies have allowed to reveal important performance instability phenomena of such PV devices (both on non-stabilized and stabilized samples[3]) and to identify and analyze in depth the causes of the mentioned instability. In particular, tests carried out on non-stabilized samples subjected to reverse bias stresses under illumination have confirmed the benefits (in terms of electrical performance improvement) induced by such stresses, as well as it had already been observed on single solar cells. Finally, further tests performed outdoor on stabilized samples, exclusively working in their Maximum Power Point, have revealed systematic and significant improvements of their electric performance during the afternoon hours, as a main consequence of the thermal annealing at moderate temperatures of the samples tested during the morning. As it was remarked in some studies in the literature [33], [34], such a thermal annealing effect can lead to relevant benefits on the aforementioned device performance. Such benefits have led to consider this type of PV devices particularly suitable for the use in hot climates, where it is possible to take a significant advantage in terms of power conversion efficiency improvements by the thermal annealing of a-Si:H based solar cells.

1.4 Bifacial PV devices: an introduction

As it has been already underlined in section 1.2, currently a growing interest is aimed to the bifacial PV devices.

Although different thin-film solar cells can easily be manufactured as bifacial devices (see, for example [35], [36]), as a matter of fact, the c-Si based bifacial PV devices (i.e. those in which the

[3] (the stabilized samples are samples subjected in lab. to extended light soaking for one thousand hours, before that outdoor tests were performed on them).

crystalline silicon is used as a substrate) have had a greater attention and an increasing development. This is what occurred, essentially because of the following motivations. First of all, the high power conversion efficiency achievable with the latter devices and a relatively high compatibility, in terms of production processes, among conventional c-Si solar cells and bifacial ones; furthermore, the leading role still played by the silicon in the PV market [37], [38]. Moreover, as it has been recently highlighted by the International Technology Roadmap for Photovoltaic [20] (and partially shown in fig. 1.4), a significant permanent increase is expected in the world market share of crystalline silicon based bifacial PV devices, by achieving within the next ten years, market share percentages of almost 40% related to c-Si bifacial solar cells and about 35% referring to c-Si bifacial modules.

Basically, a c-Si bifacial solar cell can be schematically represented as shown in fig. 1.6 a, where we can observe the layers' sequence of a bifacial solar cell having a p-type c-Si substrate. Bifacial solar cells, with a similar structure but having a n-type c-Si substrate, are manufactured too (as an example, see fig. 1.6 b).

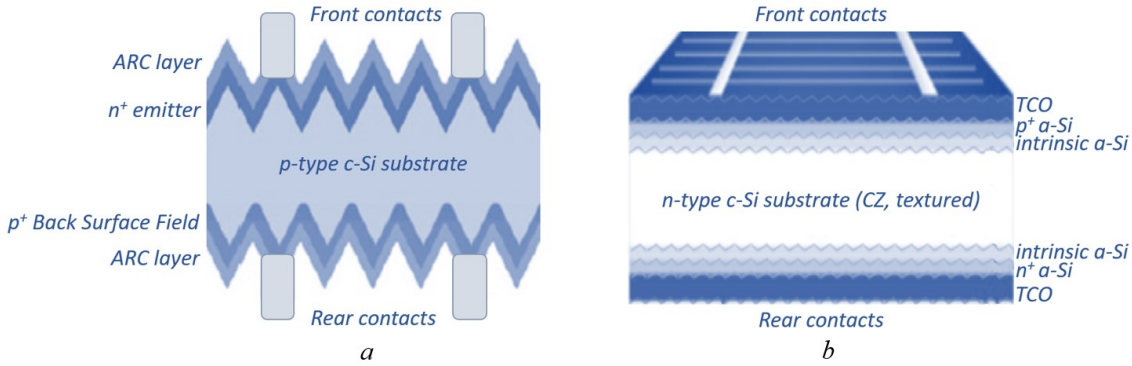

Fig. 1.6 – Schematic representation (layers' sequence) of: a. bifacial solar cell structure; b. silicon heterojunction (Si HJT) solar cell structure.

According to fig. 1.6 a, generally a metallization, formed by suitable open grids on both cell front and rear sides, makes it possible the absorption of the solar radiation from both such sides; moreover, the emitter at the cell front side consists of a n^+ diffused layer, while the so-called *Back Surface Feld* is made by a p^+ diffused layer; on both the front and rear sides of the cell, anti-reflection coating passivated layers with textured surfaces are manufactured, to facilitate the light trapping and adequately limit the reflection losses [37], [39].

Among the most promising technologies, there is the so-called *Silicon heterojunction (Si HJT) solar cells technology*, which is particularly suitable for the fabrication of bifacial PV devices, consequently to the symmetrical structure (shown in Fig. 1.6 b) of each solar cell [40], [41]. It is noteworthy that such a technology had allowed to achieve the previous world power conversion efficiency record (of 25.6% at the research stage, referred to a single solar cell, having an active area equals to 143.7 cm^2), as it had been announced by Panasonic Corporation in April 2014 [42], [43]. More recently, further developments

based on this technology have brought in a short time to the new efficiency record above 26%, with reference to the mentioned (see section 1.2) silicon heterojunction solar cells with interdigitated back contacts *(HJ-IBC tech.*) [18]. As it has been highlighted in [43], significant electrical performances have been achieved for silicon heterojunction solar cells, by adopting for the structure depicted in Fig. 1.6 b the material thicknesses listed here: a thin monocrystalline silicon wafer of the order of one hundred μm approximately; p-type, n-type and intrinsic amorphous silicon layers of about 10 nm. Generally, by manufacturing high quality a-Si layers over the crystalline silicon substrate, it is possible to obtain an adequate limitation of the recombination losses of the charge carriers into the cell, in addition to limit the solar cell electrical performance variations when its operating temperature changes (i.e. suitably reduced values of the PV cell temperature coefficient referring to power conversion efficiency[4]).

Since the eighties of the last century, the bifacial devices had been considered a novel concept technology able to improve the energy generation of PV plants [44] and, over the last years, they have had a significant fast development, as a consequence of their multiple benefits, compared to conventional mono-facial PV devices. Actually, among the main advantages, the bifacial PV devices make it possible a more efficient material exploitation. Indeed, each bifacial solar cell has both its front and rear surfaces light-sensitive and able to generate electricity by efficiently harvesting and exploiting the solar radiation. Consequently, the installation of these devices in a PV plant can involve a saving on the cell costs and more in general on the costs linked to area, in addition to a reduction of the Levelized Energy Cost [45], [46].

An important advantage arising from the use of bifacial PV technology consists in the increase of electricity generation per unit area, as a result of the adequate exploitation of additional solar radiation harvested by each bifacial solar cell rear surface. In fact, as it has been proved from several studies in the scientific literature (for instance, see [47], [48]), by using bifacial devices in a PV system, it is possible to significantly increase the electricity produced, compared to that obtainable by mono-facial devices, at the same installation conditions. In this regard, as remarked in [47], a bifacial gain[5] up to 50% could be achieved, although by considering an ideal configuration of standalone PV modules. However, it is very important to note that generally the extent of such a bifacial gain in real conditions strongly depends on several factors afflicting the electrical performance of a bifacial PV module (e.g. the module elevation, its orientation and tilt angle, the ground albedo, installation site location, in addition to other installation conditions peculiarity) [49].

Currently, the bifacial PV technology, even if it was already devised from the early stages of PV science in the sixties of the last century [50],[51], is at its birth. Many relevant major points remain. For

[4] Such parameter is generally used to express the power conversion efficiency variation rate of a solar cell when its temperature increases of 1 °C.

[5] (i.e. a parameter, suitably defined, indicating the gain in terms of electricity yields, obtained by comparing the energy supplied by a bifacial module and a mono-facial one, in the same installation conditions).

example, one major problem is the lack of a standard methodology for the electrical characterization of such devices at the cell and at the module level. Another missing point is an accurate and in-depth analysis and understanding of their performance in real operating conditions, in order to individuate optimal installation conditions, allowing to maximize the electrical performance of these devices. Such important topics are determining a growing interest in the scientific community and several studies have recently treated them. Some of these studies (such as [52], [53]) have focused on the characterization methods of bifacial PV devices, while other studies (for instance, see [38], [49], [54]) have treated the modeling and performance forecast of bifacial modules, by varying the parameters significantly affecting their performances. In Chapter 5, the most relevant findings of some of these studies will be thoroughly described and examined.

Actually, the prediction of the bifacial PV module electrical performance for the purposes of their electrical characterization and the optimal installation condition determination has a crucial importance. It is for this reason that, with a view to enabling progress in this field, in such thesis work a new analytical model has been developed for predicting the electrical characteristics of bifacial modules and numerous experiments have been carried out for the validation of the mentioned model. The main results of such validation will be described and discussed in detail in Chapter 6.

1.5 Project purpose

With a view to actively contributing to the advancement of knowledge on the renewable energy sources' exploitation, in particular of solar energy, for the effective and efficient electricity generation, the main purpose of the doctoral research project has been the performance optimization of thin film Silicon and bifacial PV devices, through the outdoor variables affecting such performance.

A first phase of the study has been focused on tandem amorphous/microcrystalline Si PV devices, with the main objective of highlighting particular instability phenomena characterizing their electrical performance. The causes of such instability have been thoroughly investigated, to allow a more in-depth knowledge of the electrical behavior of such devices. Actually, the aforementioned tandem PV devices, in addition to have some undeniable advantages compared to other types of photovoltaic devices (as pointed out earlier in section 1.3), are affected by significant performance instability phenomena. Such phenomena can involve reliability issues, although in some cases they involve improvements of the solar cell overall power conversion efficiency. They are consequent to the significant light induced degradation, due to the Staebler-Wronski effect, typically characterizing the a-Si: H solar cells, and to the specific working conditions to which the aforementioned PV devices are subjected (in terms of illumination, temperature and electrical stress conditions), which instead can lead to a recovery / improvement of their overall electrical performance. From the need to carefully detect and study such phenomena, the first part of this Ph.D. thesis project is born.

Studying the different types of photovoltaic devices available today, it is noteworthy that currently a growing interest, both of the scientific community and the PV industry, is oriented to the high efficiency Si bifacial PV devices, consequently to the multiple advantages which they have compared to the traditional mono-facial ones (as it has been observed in more detail in the previous section 1.4).

Such a remarkable interest together with the recent and fast technological advances made in the field of high efficiency bifacial Si PV devices have given rise to the need for a subsequent study targeted on the performance optimization and electrical behavior of these latter devices, on which the second part of this Ph.D. thesis project has been focused.

Considering the importance of carefully studying and accurately forecasting the performance of these devices, with a view to allow the identification of optimal installation conditions (i.e. conditions maximizing the bifacial device performance), the main purpose of the mentioned second and last part of the project has been the development and experimental validation of a novel analytical model, for predicting the electrical performance of such devices for any geographical location. Contextually, further main goal of the second part of the project has been a detailed analysis of the bifacial module electrical behavior, by varying the main parameters affecting their performance (i.e. PV module elevation from the soil, module tilt angle, ground albedo), for contributing to the advancement of knowledge in this context. Finally, the novel model proposed has been used for predicting the electrical performance of bifacial PV systems with and without solar tracker, with reference to different geographical locations. The latter analysis has been performed in order to study the convenience of adopting a solar tracking system for optimizing a bifacial PV system performance. Moreover, by adapting the mentioned model to predict the electricity production of a traditional mono-facial PV system with and without solar tracker, we have also investigated on the convenience of installing a fixed (i.e. without any tracker) bifacial PV system with the same geometry, rather than using a solar tracking system to optimize the performance of a mono-facial PV system.

CHAPTER 2 PERFORMANCE INSTABILITY OF AMORPHOUS SILICON BASED PV CELLS: A BRIEF SUMMARY OF THE STATE OF ART

In this chapter, the main findings of previous studies in the scientific literature regarding performance instability phenomena of hydrogenated amorphous silicon (a-Si:H) solar cells will be summarized, in order to provide an overview on this topic and to facilitate the reading of the following chapter 3 (in which the results of new experiments, aimed to further investigate the above mentioned phenomena, will be illustrated and discussed). Firstly, a focus will be made on the well-known Staebler-Wronski Effect and on the main thermal effects affecting the performance of the aforementioned solar cells (see sections 2.1 and 2.2). Afterwards, a synthesis of the already known performance improvement basic dynamics, observed for such cells under reverse bias DC stresses and illumination, will be provided (see section 2.3). Finally, some instability effects observed on the mentioned devices, induced by solar spectrum variations, will be illustrated (see section 2.4).

2.1 Staebler-Wronski Effect and Light induced degradation

As it has been mentioned in the introductory Chapter 1 (see section 1.3), the a-Si:H based solar cells are subjected to a remarkable degradation phenomenon of their performance when they are exposed to the light. For the first time, such a phenomenon was observed in 1977 by Staebler and Wronski on amorphous Silicon films [23], so that nowadays we refer to this phenomenon as the "Staebler-Wronski Effect". Basically, this effect involves a light induced degradation of hydrogenated amorphous silicon solar cells, by determining considerable cell power conversion efficiency decreases under illumination, typically within the first few hundred hours [22]. In Fig. 2.1, an example of such a degradation is shown, with reference to two amorphous silicon-based devices (i.e. a single-junction solar cell and a multi-junction module), subjected for some thousand hours to the illumination (i.e. a so-called "*light soaking"*) supplied by a solar simulator. As it can be deduced from this figure, after a time interval of about one thousand hours, an output power density significant reduction (of approximately 30%, compared to the initial value) is observable for an a-Si single-junction PV cell.

Although significant efforts were made by several authors to extensively study the undesired Staebler-Wronsky degradation effect, a well-defined mechanism to definitely explain the underlying mechanism of the light-induced degradation occurring in a-Si:H based PV devices is still missing.

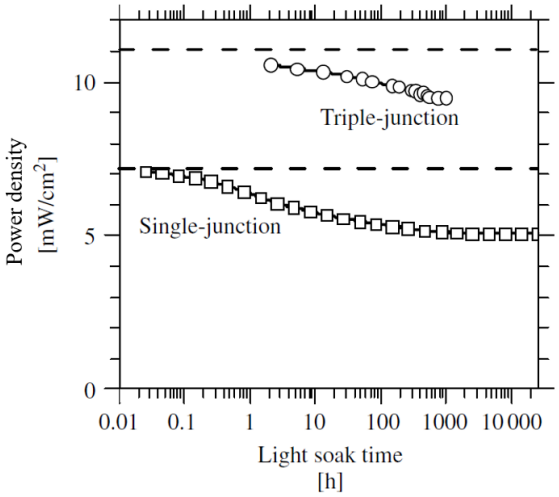

Fig. 2.1 – Light induced degradation for two amorphous silicon-based devices (i.e. a single-junction solar cell and a triple-junction module), subjected to light soaking under a solar simulator illumination at 1000 W/m². Source: [22],[55].

The most widely accepted theory is that the defect states, existing in the amorphous network, playing an important role in determining the material electronic performance, act as trap states and recombination centers, namely where charge carriers remain trapped, so that ultimately a performance degradation is determined [25].

Moreover, as it was underlined in the scientific literature [24], [25], [56], it is believed that the hydrogen atoms in the hydrogenated amorphous silicon structure (which allow, as a benefit, to partially passivate the so-called *Dangling Bonds*, typically existing in the amorphous silicon network [57]) have a relevant role in metastable defect generation: basically, the light to which an a-Si:H based PV cell is exposed supplies a sufficient energy for breaking the nicknamed "dilute H phase", so that *Dangling Bond defects* are generated [58],[59][6]. Essentially, the generation of a Dangling Bond defect can be imagined by simply considering that a hydrogen atom is removed from its dilute phase site, leaving behind an unoccupied single electron state, namely a dangling bond.

The experimental data so far collected clearly indicate that the exposure of hydrogenated amorphous silicon to light increases the density of neutral silicon dangling bonds. This involves an excess of metastable defects, which determines a significant reduction of the lifetime of free carriers. Furthermore, it was observed that the generation of metastable dangling bonds is the result of recombination events between carriers generated by light absorption [60].

In the example of Fig. 2.2, the increase of dangling bond defect density (compared to the time zero defect density), occurring under illumination for two different light intensity cases, is clearly shown. As

[6] For the hydrogen in the a-Si:H material structure, two main "phases" (i.e. configurations where the hydrogen is bonded to silicon atoms) have been identified, namely: the so-called "dilute phase" and "clustered phase". In the first one, a hydrogen atom is approximately 1 nm far from any other hydrogen atom; in the second one (i.e. the clustered phase), two or more hydrogen atoms coexist in close proximity. It is believed that while the dilute phase sites contribute to dangling bond creation, presumably the clustered phase sites do not contribute to their creation.

widely shared in the literature, such an increase would be the main cause of the Staebler-Wronski Effect, by ultimately leading to the aforementioned power conversion efficiency worsening for a solar cell exposed to the light. For the mentioned defect density, a saturation steady-state value (of approximately 10^{17} cm^{-3} in the case of high intensity illumination, according to the data of Fig. 2.2) seems that can be achieved [24],[61]. On the other hand, as it was remarked for example in [62], by subjecting a-Si:H based PV devices to light soaking at stable illumination conditions, after one thousand hours, a stabilized power conversion efficiency seems to be achievable for these devices.

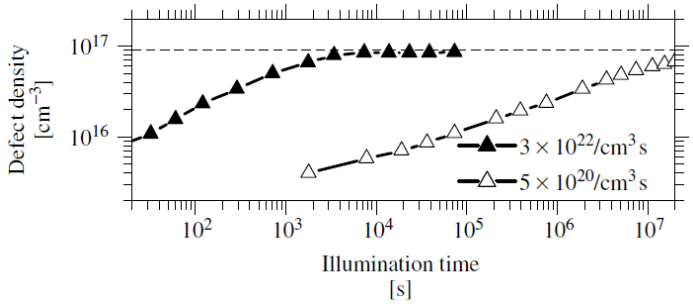

Fig. 2.2 - Dangling bond defect density trend as a function of the illumination time, as measured in [61]*, by subjecting an a-Si:H film to extended illumination. The data refer to two different cases of light intensity: a low light intensity case and a higher light intensity case; the photocarrier generation rate referred to each intensity are specified in the legend. Source:* [22].

Even though the Staebler-Wronski Effect is a not negligible drawback for the a-Si:H based technology, it is noteworthy that a fundamental characteristic of the light-soaking effect on a-Si:H PV devices and films is its metastability. In fact, it is possible to remove such an effect through a thermal annealing of a specimen previously subjected to light - soaking. Such an annealing can lead to a nearly total recovery of the specimen initial performance (i.e. the ones existing before the light – soaking effect). This aspect will be further discussed in the next paragraph.

2.2 Thermal effects on a-Si based solar cells: main previous findings

As it was proved in several studies in the literature (for instance, see [63],[64]), a thermal annealing of a-Si based PV devices can result in significant benefits on the performance of such devices.
A thermal annealing at temperature above 150°C, for a short time interval (usually few minutes), of a-Si based solar cells, previously subjected to light-soaking, leads to an almost complete restore of the cell initial performance (namely the one existing before the light induced degradation) [22],[23].

Since any thermodynamic process is defined by an activation energy, a certain amount of energy will be necessary to generate defects and a certain amount of energy will allow to remove them. A light-soaking can provide the needed energy amount to generate defects within the material, instead an adequate thermal annealing is able to reverse such process, by removing defects. Essentially,

metastability requires an energy barrier between alternative states (for instance, A and B) and a generation of defects through external excitation. The recovery process obtained by means of thermal excitation is well represented by Fig. 2.3 [65].

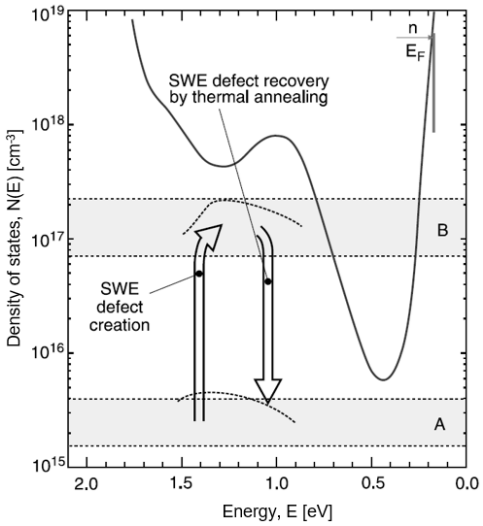

Fig. 2.3 – Defect density variation in a-Si:H, due to defect generation determined by light-soaking and defect recovery induced by thermal annealing. Dashed curves indicate defect density measured for intrinsic a-Si:H films before and after light induced degradation. Continuous curve indicates defect density for n doped a-Si:H film. A: range for high quality intrinsic a-Si:H; B: range of maximum defect density generated by extended ill. (saturated level). Fermi level (E_F) for n doped a-Si:H film is shown too. Source: [65].

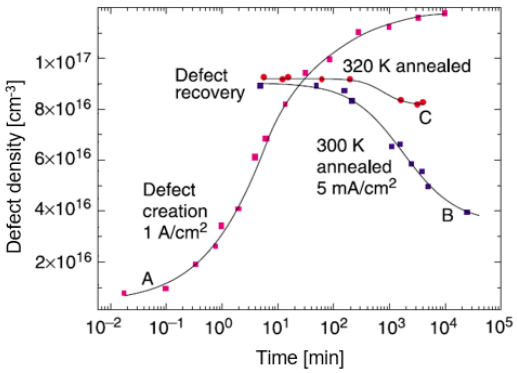

Fig. 2.4 – Defect recovery induced by thermal annealing at moderate temperatures on a pin a-Si:H diode. Time evolution of defect density: curve A: defects are generated under forward current of 1 A/cm^2; curve B: defect recovery induced by an annealing at 300 K, with 5 mA/cm^2 forward current, after inducing 9×10^{16} cm^{-3} defects with 1 A/cm^2 forward current for 100 min; curve C: defect recovery obtained exclusively by annealing at 320 K, after inducing 9×10^{16} cm^{-3} defects with 1 A/cm^2 forward current for 100 min. Source: [65].

It should be noted that also a thermal annealing at moderate temperatures can lead to observe not negligible benefits on the performance of a-Si:H PV devices [64],[66].

On the other hand, also such a type of thermal annealing determines a defect recovery (i.e. a defect density reduction, after a defect density growth) in a-Si:H devices, as it is clearly shown in Fig. 2.4.

Based on what has been seen so far, we can say that the light induced degradation and the thermal annealing represent two processes under way continually, by producing a kind of equilibrium between generation and annihilation of the defects within the material. Furthermore, it can be assumed that performance reversible variation phenomena observable on a-Si:H PV devices are based on such processes, as it will be highlighted in the following chapter 3.

As it was widely studied and remarked in the literature about the thermal behavior of hydrogenated amorphous silicon-based PV cells, actually this behavior is more complex than that of the crystalline silicon solar cells, which is a typically linear one. In fact, for a-Si PV devices a not perfect linear behavior was observed. For instance, in [33], for dual-junction amorphous Silicon thin film solar cells, significant improvements of power conversion efficiency were observed when their temperature increased. In particular, a remarkable positive temperature coefficient equals to 0.14%, referred to the PV devices efficiency, was measured within 25–45 °C temperature range, even if a negative value of such coefficient resulted for different temperature ranges (see graph in Fig. 2.5).

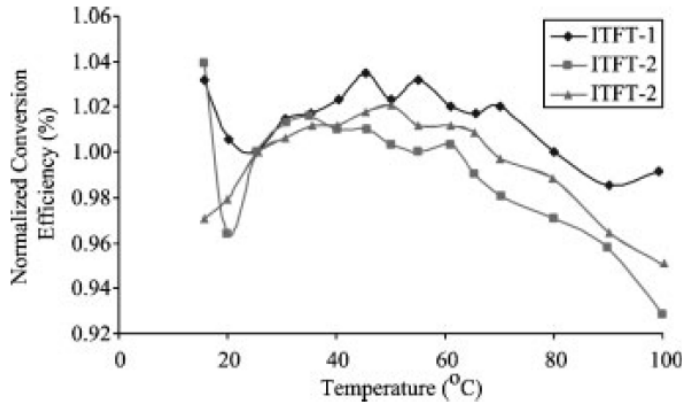

Fig. 2.5 – Normalized power conversion efficiency trends of dual-junction a-Si solar cells, detected as a function of such device temperature. Source: [33].

As it was noted in [34], as a matter of fact, the specific thermal behavior of a-Si based PV devices is basically characterized by two main phenomena, in conflict with each other. Such phenomena are associated to the cell temperature rise, by affecting the cell electrical performance: the first phenomenon consists in the inborn tendency to decrease of a solar cell efficiency by increasing its temperature (such a behavior is that usually observed for most solar PV devices; it leads to a negative value of the temperature coefficient referred to the efficiency); the second one consists in the benefit which a cell thermal annealing is able to produce on the cell performance, as a regenerative effect. This latter phenomenon can allow to detect in specific experimental conditions a positive value of the temperature coefficient related to solar device efficiency (as in the case of the study [33]).

Finally, it is noteworthy that typically, for negative values of the temperature coefficient of the cell efficiency, the a-Si based PV devices exhibit, by rising temperatures, a considerably lower output power decrease, in comparison to other thin film PV technology. This is what occurs probably because of the thermal annealing regenerative effect [34]. Such a peculiarity has led to consider the a-Si based PV devices particularly suitable for the installation in hot climate regions, as it will proved and further discussed herein in chapter 4.

2.3 Performance improvement dynamics in a-Si:H and tandem amorphous / microcrystalline Si solar cells

2.3.1 LID reversibility and performance improvements via reverse bias DC stresses under illumination

As it has been introduced in Section 1.3, numerous studies [21],[26],[27],[29-31] proved that, both for single junction a-Si:H solar cells and tandem a-Si / μc-Si ones, not only a reversibility of the Light induced degradation exists, but also remarkable performance improvements are obtainable, via suitable DC reverse bias stress conditions applied to such solar cells, under illumination. In this regard, the benefits of such reverse bias stresses were initially studied on single-junction solar cells (subjected to experiments indoor, under the illumination provided by a solar simulator) and remarkable efficiency increases were observed, as for example shown in the graphs of Fig. 2.6. As it can be clearly seen, the amount of the efficiency increase depends on both the reverse bias voltage level applied to the solar cell and the light intensity. Actually, such a performance improvement effect (which was observed for the main electrical parameters of a solar cell) is assisted by the light, with growing improvements detected by increasing the intensity of the light which illuminates the solar cell (see Fig. 2.6 b) [27], [30],[31].

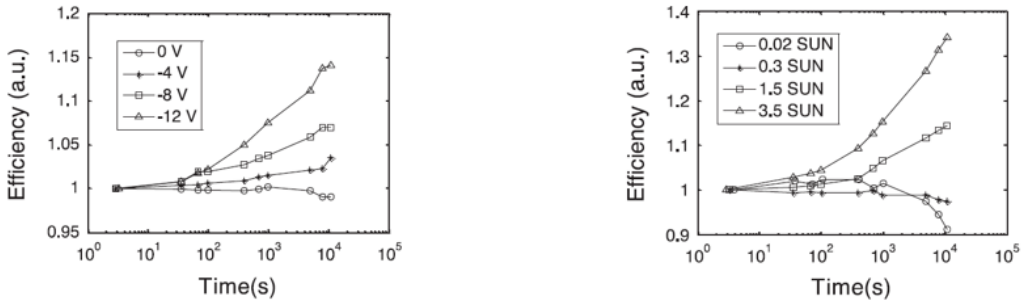

a *b*

Fig. 2.6 –Power conversion efficiency normalized trends observed on a-Si:H single junction solar cells, as a function of the stress time: a. by varying the reverse bias voltage applied, under constant illumination of 1.5 SUN; b. by varying the irradiance level, with a fixed reverse bias voltage of -4V. Source: [31].

In addition to the power conversion efficiency trends, those of the other main electrical parameters of a solar cell (namely, short circuit current density, Jsc, open circuit voltage, Voc, series resistance, Roc, and fill factor, FF), in response to reverse bias stresses under illumination, were carefully analyzed too. For instance, in Fig. 2.7 the trends of such parameters, corresponding to the efficiency trends of Fig. 2.6 a., are reported. As it appears evident from Fig. 2.7, the cell parameters which exhibit the most significant improvements are the Roc (which decreases) and consequently the FF (which increases), and the Voc. The highest improvements were observed for the highest reverse bias applied to the studied solar cells. It is noteworthy that, as remarked in [31], the layer dominating the Roc is the p-type a-Si:H film, which hence is the one responsible for the Roc variations.

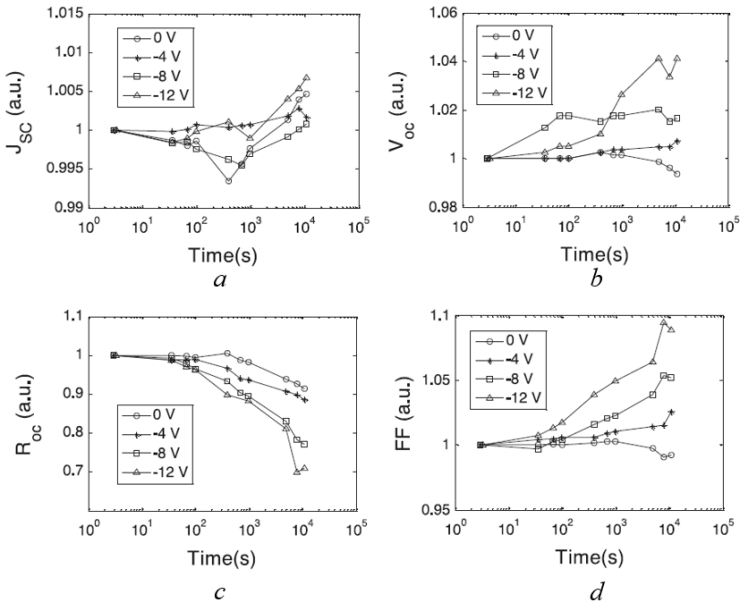

Fig. 2.7 – Normalized trends, observed on a-Si:H single junction solar cells, of a. short circ. current density (Jsc), b. open circ. voltage (Voc), c. series resistance (Roc), and d. fill factor (FF), as a function of the stress time, for different reverse bias voltage values (indicated in the legend) under constant illumination of 1.5 SUN. Such trends correspond to those of the power conv. efficiency in Fig. 2.6 a. Source: [31].

Furthermore, in the study [31], it was noted that the aforementioned performance improvement effect is linked to a reversible motion of ions (probably related to H species) at the TCO / p+ a-Si:H interface, driven by the external electric field (associated to the reverse bias applied to the solar cell) and by the illumination, as schematically represented in Fig. 2.8.

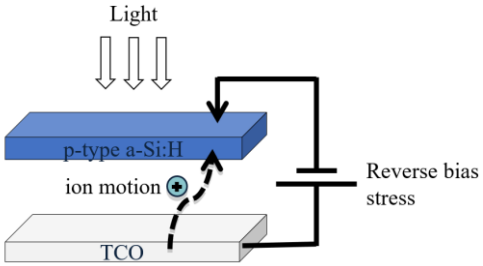

Fig. 2.8 – Schematic representation of the ion migration (probably of H species) at the TCO / p+ a-Si:H interface of an a-Si:H PV cell, under illumination and reverse bias stress, as proposed in [31] to explain the performance improvement observed for such type of PV cells.

Considering that a materials interface similar to the above mentioned one is found in tandem a-Si /µc-Si solar cells, consequently, a similar experimental study was extended to the latter cells. This led to conclude that also for such solar cells evident performance improvements are verifiable under adequate reverse bias stress and illumination conditions (as for instance, it is clearly shown in Fig. 2.9).

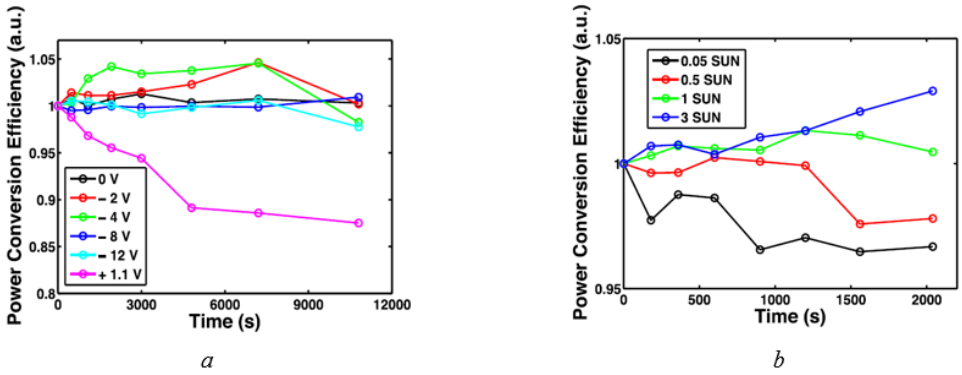

Fig. 2.9 - Power conversion efficiency normalized trends observed on tandem a-Si /µc-Si solar cells, as a function of the stress time: a. by varying the reverse bias voltage applied, under constant illumination of 1 SUN; b. by varying the irradiance level, with a fixed reverse bias voltage of -4V. Source: [21].

Also for the case of a-Si /µc-Si solar cells, the trends of all their main electrical parameters were studied, to extensively analyze the effect on the performance of such cells induced by the applied reverse bias stresses under illumination. By way of example, in Fig. 2.10, the normalized tends of Jsc, Voc, Roc, corresponding to the efficiency trends of Fig. 2.9 a., are reported, as a function of the stress time, for different levels of reverse bias DC voltage stresses applied to the solar cells in question, under illumination. From the Fig. 2.10, we clearly see that, by applying adequate reverse bias stress voltage levels (best behavior observed at -4V), an evident improvement of the cell electrical parameters was observed, with a consequent shift toward higher power conversion efficiency values (as illustrated in Fig. 2.9 a.). Instead, under maximum power point (see the case of positive voltage stress applied), or in short circuit condition (see the case of stress at voltage equal to 0), a clear worsening of the solar cell electrical parameters was detected, as a result of the Staebler–Wronski degradation effect under cell

illumination. Therefore, it was concluded that, similarly to the case of single junction a-Si:H PV cells, also for the tandem a-Si /µc-Si solar cells, by applying adequate reverse bias stress conditions under illumination, not only it was observable a slowdown of the wear out rate under light soaking, but also clear improvements of the solar cell characteristics were verifiable [21].

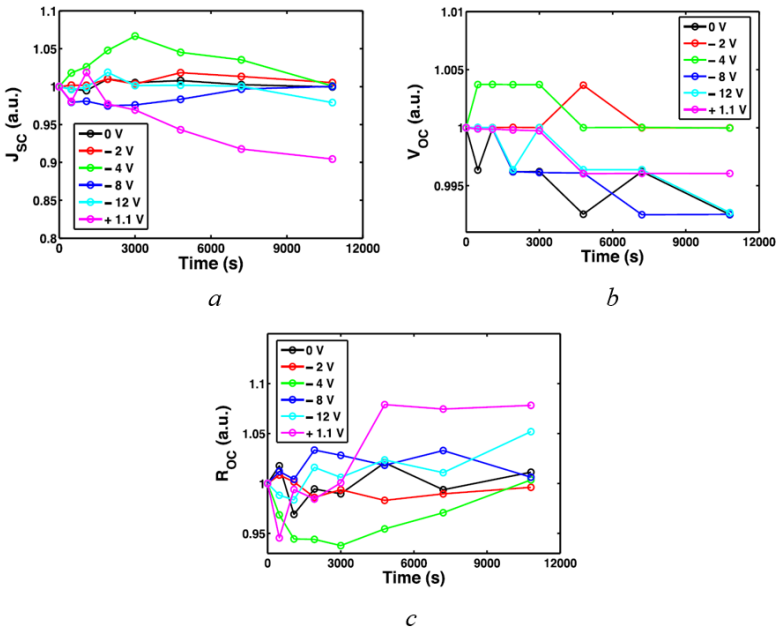

Fig. 2.10 - Normalized trends, observed on tandem a-Si /µc-Si solar cells, of a. short circ. current density (Jsc), b. open circ. voltage (Voc),and c. series resistance (Roc), as a function of the stress time, for different reverse bias voltage values (indicated in the legend) under constant illumination of 1 SUN. Such trends correspond to those of the power conv. efficiency in Fig. 2.9 a. Source: [21].

As it was underlined in [21], [27], it is noteworthy that in the case of tandem a-Si /µc-Si solar cells much lower levels of stress voltage (with an electric field of a factor 25 times lower) are needed to achieve performance increases similar to that observed for single-junction a-Si:H PV cells. Such a significant difference was explained by assuming that the high hydrogen concentration in the µc-Si layer (considerably greater than that in the TCO) probably facilitates a diffusion of hydrogen ions toward the a-Si:H cell, making the performance improvement effect evident with lower values of electric field applied.

Finally, it should be noted that in the work [27] the reversibility of ageing effects of a-Si:H cells was analyzed too. In particular, for such cells the dependence of the electric parameters' trends from the applied stress voltage sign was studied, as for example illustrated in Fig. 2.11.

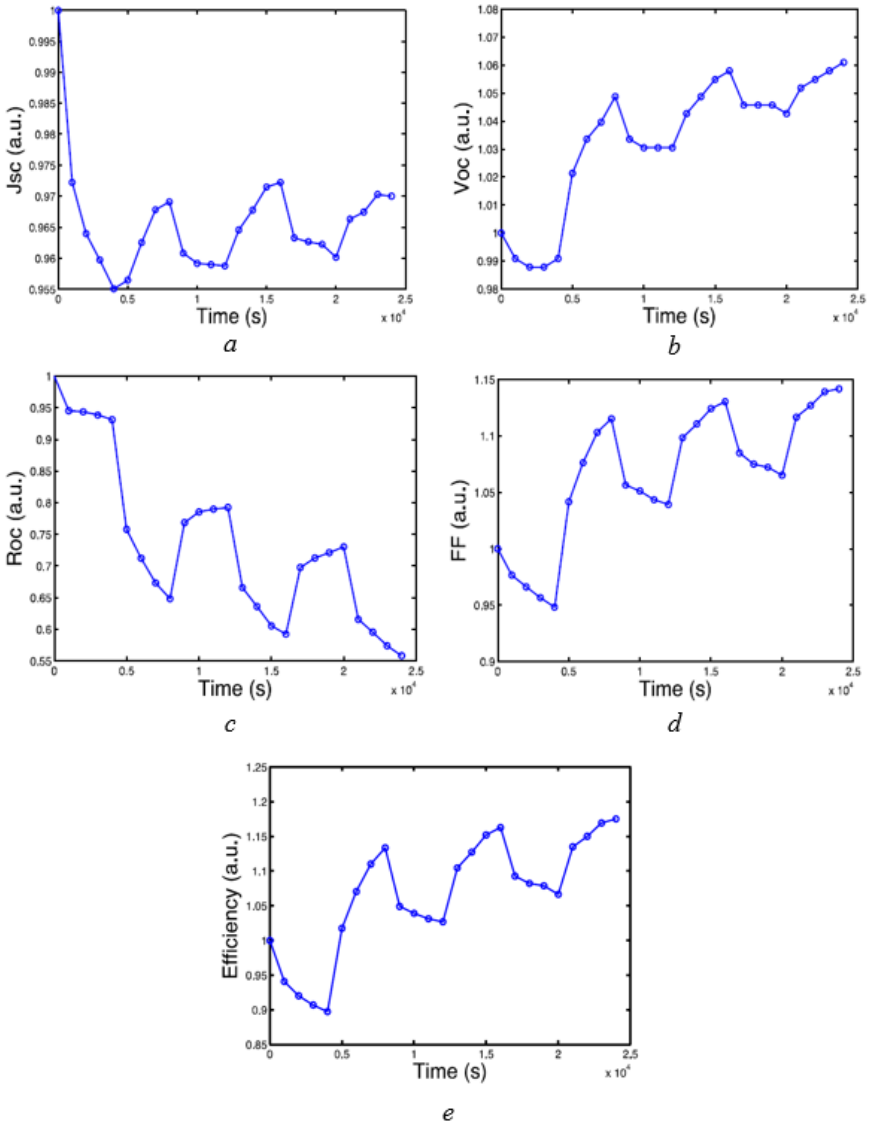

Fig. 2.11 - Normalized trends of a. Jsc, b. Voc, c. Roc, d. FF, and e. power conv. efficiency, as a function of the stress time, for an a-Si:H PV cell subjected to reverse and forward bias stresses (of -12 V, +0.6 V, respectively), alternately applied (for a duration of $4 \cdot 10^3$ *s each), under illumination of 3 SUN. Source:* [27].

From the latter figure, we can clearly see that reversible monotonic trends were observed for all the solar cell electrical parameters, in response to reverse and forward bias stresses alternately applied, with evident significant improvements of such parameters caused by the reverse bias stress sequences (subsequently to their worsening observed during the forward bias stresses under illumination).

2.3.2 Light wavelength effects

In [26], the dependence from the illumination of the performance improvements observed on a-Si based solar cells was further studied. Initially, an analysis on single junction a-Si:H solar cells was carried out, with the main goal to determine the wavelengths range in which the photons are effective

for leading to an improvement of the solar cell efficiency and the lifetime. In particular, the solar cells subjected to reverse bias stress were illuminated with monochromatic light at different wavelengths and the evolution of the cells External Quantum Efficiency (EQE) was monitored. Fig. 2.12 a. summarizes the main results of this experiment. The curves in such figure correspond to different values (ranging from 400 nm to 900 nm) of light wavelength used for illuminating an a-Si:H cell during the stress and they are normalized to the same flux of pump photons. A cell External Quantum Efficiency improvement exists (as it is evident from Fig. 2.12 a.) exclusively in the [700, 800] nm wavelengths range, while outside such an interval no significant EQE improvement or variation was seen. This fact led the authors of the work [26] to conclude that the lifetime improvement mechanism is correlated to a process triggered by photons within the abovementioned wavelengths range (namely, with energy equal to 1.6-1.7 eV, close to the a-Si:H band gap).

As the authors reported in the work [21], further studies concerning the light wavelength effects were performed on tandem a-Si/µc-Si PV cells, after the performance improvements observed on such cells under DC reverse bias stress. The goal of the latter studies was of discerning which of the PV cells in series constituting the tandem structure (namely, the a-Si and the µc-Si ones) determined the improvements detected. The main finding of such studies is represented in Fig. 2.12 b. which shows the ratio of the EQE spectrum obtained after a reverse bias stress (at -4V for 5 minutes) by illuminating an a-Si/µc-Si PV cell with a 700 nm light to the initial EQE spectrum of such cell. From the latter figure, we see clearly a growth, after the stress performed, of External Quantum Efficiency in the blue portion of the spectrum, which is the one converted into electricity by the top a-Si cell. Instead, the EQE spectrum red portion (namely the portion of the solar spectrum managed by the µc-Si PV cell) remains practically unchanged. This element led to conclude that the reverse bias stress entails a performance improvement of the a-Si cell exclusively and not of the µc-Si one; such an improvement is responsible of the comprehensive performance improvement observed for the tandem PV cell.

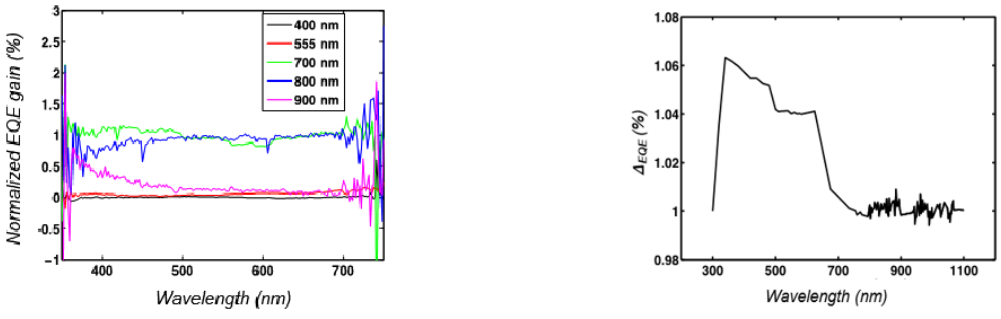

a *b*

Fig. 2.12 – Light wavelength effects observed on a-Si:H based solar cells: a. norm. EQE gain for a single junction a-Si:H solar cell, in reverse bias stress, under monochr. lights at the wavelengths specified in the legend (source: [26]*); b. ratio of the EQE spectrum after a rev. bias stress (at -4*

V for 5 min) on a-Si/μc-Si PV cell illuminated with a 700 nm light to the cell initial EQE spectrum (source: [21]*).*

2.3.3 Temperature role under reverse bias DC stresses

Another noteworthy aspect which was investigated in the literature consists in the role played by cell temperature on the amount of the performance improvements achievable for a-Si based PV cells in reverse bias stress conditions. As underlined in [27], such a role was experimentally studied for a solar cell subjected to a -12 V voltage stress under the illumination of 1.5 SUN, by varying its temperature. The main result of this study is depicted in Fig. 2.13: the highest increase of cell electrical performance was observed with cell temperature values of about 40-50 °C, while lower performance improvements were detected for temperatures lower or higher than the abovementioned values. Such fact confirms that the cells temperature constitutes a further relevant parameter for the a-Si based PV cells performance improvement dynamics.

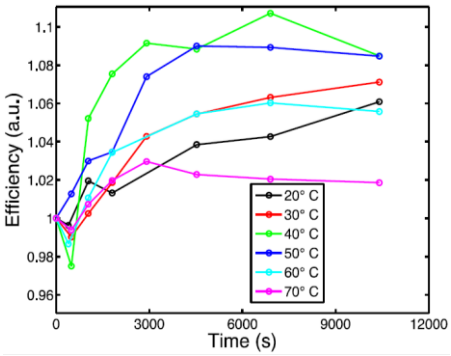

Fig. 2.13 – Normalized power conv. efficiency trends as a function of the stress time, observed for an a-Si:H PV cell illuminated at 1.5 SUN under reverse bias stress (with a voltage level of -12 V), by varying its temperature. Source: [27].

2.4 Effects of solar spectrum variations on a-Si based PV devices

Some studies in the literature (for instance, see [67–70]) focused on the effects triggered by solar spectrum variations on the performance of a-Si based solar devices, by observing that such devices have more sensitivity to spectral changes, compared to other photovoltaic technologies. Actually, in some cases not negligible performance instability phenomena, due to the mentioned changes, were detected on the devices in question. Therefore, the authors of these studies concluded that it can be important paying attention to solar spectrum variations, in order to carefully analyze the performance of the mentioned devices.

For instance, in [68] the authors observed that these modules are particularly sensitive to seasonal variations in the solar spectrum. In such work, the authors had carried out solar spectrum measurements in UK (at a latitude of 52° N) for several months during different years. From these measurements, the

parameter named “Useful fraction” (defined as the ratio of the observed spectral irradiation in the useful spectral range of the considered solar device to the observed global irradiation) was determined for three different thin-film PV technologies (i.e. CdTe, CIGS, a-Si). This allowed the authors to show more significant variations of such a parameter on a monthly scale for the a-Si technology (such variations ranged from +6% to -9%), although useful fraction improvements were observed throughout the summer months for all the technologies [68].

In [67], it was experimentally proved that detected solar spectrum variations had an influence on two fundamental electrical parameters of a-Si solar modules, i.e. their short circuit current and fill factor. For the latter parameter the significant variations in Fig. 2.14 were observed. In such figure, two main cases were considered to remark the effects of solar spectrum changes: the case of high diffuse fraction (> 0.8) (which typically occurs for solar spectrum with higher blue component, as for instance observable in cloudy days with low global solar irradiance) and the one of low diffuse fraction (< 0.2). The latter case is associated to two main conditions: the condition of spectra similar to the standard spectrum for high irradiation levels, near to midday and the one of solar spectra with higher red component, typically observable in the early morning and in the late afternoon. By observing the graph in Fig. 2.14, it is evident that the solar spectra with higher blue component (see high diffuse fraction case) led to a performance improvement (FF increase), while a red shifted solar spectrum (see low diffuse fraction case) determines a decrease of FF.

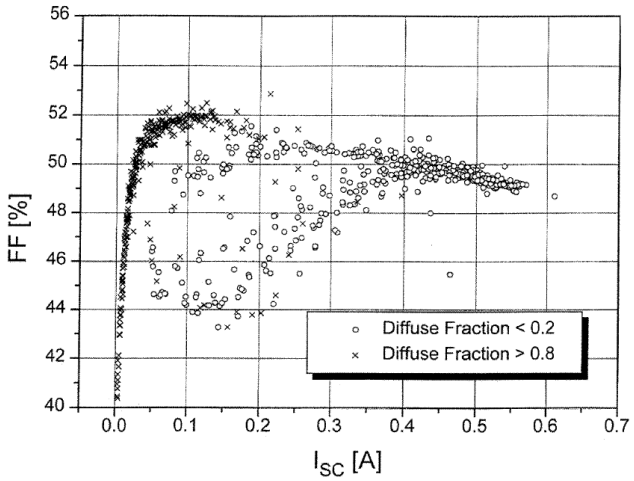

Fig. 2.14 – Trend of the fill factor (FF), as a function of the short circuit current (Isc) for an a-Si PV module, for two different diffuse fractions. Source: [67].

On the other hand, it is well-known from the literature that the External Quantum Efficiency curve of a-Si based solar cells exhibits a better response of these cells to the blue light (as clearly shown in Fig. 2.15). Therefore, the performance improvements, observed in terms of FF in Fig. 2.14 for the case

of solar spectra with higher blue component, are explainable by considering the mentioned better response of the solar cells in question to the blue light.

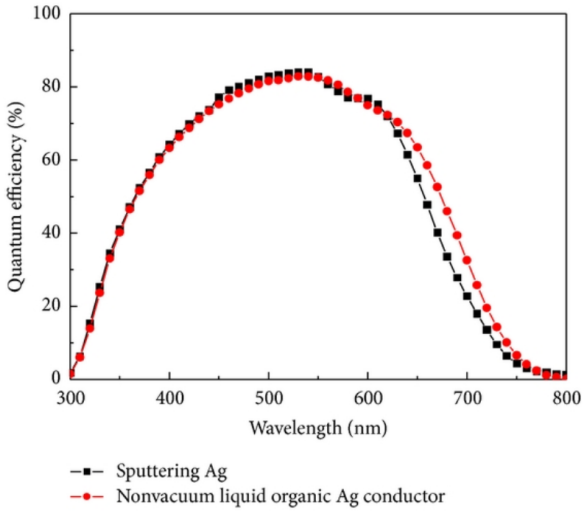

Fig. 2.15 – EQE spectra for a-Si:H solar cells (with different back reflectors process). Source: [71].

CHAPTER 3 NEW EXPERIMENTS ON TANDEM AMORPHOUS / MICROCRYSTALLINE SI PV DEVICES: DESCRIPTION AND MAIN FINDINGS

This chapter is focused on the results of new experimental activities, carried out in this work on tandem amorphous / microcrystalline Si photovoltaic (a-Si:H / μc-Si PV) mini - modules, with the main goal of further investigating the performance instability phenomena found in the literature on a-Si based solar cells (as summarized in the previous chapter 2). In section 3.1, the aims of such activities will be explained more in detail. After a description of the experimental setups used for the mentioned activities and the experimental methods applied (see section 3.2), the main findings of the experiments performed will be highlighted and discussed in depth (see section 3.3). In the final part of the chapter, the causes of instability phenomena systematically observed on the aforementioned PV mini – modules in Maximum Power Point (MPP) outdoor operation, will be thoroughly analyzed. In this regard

, we will show and discuss the effects on the mini – modules performance induced by solar cell temperature and solar spectrum variations.

3.1 Aims of the experimental activities

The main goal of the research activities performed on tandem a-Si/μc-Si PV mini - modules consisted in a further investigation on some performance instability effects, previously noticed in the scientific literature prevalently on individual solar cells.

In particular, the first aim was of verifying, by means of suitable tests, that the application of adequate reverse bias DC stresses to the mentioned mini - modules under illumination determines benefits on their electrical performance, similar to those observed in some previous studies in the literature on single solar cells tested indoor exclusively (see section 2.3.1). The practical convenience of such performance improvement technique was contextually investigated.

A further relevant aim was of highlighting electrical performance significant improvements of the abovementioned PV mini - modules, verifiable as a systematic effect in the afternoon hours, by exposing to sunlight stabilized samples of such devices working in forward bias condition.

At last but not least, the third aim was of studying in depth the possible causes of the latter improvements, in order to individuate the main factor which predominantly affects the observed electrical performance improvement.

3.2 Devices and experimental methods

3.2.1 Devices and experimental setups description

Different groups of specimens of tandem amorphous/microcrystalline silicon PV mini - modules were subjected to several experimental tests (both indoor, under illumination provided by a solar simulator, and outdoor under the sunlight). Three solar cells electrically in series make up each of the mentioned specimens. Essentially, each of these cells have the structure schematically shown in Fig. 1.5 (chapter 1). This structure consists of a stack of a p-i-n a-Si:H cell deposited on SnO_2:F transparent conductive oxide (TCO) layer, which collects the blue portion of the solar spectrum, on which it is deposited a p-i-n microcrystalline Si cell devoted to the collection of the red part of the solar spectrum. The cell is then covered with an Al doped ZnO TCO and an Ag film metallization. The thicknesses of the intrinsic layers in the amorphous and in the microcrystalline Si cells are approximately 200 nm and 1000 nm, respectively. Finally, the a-Si:H and µc-Si n and p type doped layers are few tens of nanometers thick.

The main characteristics of one of the tested specimens are summarized in tab. 3.1.

Dimensions (active area) [cm x cm]	3.2 x 2.1
Short circ. current density (J_{sc}) [A/cm^2]	9.88 x 10^{-3}
Short circ. current (I_{sc}) [A]	22.2 x 10^{-3}
Open circ. voltage (V_{oc}) [V]	4.06
Maximum Power Point curr. (I_{MPP}) [A]	22.1 x 10^{-3}
Maximum Power Point voltage (V_{MPP}) [V]	3.14
Maximum Power (P_{max}) [W]	69.4 x 10^{-3}
Maximum Power density (p_x) [W/cm^2]	10.9 x 10^{-3}
Power conversion efficiency [%]	10.9
Fill factor (FF) [%]	77
Series resistance (R_{oc}) [Ω]	23.49

Tab. 3.1 – Characteristics of one of the a-Si / µc-Si PV mini - modules tested. Note: electrical characteristics, referred to a stabilized specimen[7], measured at the solar simulator, at: 1 SUN (AM 1.5G), room temperature (specimen located orthogonally to the light beam supplied by the solar sim.).

For the tests performed outdoor, the experimental setup depicted in Fig. 3.1 was used. Essentially, this setup consists of:

[7] i.e. the initial electrical characteristics of a specimen subjected exclusively to extended light soaking for 1000 hours, before the tests on it.

- a set of specimens of the mini - modules above described;
- a c-Si reference solar cell (with the characteristics specified in Tab. 3.2), used for monitoring the solar irradiance over the minimodule plane during the tests performed;
- an adequate support (tilted of about 21° and oriented toward south), on which the specimens were located with the c-Si reference solar cell;
- a thermocouple, in contact with the glass covering one of the mini - modules (taken as reference for monitoring the cell temperature during the tests), linked to a multimeter (Fluke, model: 87 V), used to measure the glass surface temperature during some tests outdoor;
- a Keithley 4200-SCS instrument (suitably connected to the PV devices under test, as illustrated in the schematic of Fig. 3.1 a), used for forcing adequate stress conditions (according to the tests methodology which will be described in section 3.2.2) and measuring the electrical characteristics of the mentioned devices.

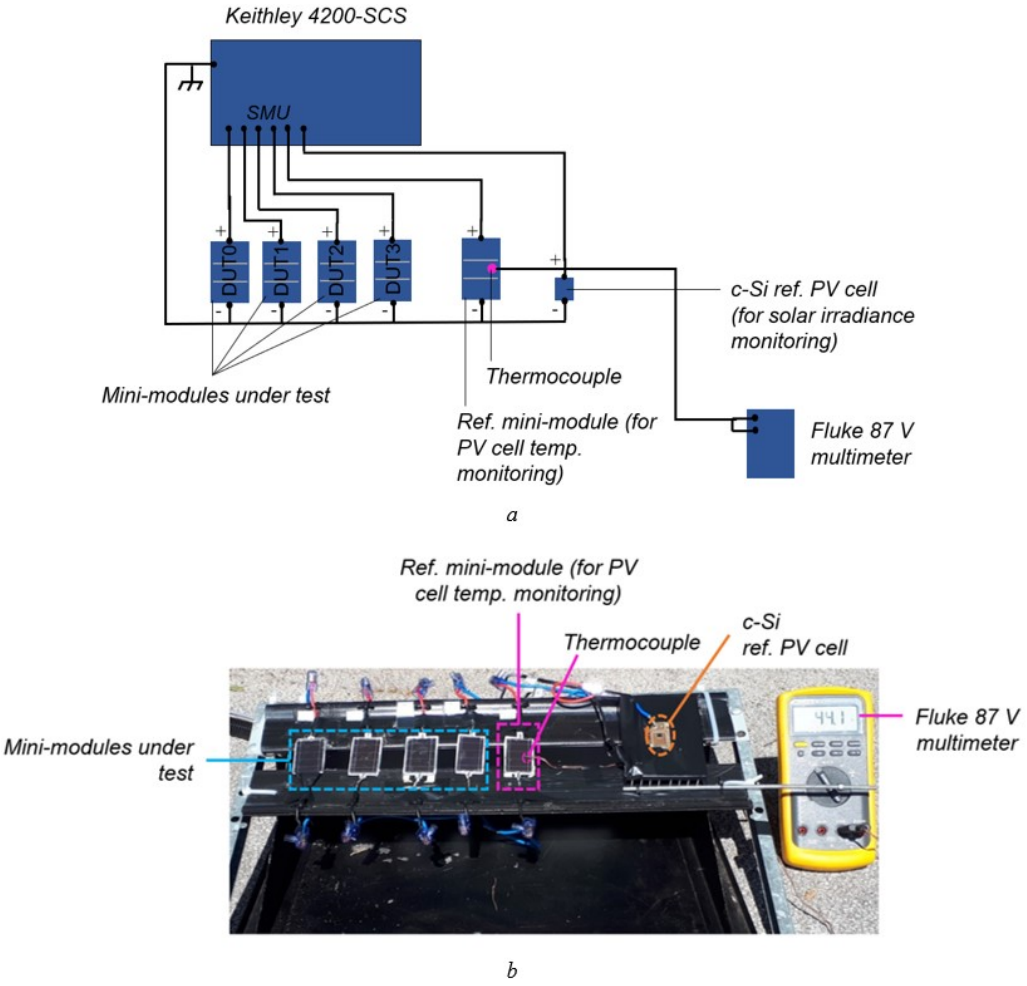

Fig. 3.1 – a. Schematic of the experimental setup used for the tests outdoor; b. photograph of its main components.

Dimensions (active area) [cm^2]	0.237
Short circ. current density (J_{sc}) [A/cm^2]	28.33×10^{-3}
Short circ. current (I_{sc}) [A]	6.714×10^{-3}
Open circ. voltage (V_{oc}) [V]	0.589
Maximum Power Point curr. (I_{MPP}) [A]	6.176×10^{-3}
Maximum Power Point voltage (V_{MPP}) [V]	0.482
Maximum Power (P_{max}) [Wp]	2.975×10^{-3}
Maximum Power density (p_x) [W/cm^2]	12.55×10^{-3}
Power conversion efficiency [%]	12.5
Fill factor (FF) [%]	75
Series resistance (R_{oc}) [Ω]	6.225

Tab. 3.2 – Main characteristics of the c-Si ref. solar cell used for monitoring the solar irradiance during the tests performed outdoor. Note: electrical characteristics measured at the solar simulator in Standard Test Conditions (STC)[8].

Moreover, for some experiments outdoor, the system in Fig. 3.2 was used to measure the solar spectrum evolution in the range from 350 nm to 1100 nm, at various times of the day. The main components of such system are:

- a monochromator (Newport, model: CS130-RG-1-MC);
- an optical fiber, used to collect the incident solar light;
- a Si photodiode, at the monochromator output;
- a PC (on which LabView software running), linked via GPIB to the monochromator and to a digital multimeter (Keithley 6517B ELECTROMETER), used for controlling the monochromator and acquiring the photodiode output current (measured through the electrometer).

[8] namely, at: cell temperature of 25 ±2 °C, irradiance of 1000 W/m^2, with reference spectral distribution, AM 1.5G (*cf.* CEI EN 60904 – 3 Standard).

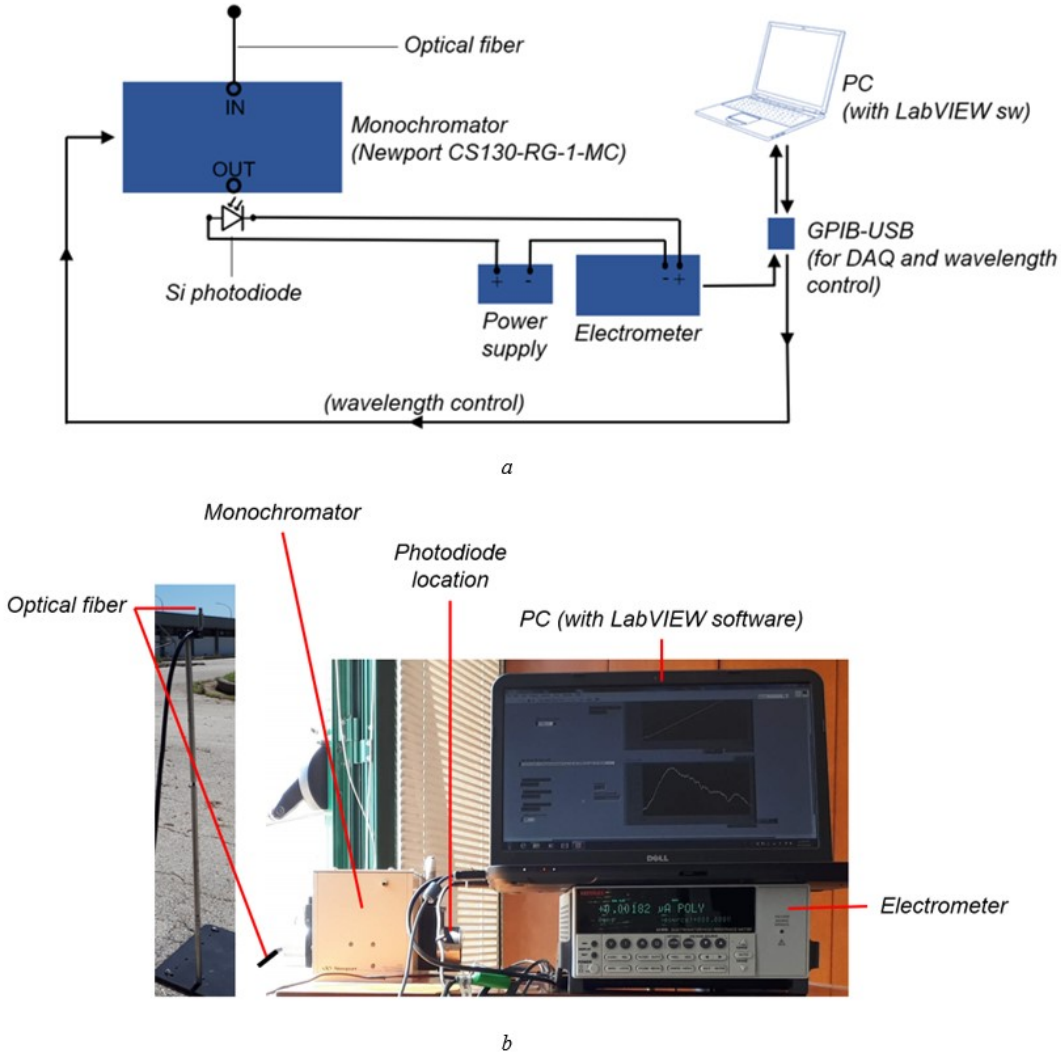

Fig. 3.2 – a. Schematic of the system used for the solar spectrum detection; b. overview of its main components.

For the experiments indoor, the tools listed below were used:

- a Newport (model 92191-1000) CW solar simulator, coupled to a suitable digital exposure controller (see Fig. 3.3);
- a thermostatic chuck (which consists of a sample holder golden plate) coupled to a BENTHAM VC-TE-20 temperature stabilized vacuum chuck controller (see Fig. 3.3);
- the Keithley 4200-SCS instrument (also used for the tests outdoor, as previously described and shown in Fig. 3.1 a).

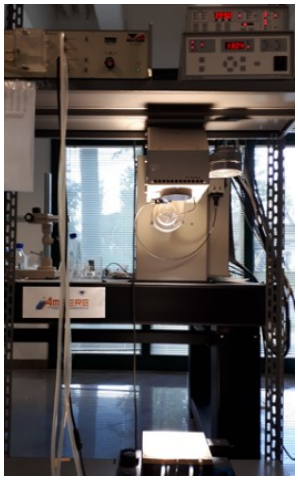

Fig. 3.3 – Overview of the CW solar simulator with its equipment, used for the tests indoor.

3.2.2 Experimental methods

Preliminary tests, aimed to verify the effects of reverse bias DC stresses, were carried out on different groups of mini - modules (each group made up by specimens either non-stabilized, or stabilized[9]), both outdoor under the sunlight and indoor under illumination conditions, obtained via the solar simulator and its equipment (described in section 3.2.1), similar to the ones in the tests outdoor. Such tests were performed according to the test procedure schematically represented in Fig. 3.4 a., as below described. Each test was composed of consecutive stress cycles; at the beginning of each cycle, the current vs. voltage (I-V) electrical characteristics of the PV mini - modules under test and of the reference c-Si solar cell (used for monitoring the irradiance level on the mini - module plane) were measured, via the Keithley 4200-SCS instrument (mentioned in section 3.2.1). Moreover, within each cycle, a specimen (taken as a reference mini - module for the group under test) worked (for 600 s) at constant voltage in its Maximum Power Point (MPP), while the remaining specimens worked either in their MPP (within the initial 300 s of the cycle) or under different reverse bias DC stress conditions applied on them (within the remaining 300 s).

Subsequently, further tests outdoor was carried out on stabilized specimens exclusively, in order to study performance instability phenomena affecting them. The latter tests were performed similarly to the previous ones, with the major difference that in each cycle all the specimens worked (for a total duration of 600 s) at constant voltage in their MPP solely (see test procedure schematized in Fig. 3.4 b.). Initially, each test had an overall duration of about 2.5 hours, and it was carried out either during the morning or during the afternoon of a given day, when two consecutive tests were performed for monitoring the mini - module electrical performance during the day considered. In following

[9] Stabilized specimens are those subjected, before the tests discussed herein, to extended light soaking for 1000 hours, instead non-stabilized specimens are those not subjected to such a treatment.

experiments, each test lasted about 4 hours overall, by taking approximately 2 hours before and 2 after mid-day.

All tests outdoor were performed in Catania, Italy (latitude 37° 26' N, longitude 15° 3' E).

In order to investigate the causes of the mentioned instability phenomena on stabilized specimens, during some tests outdoor, in addition to detect the solar spectrum (via the system in Fig. 3.2, described previously), the temperature of the glass covering the reference mini-module (see Fig. 3.1) was measured at the beginning of each measure cycle. From this temperature, the solar cell operating temperature was estimated, by considering the glass thermal conductivity and the incident solar power density on the mentioned mini - module.

Moreover, in the context of the aforementioned cause analysis, some indoor tests were performed to investigate the effect of a thermal heating at moderate temperature on stabilized mini - modules. In such tests, by using the tools in Fig. 3.3, some stabilized specimens were subjected to a thermal stress at the temperature of 50 °C [10], while they worked in MPP condition, under constant illumination of 1.1 SUN with AM1.5G spectrum.

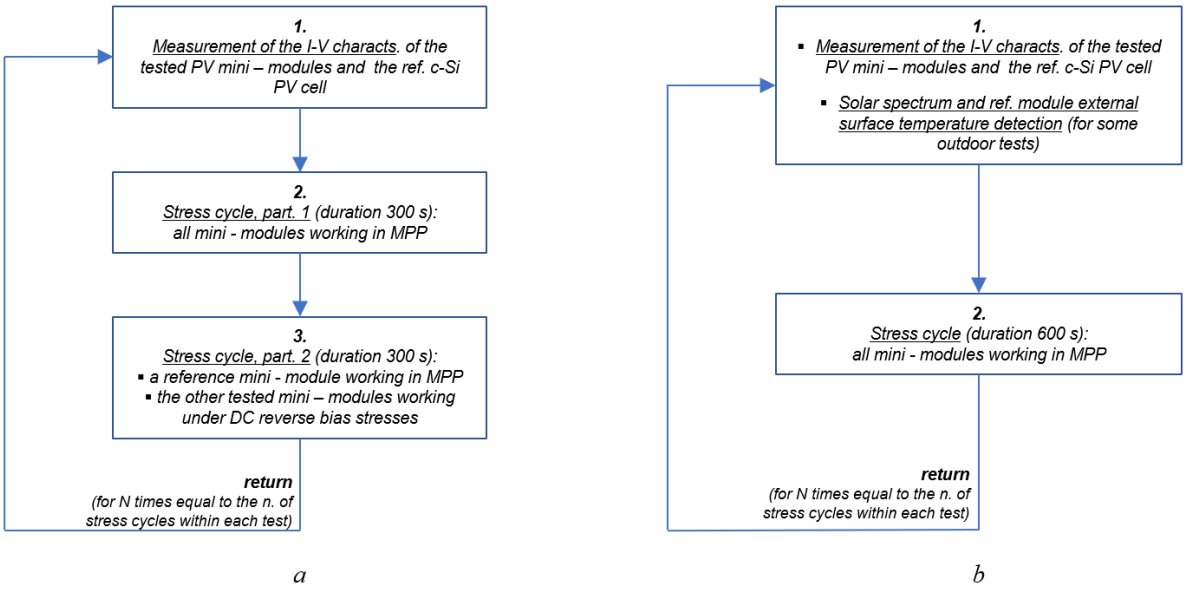

Fig. 3.4 – Schematic representation of the test procedure, for: a. all tests (indoor and outdoor) aimed to verify reverse bias DC stress effects, b. the tests outdoor aimed to study performance instability phenomena affecting stabilized samples, carried out on the PV mini – modules in question.

[10] i.e. a temperature value near to the one achieved by the specimen solar cells during the tests outdoor (as it will be shown later herein).

3.3 Results and discussion

3.3.1 Experiments on non-stabilized specimens under reverse bias DC stresses: main findings

In this section, the effects of reverse bias DC stresses applied on non-stabilized specimens of a-Si/µc-Si PV mini - modules are illustrated and discussed. Fig. 3.5 summarizes the main results of the tests carried out outdoor and indoor (according to the procedure illustrated in Fig. 3.4 a.), on different groups of the mentioned specimens, with an average irradiance of 1.1 SUN approx. in each test and in reverse bias stress conditions characterized by variable voltage levels of -4, -6, -8 V applied to the specimens.

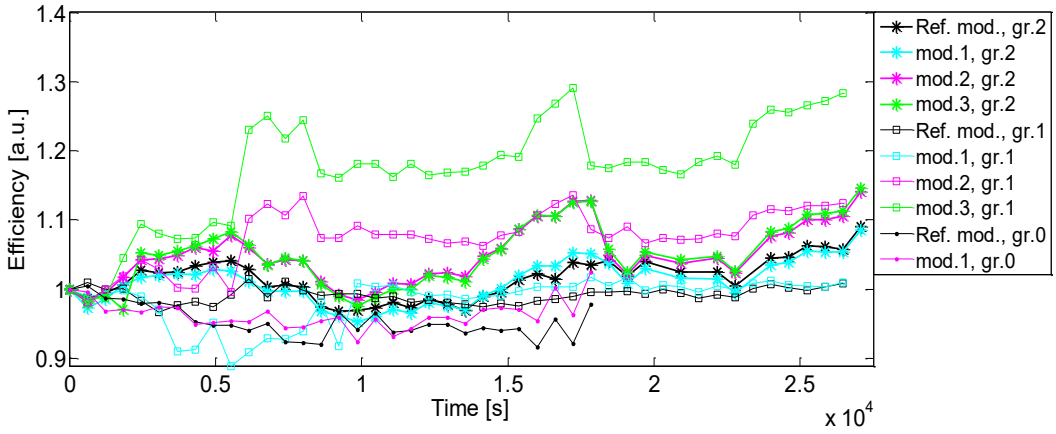

Fig. 3.5 – Normalized power conv. efficiency historical trends of three groups of non-stabilized specimens, subjected to variable reverse bias DC stress conditions (at voltage lev. of -4, -6, -8 V) during several tests on it. Note: groups 0, 2 tested outdoor, group 1 tested indoor at the solar sim.

In particular, the latter figure shows the power conversion efficiency trends for three different groups of non-stabilized specimens, named gr.0, gr.1, and gr.2 (as specified in the figure legend). Among them, two groups (gr.0 and gr.2) were tested outdoor, the remaining group (gr.1) was tested indoor, at the solar simulator. For each of these groups, one mini - module specimen (here called Ref. mod., see the mentioned figure legend) was taken as reference and it worked in its MPP solely (i.e. on it, no reverse bias stresses were applied), while the remaining specimens were subjected to different reverse bias stresses. The group gr.0 consisted of two specimens, a Ref. mod. and another specimen (named mod.1), instead each of the groups gr.1 and gr.2 consisted of four specimens (named Ref. mod., mod.1, mod.2 and mod.3, respectively). For each mini – module group, Tab. 3.3 summarizes the stress sequences applied to the different specimens making up the group considered, which allowed to observe the efficiency experimental trends in Fig. 3.5.

Stress sequence 1	**Stress sequence 2**
(total duration, td: ~ 0.89 x 10^4 s)	(total duration, td: ~ 0.89 x 10^4 s)
Ref. mod. in MPP for td	**Ref. mod.** in MPP for td
mod.1 in MPP for td/2, at – 4 V for td/2	**mod.1** in MPP for td/2, at – 6 V for td/2

a.: **gr.0**

Stress sequence 1	**Stress sequence 2**	**Stress sequence 3**
(total duration, td: ~ 0.88 x 10^4 s)	(total duration, td: ~ 0.88 x 10^4 s)	(total duration, td: ~ 0.88 x 10^4 s)
Ref. mod. in MPP for td	**Ref. mod.** in MPP	**Ref. mod.** in MPP
mod.1 in MPP for td/2, at – 4 V for td/2	**mod.1** in MPP for td/2, at – 6 V for td/2	**mod.1** in MPP for td/2, at – 8 V for td/2
mod.2 in MPP for td/2, at – 6 V for td/2	**mod.2** in MPP for td/2, at – 4 V for td/2	**mod.2** in MPP for td/2, at – 6 V for td/2
mod.3 in MPP for td/2, at – 8 V for td/2	**mod.3** in MPP for td/2, at – 8 V for td/2	**mod.3** in MPP for td/2, at – 4 V for td/2

b.: **gr.1**

Stress sequence 1	**Stress sequence 2**	**Stress sequence 3**
(total duration, td: ~ 0.92 x 10^4 s)	(total duration, td: ~ 0.92 x 10^4 s)	(total duration, td: ~ 0.87 x 10^4 s)
Ref. mod. in MPP for td	**Ref. mod.** in MPP for td	**Ref. mod.** in MPP for td
mod.1 in MPP for td/2, at – 4 V for td/2	**mod.1** in MPP for td/2, at – 6 V for td/2	**mod.1** in MPP for td/2, at – 8 V for td/2
mod.2 in MPP for td/2, at – 6 V for td/2	**mod.2** in MPP for td/2, at – 4 V for td/2	**mod.2** in MPP for td/2, at – 4 V for td/2
mod.3 in MPP for td/2, at – 8 V for td/2	**mod.3** in MPP for td/2, at – 8 V for td/2	**mod.3** in MPP for td/2, at – 6 V for td/2

c.: **gr.2**

Tab. 3.3 – Consecutive stress sequences applied to the non-stabilized specimens making up the three groups of mini – modules considered (a. gr.1, b. gr.2, c. gr.3). These stress sequences allowed to observe the power conversion efficiency experimental trends of Fig. 3.5 for the mentioned specimens.

For all groups, the trends in Fig. 3.5 shows relevant efficiency growths for the specimens on which reverse bias stresses were applied, compared to the mini - modules taken as reference. For instance, an impressive efficiency growth of about 28% was observed for the mod.3 of the gr.1, after DC reverse bias stresses applied for about 3.67 hours overall (of which about 2.44 hours under the stress voltage of -8 V and the remaining time interval under stress voltage of –4 V). Such benefits, observed in terms of the mentioned efficiency growths, are primarily due to the electric field associated to DC reverse bias stress conditions applied to the photovoltaic devices when they are illuminated, as consistent to previous studies in the literature, performed on single solar cells only indoor (as descried herein, section 2.3.1). The power conversion efficiency improvements in Fig. 3.5 are related to a general improvement trend of the main electrical parameters of the specimens subjected to reverse bias stresses, as we can notice from the trends in Fig. 3.6 (where, for instance, the short circuit current density and the series resistance normalized trends of the tested mini - modules are shown) [32].

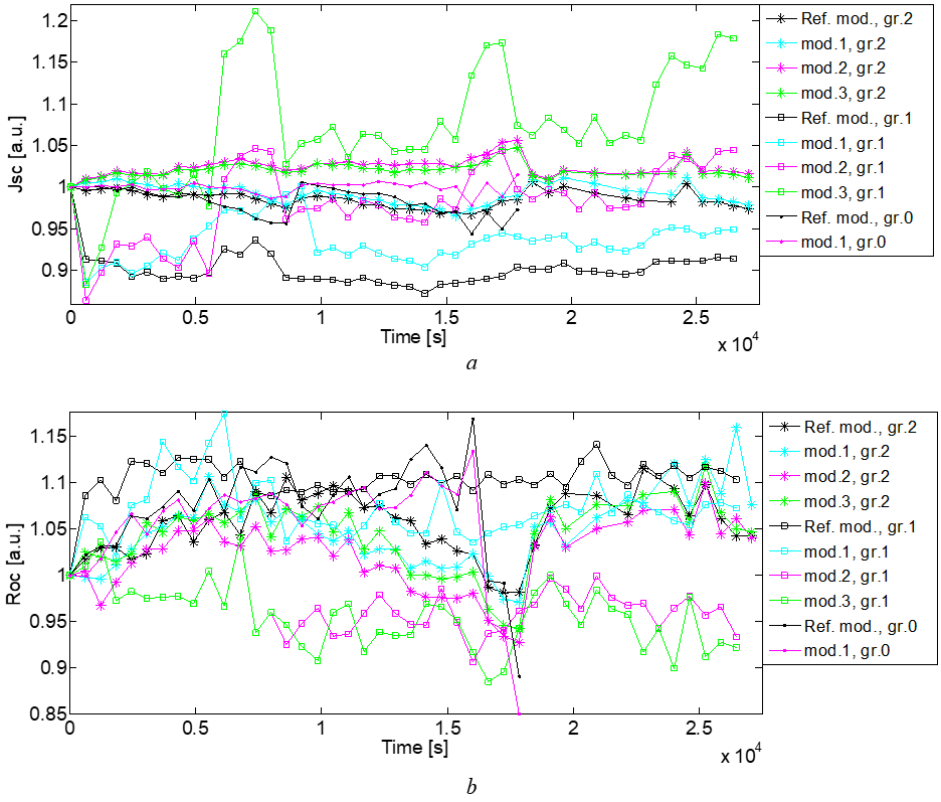

Fig. 3.6 – Norm. (to light intensity and time zero values) trends of a. short circ. current density (Jsc) and b. series resistance (Roc) of the specimens, during the tests of Fig. 3.5.

In Fig. 3.7, the results referred to the group gr.2 of specimens (tested outdoor) are shown in more details.

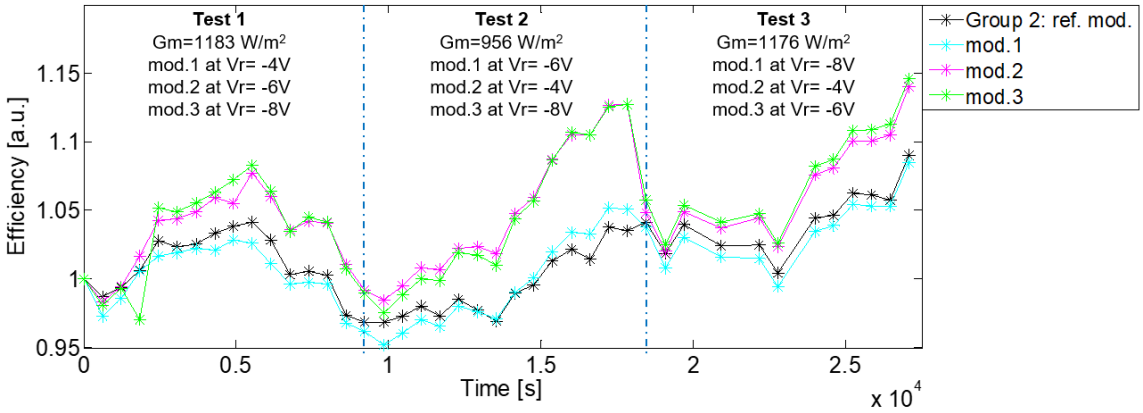

Fig. 3.7 – Normalized power conv. efficiency trends for the group gr.2 of specimens of Fig. 3.5, during the tests performed on it (under the test conditions specified in the legend).

From this figure, we can note that significant efficiency improvements are observable already with the lowest voltage level (of -4V) applied to the specimens and such improvements are often almost the

same or greater than those observed at higher voltage levels (as it is evident in the tests 2 and 3 of Fig. 3.7).

For the case of the test 2 of Fig. 3.7 (which represents the best case, among the tests performed outdoor on non-stabilized specimens), in Fig. 3.8 the normalized trends of the main electrical parameters of the specimens are shown. From such trends is evident that remarkable improvements of these parameters (in terms of norm. Jsc, Voc and FF increases and norm. Roc reduction) occurred for the mini - modules subjected to reverse bias stresses.

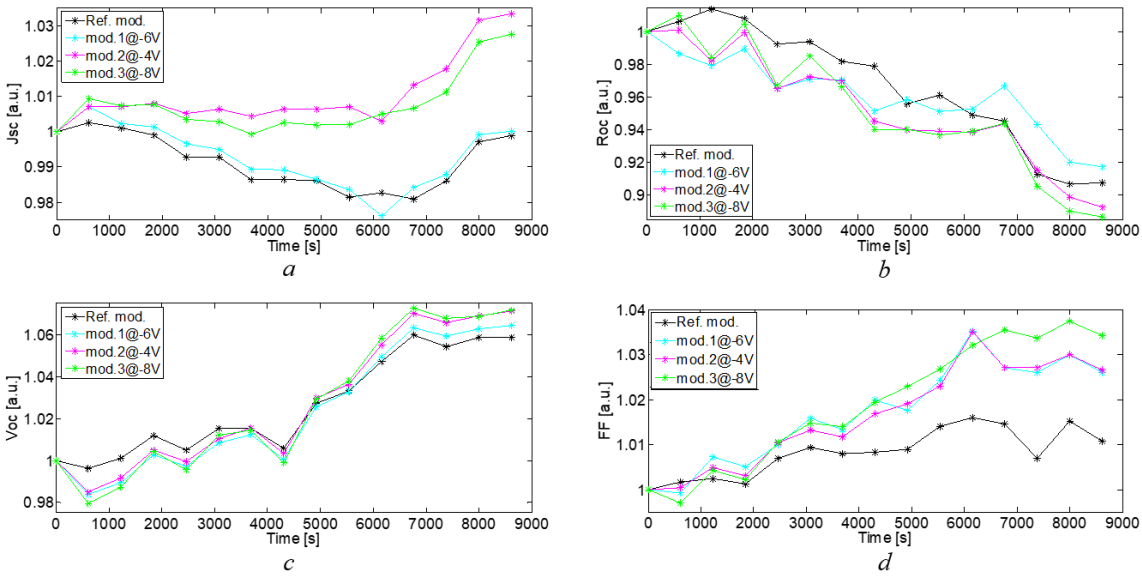

Fig. 3.8 – Normalized trends during the test 2 of Fig. 3.7 of the specimen main electrical parameters: a. short circ. current (Jsc), b. series resistance (Roc), c. open circ. voltage (Voc), d. fill factor (FF). Note: Jsc, Roc, FF trends normalized to the incident light intensity and to the initial values.

In general, as exemplified by the results so far shown, the amount of the observable performance improvements depends on several factors, i.e. essentially the DC reverse bias stress condition supplied (hence the external electric field intensity) and the corresponding stress time, in addition to the illumination conditions of the solar devices.

Regarding the practical convenience of applying DC reverse bias stresses to the a-Si/µc-Si PV devices in order to improve their performance, it is noteworthy that actually a considerable power consumption is necessary to obtain the improvements observed. For example, in the significant case of the mod.3 of the group gr.1 (see Fig. 3.5), a relevant power density of 278 W/m^2 approximately was supplied to carry out all reverse bias stresses on this device. Note that such a power density consumption is higher than the max. electric power density (of 100 W/m^2 approx.) which the photovoltaic module can supply [32]. Moreover, the required stress times are quite long, of the orders of hours, so that the required energy to recover/enhance PV performance is remarkable, of the order of 1 kWh/m^2. Finally, it has to be considered that such PV efficiency improvements are observed on non-stabilized samples,

i.e., on modules not subjected to the usual extended 1000 h light soaking stabilization procedure. This is a crucial aspect that we have studied. In the next section we discuss the results observed on stabilized samples.

3.3.2 Experiments on stabilized specimens: main findings

3.3.2.1 Results of preliminary tests under reverse bias DC stresses

Numerous tests of reverse bias DC stresses performed outdoor on stabilized specimens (according to the same procedure of the tests on non-stab. modules) were performed. A typical example of what happens is reported in fig. 3.9. In this case, all samples, whether or not subjected to reverse bias stress, behave in the same way, i.e., an evident drop of efficiency is observed for all stabilized specimens.

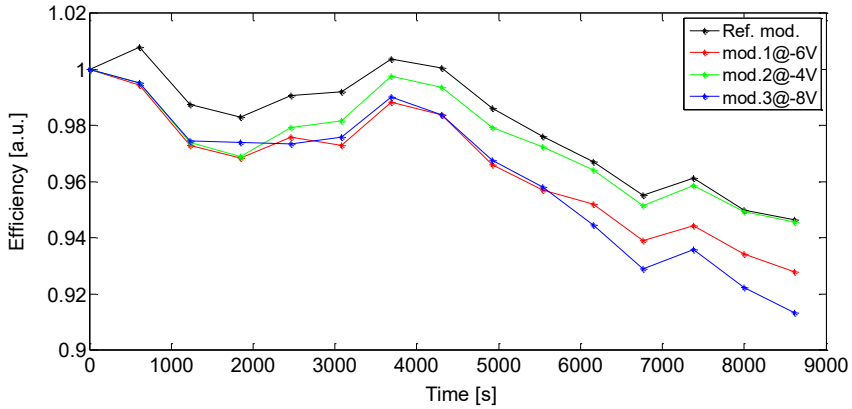

Fig. 3.9 – Overall power conv. efficiency trends of stabilized specimens of a-Si/µc-Si mini - modules, subjected to reverse bias DC stresses, during one of the outdoor tests performed on them.

In numerous tests we have found the same result reported in Fig. 3.9, that is, negligible difference of behavior among reference and reverse biased samples. Therefore, we found that in stabilized modules the application of reverse bias stresses does not determine benefits on the power conversion efficiency of these specimens, in contrast to the results on non-stabilized samples (previously discussed in section 3.3.1).

However, subsequent tests outdoor carried out on stabilized specimens, not subjected to reverse bias DC stresses, led yet to observe relevant instability phenomena on their performance, as it will be shown in the following subsection.

3.3.2.2 Performance instability phenomena on stabilized specimens in MPP outdoor operation

In this section, instability phenomena with reversible variations of electrical performance observed on stabilized specimens of a-Si/µc-Si PV mini - modules working outdoor in their Maximum Power Point (MPP) exclusively, are shown and commented. In Fig. 3.10, the most significant results of initial tests performed outdoor (in July 2017) are illustrated. In these experiments, for each day two consecutive

tests were performed, one during the morning and one during the afternoon, to detect the mini-module performance during the considered day.

At a first glance, from Fig. 3.10 we notice for each day a "U" shape in the efficiency vs. time trend. This is systematic for all samples and all days. A first simple explanation is the module temperature: from morning to mid-day the module temperature increases, while from mid-day to afternoon it decreases. As it is well known, PV module efficiency decreases with temperature, and this produces the "U-shapes" of Fig. 3.10.

Such explanation, however, as described in detail in the following, explains only in part the data. In fact, the considerable power conversion efficiency variations, with a remarkable efficiency improvement in the afternoon, are systematically detected from the morning to the afternoon in all specimens. Furthermore, at the early stages of the morning outdoor tests, the modules maintain initially the larger efficiency found at the end of the previous afternoon.

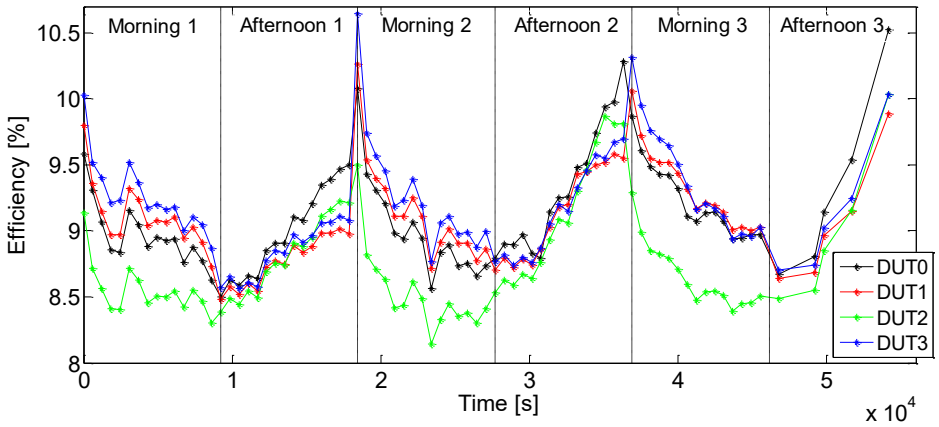

Fig. 3.10 - Overall power conversion efficiency vs. stress time trends for the tested stabilized specimens (named DUT0, DUT1, DUT2, DUT3 [11]) working in MPP, during tests performed outdoor in July 2017.

For example, considering the Afternoon 1 case, from the Fig. 3.11, where the normalized trends to the incident illumination of the main electrical parameters of the tested mini - modules are plotted, we note that the efficiency improvements shown in Fig. 3.10 are associated to a general improvement of these parameters. In particular, we observe a significant decrease of normalized series resistance (Roc), together with growths of normalized open circuit voltage (Voc), short circuit current density (Jsc) and fill factor (FF).

[11] DUT is the acronym of Device Under Test.

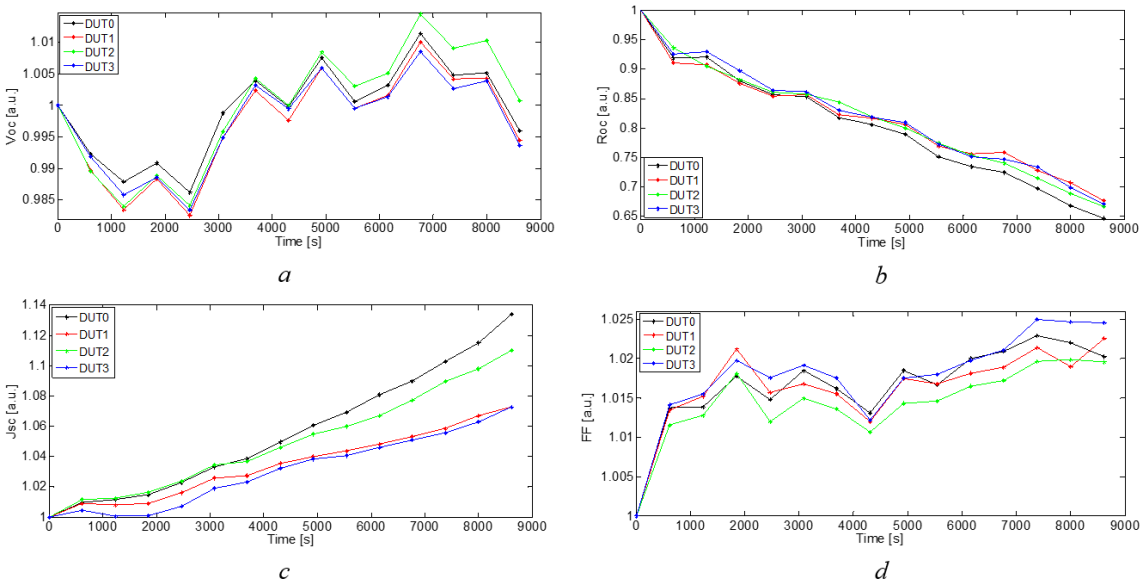

Fig. 3.11 - Main electrical parameters normalized trends of the tested PV mini - modules, during the Afternoon 1 test of Fig. 3.10: a. open circuit voltage (Voc), b. series resistance (Roc), c. short circuit current density (Jsc), d. fill factor (FF). Note: trends normalized to the incident solar irradiance and to the initial values of the considered parameters.

Consistently with different studies in the literature (see herein chapter 2), the performance improvements systematically observed in the afternoon for the tested mini - modules working in MPP in outdoor conditions can be also attributed to two additional possible causes, essentially: firstly, a thermal annealing at moderate temperature of the mini - modules during the morning, which most likely involves an annealing of the defects formed during light soaking in MPP, ultimately leading to power conversion efficiency improvements in the afternoon for the PV devices in question; second, an effect of any solar spectrum variation on going from the morning to the afternoon. Such additional causes and the role played by the module temperature will be analyzed in depth and demonstrated in the following section 3.3.2.3.

For the dual purpose of investigating in depth on the mentioned causes and to confirm the reversible effects observed in the initial experiments, by checking the results repeatability on a daily scale, we carried out further tests outdoor on another different group of stabilized specimens, working also in this case in their MPP under sunlight and variable illumination and temperature conditions. The latter tests were performed between February and May 2019, with the only difference, compared to the previous outdoor tests (of July 2017), that each test lasted about 4 hours overall, by taking approximately 2 hours before and 2 after mid-day. In such tests we monitored the solar cell temperature and over the course of different days we measured also the solar spectrum evolution (by using the measurement systems described in section 3.2.1).

Fig. 3.12 shows the main results of the latter tests, where the power conversion efficiency (see Fig. 3.12 a) and the solar cell temperature (see Fig. 3.12 b) time evolution for different test days are plotted.

Similarly to the previous tests of July 2017, also in the most recent experiments of Fig. 3.12 an evident effect of power conversion efficiency worsening in the morning followed by improvements in the afternoon is observable systematically again. Furthermore, as it will be discussed in more detail later herein (see section 3.3.2.3), a clear correlation exists between the tested mini-module efficiency and the temperature of the mini-module solar cell: actually, the efficiency improvements take place evidently after mid-day, i.e. subsequently to a significant thermal heating of the solar cells during the morning and up to about mid-day, essentially due to the increasing solar irradiance.

The reversible efficiency variation highlighted in Fig. 3.12 are generally related to reversible changes of the other main electrical parameters of the tested mini - modules (i.e. the open circuit voltage, Voc, series resistance, Roc, short circuit current density, Jsc, and fill factor, FF), as it is shown for example in Fig. 3.13 for the day 2 test of Fig. 3.12.

We note that after a worsening of the considered parameters during the morning, in the afternoon a trend toward an improvement takes place. Such an improvement is particularly evident for the normalized Roc which decreases and the Voc which increases. This involves an overall improvement of the tested mini-module electrical performance, which is mainly due to the thermal annealing of the solar cells, as it will be demonstrated and further discussed in the following paragraph.

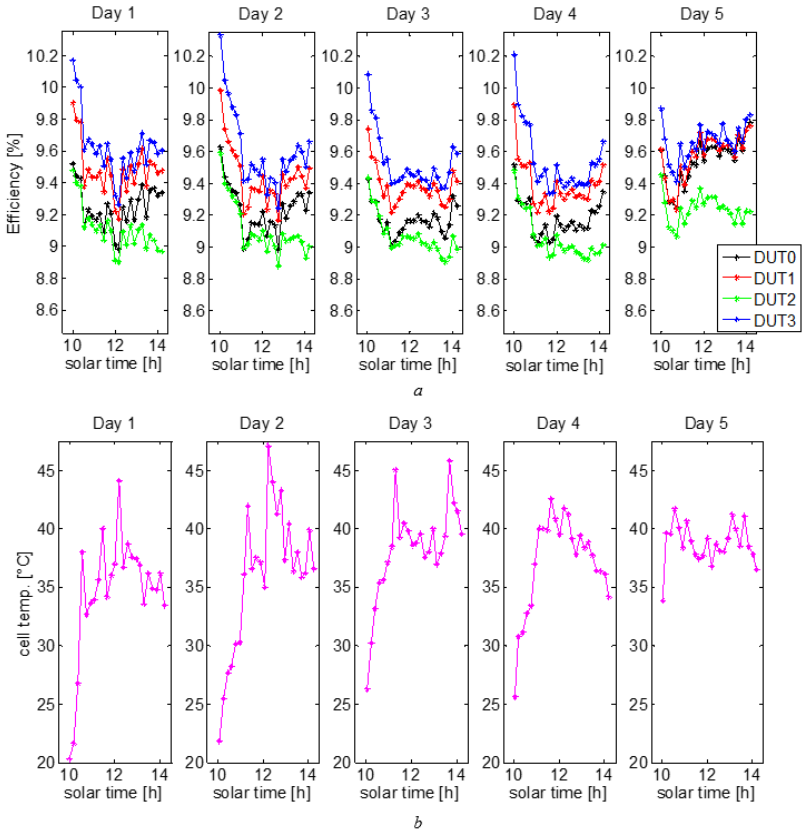

Fig. 3.12 - Trends, as a function of local solar time (UTC+1) during outdoor tests, performed between Feb. and May 2019 on a group of stabilized specimens (named DUT0, DUT1, DUT2, DUT3) of

tandem a-Si / µc-Si PV mini – modules working in MPP: a. specimen power conversion efficiency; b. solar cell operating temperature.

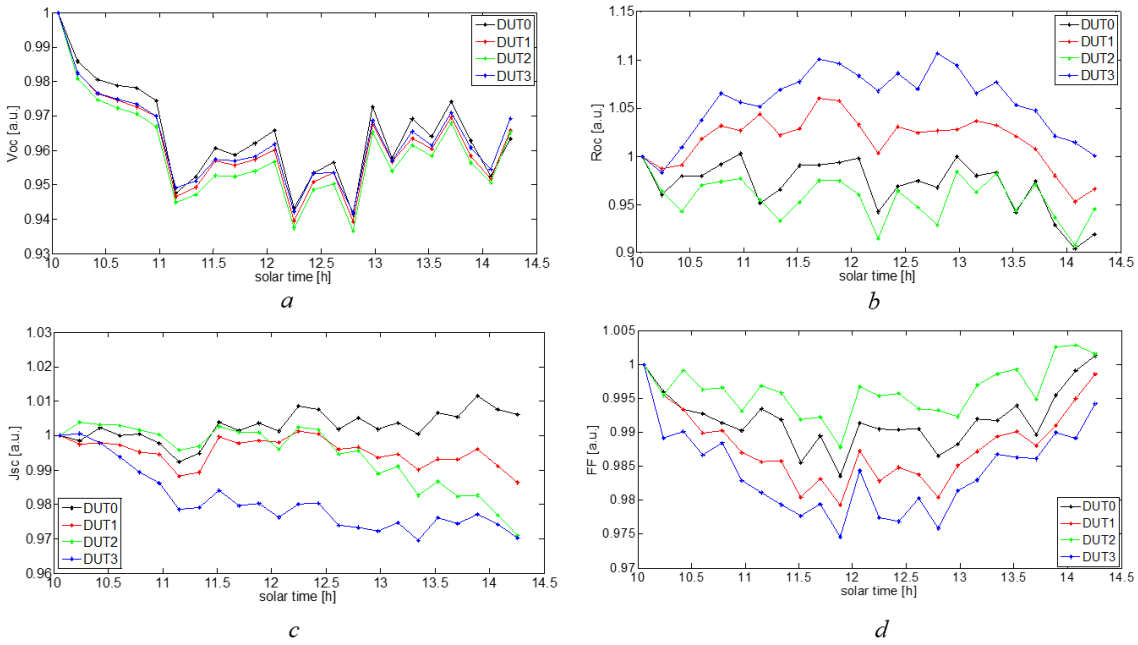

Fig. 3.13 – Main electrical parameters normalized trends, as a function of local solar time (UTC+1), for the tested PV mini - modules during the day 2 test of Fig. 3.12: a. open circuit voltage (Voc), b. series resistance (Roc), c. short circuit current density (Jsc), d. fill factor (FF). Note: trends in a. normalized to the initial values of the mini – modules' Voc. Trends in b., c., d. normalized to the incident light intensity and to the considered parameters initial values.

3.3.2.3 Causes of the instability phenomena observed in outdoor MPP operation: in-depth analysis

To analyze the causes of the instability phenomena observed on stabilized mini - modules working outdoor in their MPP (shown in previous section 3.3.2.2), firstly the correlation between the tested mini - module electrical performance variations and the changes of mini - module solar cell temperature has been studied in depth.

Fig. 3.14 highlights such correlation, with reference to the test days of Fig. 3.12, by showing the tested mini-module power conversion efficiency as a function of the PV cell operating temperature during the mentioned test days.

Although the experimental data of Fig. 3.14 show some variations from a case to the other, however they can be schematized as shown in the sketch of Fig. 3.15, which ideally represents the electrical behavior of a single PV mini-module working in its MPP, when different cell maximum temperatures are achieved. As it is well known, typically when a solar cell temperature grows, its power conversion efficiency decreases. However, together with such usual behavior, the a-Si:H / µc-Si tandem solar cells are characterized by an additional phenomenon of efficiency improvement. In fact, moving toward the

afternoon hours, the efficiency goes up again to higher values since the cell temperature decreases; nevertheless, it should be noted that the efficiency in the afternoon does not return to the morning value at the same temperature, but it achieves a higher value.

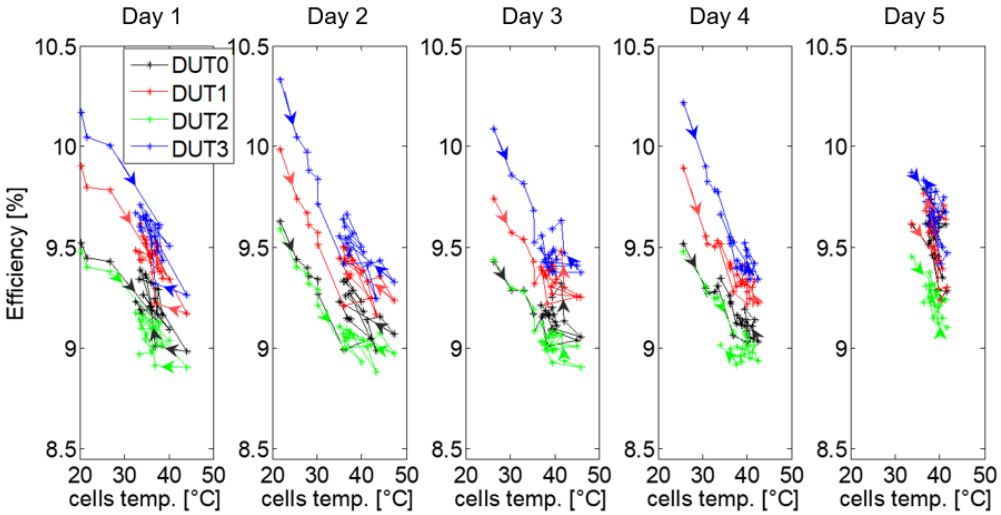

Fig. 3.14 - Power conversion efficiency of the tested mini - modules vs. PV cell operating temperature, during the test days of Fig. 3.12. Note: the arrows on the curves indicate the direction of the time evolution.

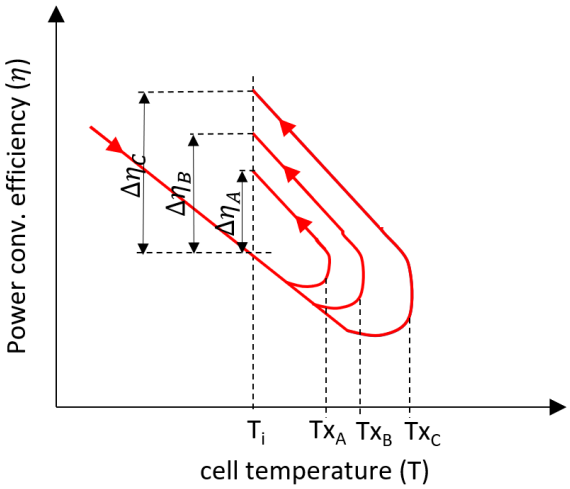

Fig. 3.15 - Scheme of the electrical behavior of a single mini-module as the operating temperature of its solar cells changes: power conversion efficiency trends, as they can be deducted by the experimental ones of Fig. 3.14. Note: Tx_A, Tx_B, Tx_C represent three different increasing values of the maximum operating temperature achieved by the cells. The arrows on the curves indicate the direction of the time evolution.

To explain these results, it should be considered that an additional phenomenon exists, due to the annealing of the defects generated during light soaking in MPP. This annealing involves an improvement of the PV cell efficiency, so that some sort of hysteresis effect is observable. Substantially, by starting

in the morning from a cold solar cell with high efficiency, while the cell operating temperature rises due to the solar irradiance, three different effects occur concurrently: 1. the PV device efficiency decreases, as a result of the cell temperature growth; 2. the PV device efficiency drops, because the Light Induced Degradation (LID) occurs for the light soaking during the cell MPP operation; 3. around noon, the solar cells achieve their highest operating temperature (Tx_A, or Tx_B, or Tx_C in the scheme of Fig. 3.15). This determines a moderate thermal annealing involving some defect annealing, by ultimately leading to an efficiency improvement. For increasing values ($Tx_A < Tx_B < Tx_C$) of maximum operating temperature achieved by the solar cells, increasing growths of power conversion efficiency ($\Delta\eta_A < \Delta\eta_B < \Delta\eta_C$, obtained by comparing morning and afternoon values at the same cell temperature) occur, because of the increasing intensity of the solar cell thermal annealing. To uphold the correctness of the scheme of Fig. 3.15, we observe again the experimental trends of Figs. 3.12, 3.14. For instance, we focus on the efficiency of the specimen DUT0 and the temperature trends during the tests of the days 2 and 4. In such tests, the cell maximum temperature values were quite different, i.e. 47.1 °C and 42.6 °C, respectively; and actually, by considering the same cell temperature (36 °C), the efficiency growth ($\Delta\eta$) from the morning to the afternoon is higher in the day 2 test (3.79% approx.) compared to the day 4 test (1.25% approx.).

The complex behavior above described, due to the combination of different phenomena, determines sensitive changes in the estimation of the power conversion temperature coefficient of such type of PV devices. For instance, in the day 2 test, the temperature coefficient of the DUT0 is about -0.23%/°C, if we consider the experimental data points of the morning exclusively. But, if we consider all the experimental data points, by including the morning, when the cells achieve their maximum operating temperature, and the afternoon measurements, the temperature coefficient becomes significantly lower, namely -0.20%/°C approximately.

Fig. 3.16 shows the trends of the mini – module main electrical parameters as a function of solar cell temperature, during the day 2 test of Fig. 3.14. These trends are similar to those of the power conversion efficiency, resulting in an overall improvement of the electrical performance which can be attributed to the cell thermal heating occurred around mid-day. We note that the most affected parameters are the open circuit voltage (Voc) and the series resistance (Roc). For instance, the Voc parameter exhibits values in the afternoon evidently higher than those in the morning, for the same cell temperature value. This aspect will be further discussed later in such paragraph.

Continuing the analysis on the causes potentially responsible for the observed instability phenomena, we have also checked if the tested specimen performance variations, detected in the outdoor tests, are in some way linked to solar spectrum changes during the day. For this purpose, we measured the solar spectrum evolution from the morning to the afternoon for various days. For instance, Fig. 3.17 a. illustrates the solar spectra detected at different local solar times of the day 5 test of Fig. 3.12. Each

spectrum plotted in Fig. 3.17 has been normalized to its maximum value, in order to facilitate the comparison among spectra at different hours. By observing Figure 3.17 a., we see clearly that the blue component of the spectrum grows on going from the morning to the afternoon hours. Such a solar spectrum change from the morning to the afternoon hours is well reproducible and it has been observed in different days (as for instance it is shown in Fig. 3.17 b.). Similar variations were observed in some studies in the literature (see [68],[72]), where it was explained that the solar spectrum shifting towards the blue during the day is due to a growth during the day of water vapor density in the atmosphere.

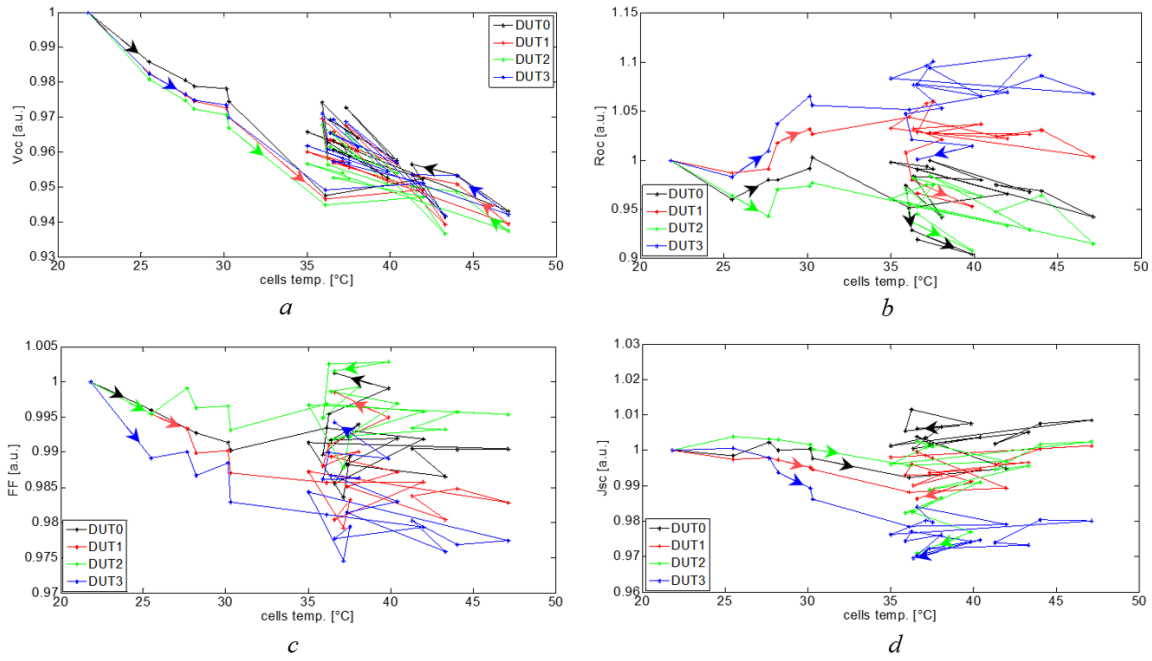

Fig. 3.16 - Trends, during the day 2 test of Fig. 3.14, of the specimen main electrical parameters, as a function of the cell operating temperatures: a. open circuit voltage (Voc); b. series resistance (Roc); c. fill factor (FF); d. short circuit current density (Jsc). Note: trends in a. normalized to the initial values of the specimen Voc (i.e. the Voc values at the beginning of the day 2 test). Trends in b., c., d. normalized to the incident light intensity and to the initial values of the considered parameters. The arrows on the curves indicate the direction of the time evolution.

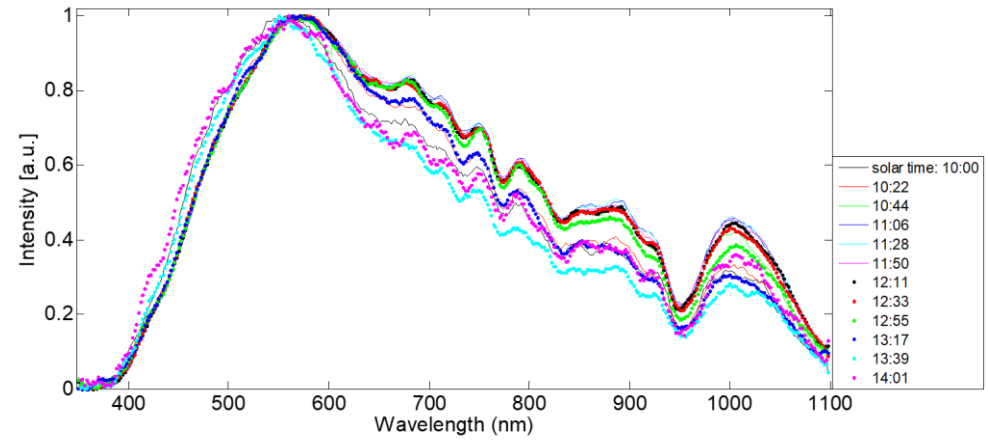

a

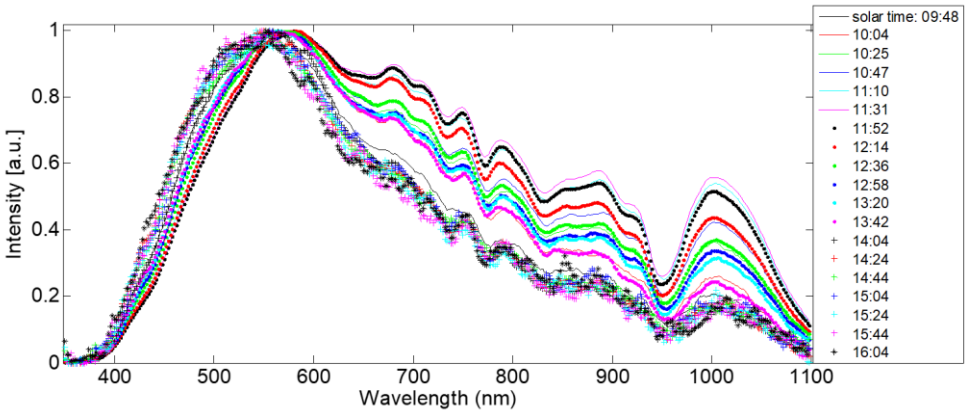

b

Fig. 3.17 - Solar spectrum changes, detected over the course of different days in May-June 2019: a. solar spectra at different solar times during the day 5 test of Fig. 3.12, b. solar spectra at different solar times during another test day. Note: the measured solar spectra, not corrected for the EQE of the photodetector used, have been normalized to their respective maximum values.

Hence, it could be hypothesized that the photovoltaic device efficiency variations occurring on going from the morning to the afternoon hours are attributable to the observed solar spectrum changes. But this is not the case. Actually, the observed efficiency variations are essentially due to the aforementioned annealing phenomena occurring around mid-day, rather than the solar spectrum changes. This will be demonstrated later, through an in dept analysis of the time evolution of the tested PV device main electrical parameters.

Hence, to highlight the cause of the observed efficiency variations, we have studied such a time evolution. For this purpose, we assume that the cell parameters most influenced by the spectral changes should be the fill factor and the short circuit current, as proposed in [68]. Indeed, it is well-known that typically a solar cell has a not flat external quantum efficiency (EQE) curve along the solar spectrum. Therefore, it is expected that, by varying the shape of incident solar spectrum, for the same flux of incident photons, a variation of the solar cell short circuit current (Isc) should occur. So, if we consider

for instance a solar cell with a higher EQE in the blue - green wavelength range, if an incident spectrum variation toward the blue – green occurs (i.e. if the weight of the blue – green component of the spectrum increases), it is expected that this cell exhibits a higher Isc.

In Fig. 3.18, the time evolution, during the test days of Figs. 3.12 and 3.14, of normalized short circuit current density, fill factor and open circuit voltage is illustrated, for all the tested specimens. Moreover, Tabs. 3.4 and 3.5 summarize the percentage variations of the electrical parameters of Fig. 3.18, observed for each test day on going from the morning to the afternoon. These variations have been obtained for each test day by considering two different hours of the morning and of the afternoon, when similar solar irradiance values were present, but the solar spectrum had different shapes.

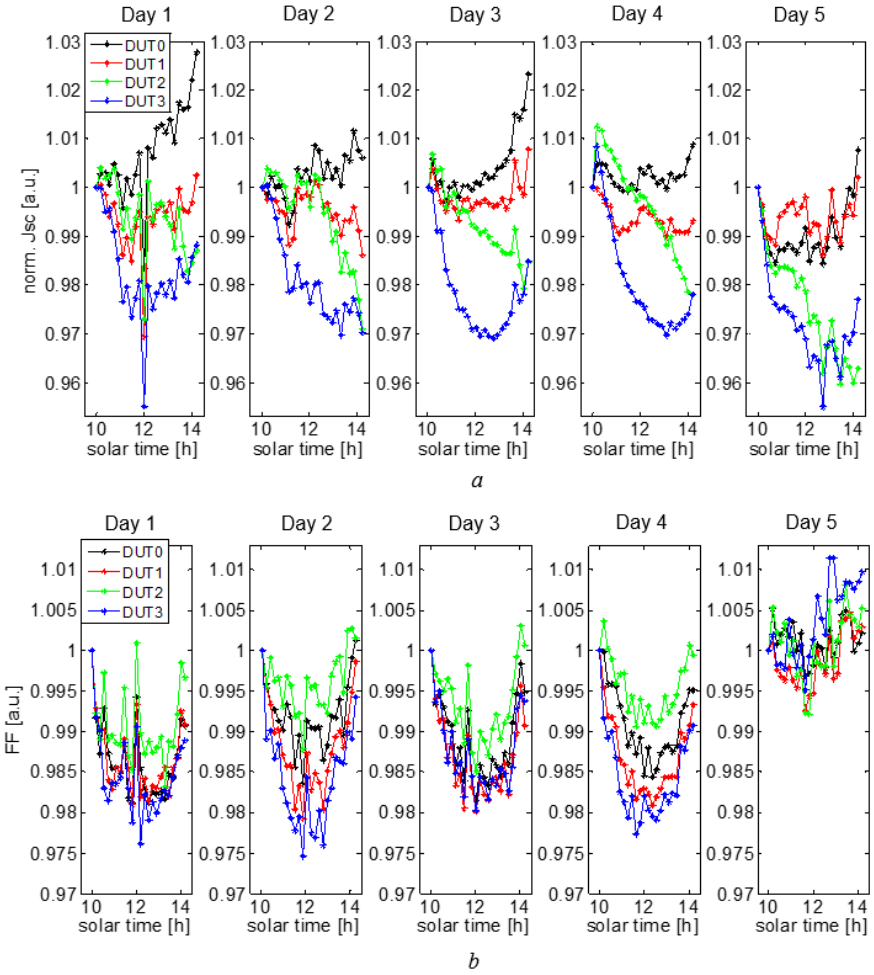

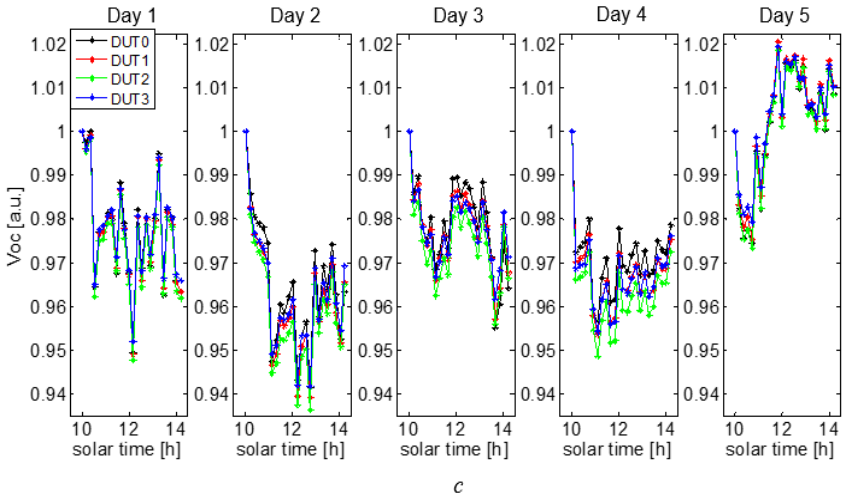

c

Fig. 3.18 - Normalized trends, during the outdoor test days of Figs. 3.12, 3.14, of: a. short circuit current density (norm. Jsc), b. fill factor (FF), c. open circuit voltage (Voc) of the tested specimens. Note: Jsc trends in a. are normalized to the incident light over the specimen surface in each measure cycle and to the initial values at the beginning of each test. FF and Voc trends, in b. and c., are normalized to the initial values at the beginning of each test.

Test Day	Solar times (UTC+1)	Δirr. [%]	Δcell Temp. [%]	Δeff. [%]	ΔJsc,norm. [%]	ΔFF [%]	Δvoc [%]
1	10:34 13:40	+0.01	-8.15	+2.54	+1.50	-0.84	+1.78
2	11:20 12:59	-0.68	-11.00	+2.49	+0.71	-0.37	+2.04
3	11:08 12:58	+0.76	+3.95	+1.31	+0.30	0.00	+0.98
4	11:06 13:17	-0.47	-3.05	+0.97	+0.30	-0.40	+1.06
5	11:06 12:55	-1.30	-3.76	+2.90	+0.04	+0.28	+3.16

Tab. 3.4 – Percentage variations of DUT0 specimen el. parameters (power conv. eff., Jsc,norm., FF, Voc) during the test days of Figs. 3.12, 3.18. To calculate these var. for each test day, two different solar times were considered, with similar global irradiance values on the specimen surface but different solar spectrum shapes. The percentage variations of irradiance (Δirr.) and of PV cell temperature (Δtemp.) between such solar times are indicated too. A positive percentage value represents a parameter increase from the morning to the afternoon.

Test Day	Solar times (UTC+1)	Δirr. [%]	Δcell Temp. [%]	Δeff. [%]	ΔJsc,norm. [%]	ΔFF [%]	Δvoc [%]
1	10:34 13:40	+0.01	-8.15	+1.64	+0.12	-0.46	+1.92
2	11:20 12:59	-0.68	-11.00	+2.30	+0.42	-0.07	+1.84
3	11:08 12:58	+0.76	+3.95	+1.15	+0.06	+0.10	+0.96
4	11:06 13:17	-0.47	-3.05	+1.05	+0.28	-0.14	+0.87
5	11:06 12:55	-1.30	-3.76	+2.65	-0.52	+0.01	+3.17

Tab. 3.5 - Percentage variations of DUT1 specimen el. parameters (power conv. eff., Jsc,norm., FF, Voc) during the test days of Figs. 3.12, 3.18. Such variations were calculated as those in Tab. 3.4. The percentage variations of irradiance (Δirr.) and of PV cell temperature (Δtemp.) between such solar times are indicated too. A positive percentage value represents a parameter increase from the morning to the afternoon.

By observing the tables above, at a first glance we see that the open circuit voltage (Voc) exhibits noticeable variations, instead the normalized short circuit current density (Jsc,norm.) and the fill factor (FF) vary remarkably less. The most relevant fact is the following. Although the solar spectrum varies considerably between the times in the tables, the Jsc,norm., which typically represents the PV cell most sensitive parameter to spectral changes, varies negligibly compared to the Voc. The latter is the electrical parameter most affected by PV cell temperature changes. Such fact leads to conclude that the remarkable power conversion efficiency improvements observed are not referable to the measured solar spectrum variations, which as a matter of fact produce weak changes of Jsc,norm. Instead, they are primarily due to a thermal phenomenon concerning the tested mini – modules, by ultimately leading to a growth of Voc (hence to an improvement in the lifetime of charge carriers in the PV cells).

On the other hand, by observing the Voc trends as a function of the PV cell temperature (shown in Fig. 3.19), it is evident that, for a given PV cell temperature value, a significant Voc increase takes place, from the morning to the afternoon of each test day. This is consistent with the detected trends of the tested PV device power conversion efficiency, previously shown in Fig. 3.14. Ultimately, these increases of Voc are primarily due to the thermal annealing of defects in the mini – modules, reversibly generated during the morning light soaking stage. Hence, this defect annealing is to be considered the main cause of the module efficiency improvements observed on a daily scale by passing from the morning to the afternoon hours [73].

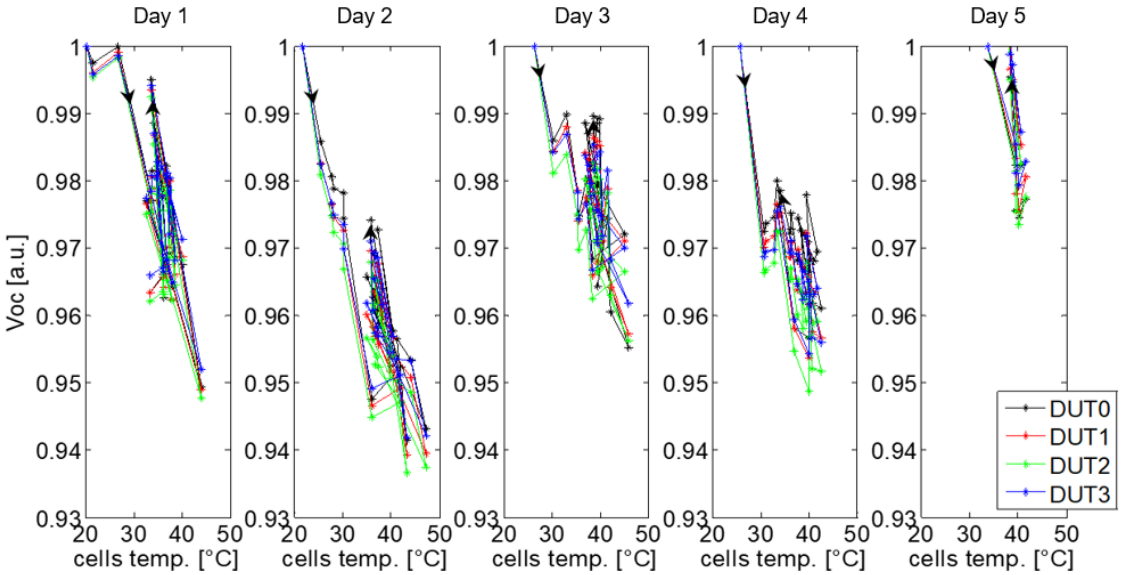

Fig. 3.19 - Normalized trends of open circuit voltage (Voc) vs. operating cell temperature, for the tested specimens over the course of the outdoor test days of Figs. 3.12, 3.14. The arrows on the curves indicate the direction of the time evolution.

As further proof of the fundamental role played by the cell operating temperature for the electrical performance of the tested PV mini – modules, the thermal behavior of such devices was checked indoor too. By using the tools for the indoor experiments previously described in section 3.2.1, some stabilized specimens (like that tested outdoor) were subjected to thermal stress tests indoor. The aim of such tests was to check also in indoor conditions the effect induced by the thermal annealing at moderate temperatures on the specimen electrical performance. For instance, Fig. 3.20 illustrates such an effect for a specimen, subjected to a thermal stress test at about 50 °C, while it worked in its maximum power point (MPP) under a constant illumination of 1.1 SUN with AM1.5G spectrum (ensured by the solar simulator depicted in Fig. 3.3) [32]. It should be noted that the mentioned thermal stress test indoor was performed at conditions similar to those of the tests outdoor (i.e. by keeping for about 1 hour the specimen, working in its MPP, at a temperature near to that achieved around midday by the mini – module PV cells during the outdoor tests).

As it clearly appears from fig. 3.20, during the indoor thermal stress test an evident electrical performance improvement occurred for the tested specimen, in terms of an increase of maximum power point current and consequently of power conversion efficiency. This fact again confirms the benefit which the thermal annealing at moderate temperatures is able to determine on the performance of the PV devices analyzed and the fundamental role played by the temperature achieved by the solar cells during their operation.

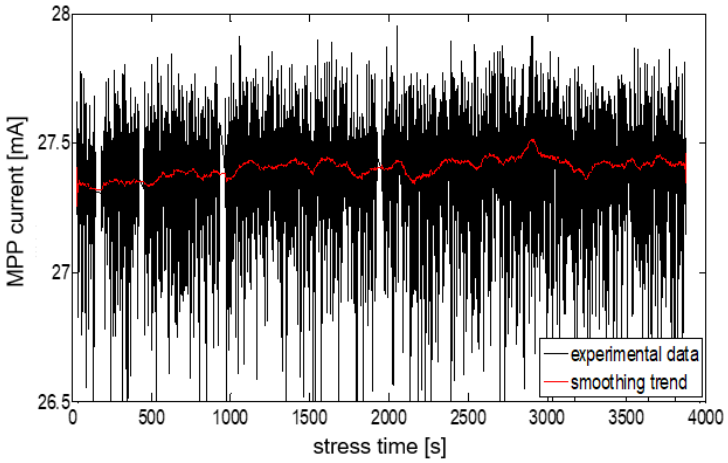

Fig. 3.20 – Effect on the el. performance, induced by a thermal stress test carried out indoor at 50°C and at 1.1 SUN, AM1.5G (CW solar simulator) on a stabilized specimen of a-Si/μc-Si PV mini – module working in its MPP: trends of MPP current (red curve obtained through an appropriate smoothing operation on the exp. data black curve).

CHAPTER 4 MAJOR CONCLUSIONS OF THE RESEARCH ACTIVITY ON TANDEM AMORPHOUS / MICROCRYSTALLINE SI PV DEVICES

Based on the experimental research activities carried out in this work on thin film tandem amorphous / microcrystalline Silicon PV devices and discussed in the previous chapter 3, the major conclusions here presented can be drawn.

Firstly, regarding the effects induced by DC reverse bias stresses applied on the mentioned devices under illuminations, the outdoor tests performed on non-stabilized PV mini-module samples have confirmed the following. The mentioned stresses allow to improve the performance of these devices significantly, consistently with the benefits observed in the literature (see, for instance [21]) in indoor conditions (under the illumination provided by a solar simulator) on single solar cells. Generally, the amount of the performance improvements depends on several factors, namely: the DC reverse bias stress condition supplied (hence the external electric field intensity) and the corresponding stress time, in addition to the illumination conditions of the PV devices. Although remarkable power conversion efficiency increases were observed on non-stabilized samples (up to 28%, after DC reverse bias stresses of -4, -8 V, applied for about 3.68 hours, under the irradiance of 1.1 SUN approx.), it is noteworthy that the application of such reverse bias stress technique, for improving the performance of this type of PV devices, appears not convenient. Actually, to obtain the efficiency improvements observed, a relevant consumption in terms of power density (of the order of 278 W/m^2), higher than the maximum electric power density (of 100 W/m^2 approx.) which a single PV mini - module can supply, was estimated. Furthermore, in the case of reverse bias stress conditions applied to tandem mini-module stabilized samples in outdoor condition, no performance improvement was observed.

The reversible performance instability phenomena detected and thoroughly studied on stabilized samples of the aforementioned devices working in MPP in outdoor conditions are of great interest. In this regard, we observed clear reversible effects of power conversion efficiency instability on going from the morning to the afternoon, well repeatable on a daily scale. The correlation among the mini-module electrical performance trends, the PV cell temperature and the solar spectrum variations was analyzed in-depth. A high reproducibility of the trends of all electrical parameters was seen for the various test days and tested mini - modules. Essentially, the following dynamics are highlighted by the experimental tests performed: 1. initially, in the morning, the Light Induced Degradation occurs and defects are generated, due to the light soaking; 2. subsequently, around mid-day, a thermal annealing of the defects generated in the morning occurs; 3. in the afternoon, an improvement of the PV device power

conversion efficiency occurs, as a consequence of the mid-day defect annealing. Such phenomenon, which involves significant variations of PV device electrical performance, is repeatable on a daily scale. The main cause of this instability effect consists in the variations of solar cell operating temperature, while the solar spectrum variation, even if existing, plays a minor role. The most important finding is that the moderate thermal annealing, which takes place when the solar cells achieve their maximum temperature, actually produces a defect annealing. It results in a power conversion efficiency improvement. The experimental results provide clearly the following information. The higher is the maximum temperature achieved by the solar cells during their operation (i.e. the more intense is the solar cell thermal annealing occurring), the higher the observable power conversion efficiency growth becomes (see Fig. 4.1). In other words, to an increase of the solar cell maximum operating temperature corresponds an increase of the power conversion efficiency growth, observed by comparing (for a given day) the morning and afternoon efficiency values at the same cell temperature. This is due to the increasing intensity of the solar cell thermal annealing.

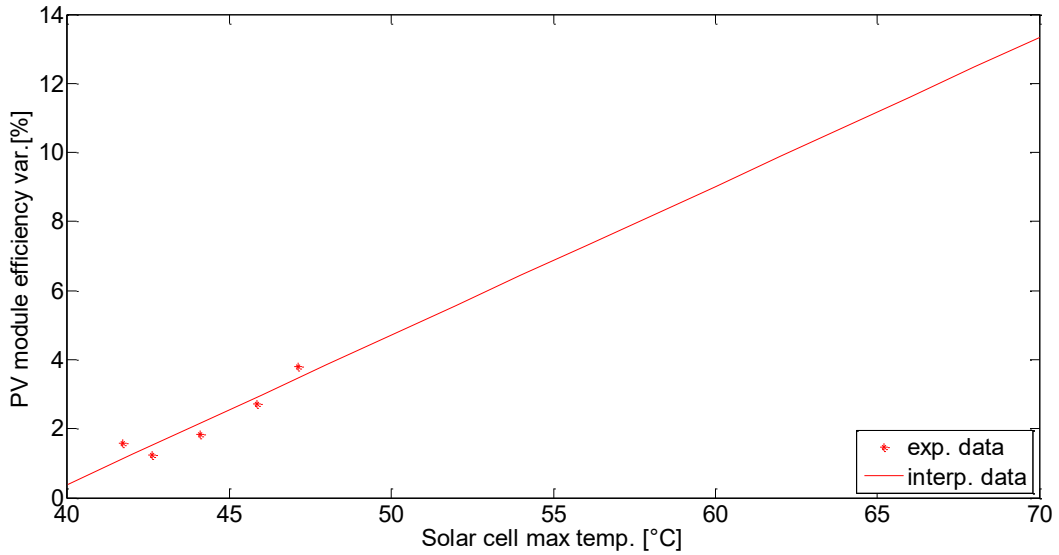

Fig. 4.1 – Percentage growth of power conversion efficiency, observable for a tandem a-Si / μc-Si PV module, as a function of the maximum operating temperature achieved by its solar cells. Note: experimental data (star marker), referred to a tested PV device (DUT0), as determined from the results shown in chapter 3, see Figs. 3.12, 3.14. Interpolated data (continuous line), obtained from the experimental ones.

Hence, we can conclude that, also if the Staebler-Wronski effect represents a limitation for the performance of the PV devices in question, it is also true the following important aspect. If these devices, while working in their MPP, achieve moderately high maximum temperatures (of the order of 45-50°C, in our experiments) even for short time intervals (of the order of one hour), some efficiency recovery (of the order of 2-3%, as observed in our experiments, or higher for higher cell maximum temperatures) will occur, as a result of the defect annealing.

This fact makes the thin film tandem amorphous / microcrystalline Si PV devices particularly suitable for the use in hot climate regions. There, significant benefits can be obtained in terms of electricity generation, by exploiting the specific thermal behavior of such devices.

To support such statement, the amount of power conversion efficiency improvement achievable in a hot climate region has been estimated, as shown below.

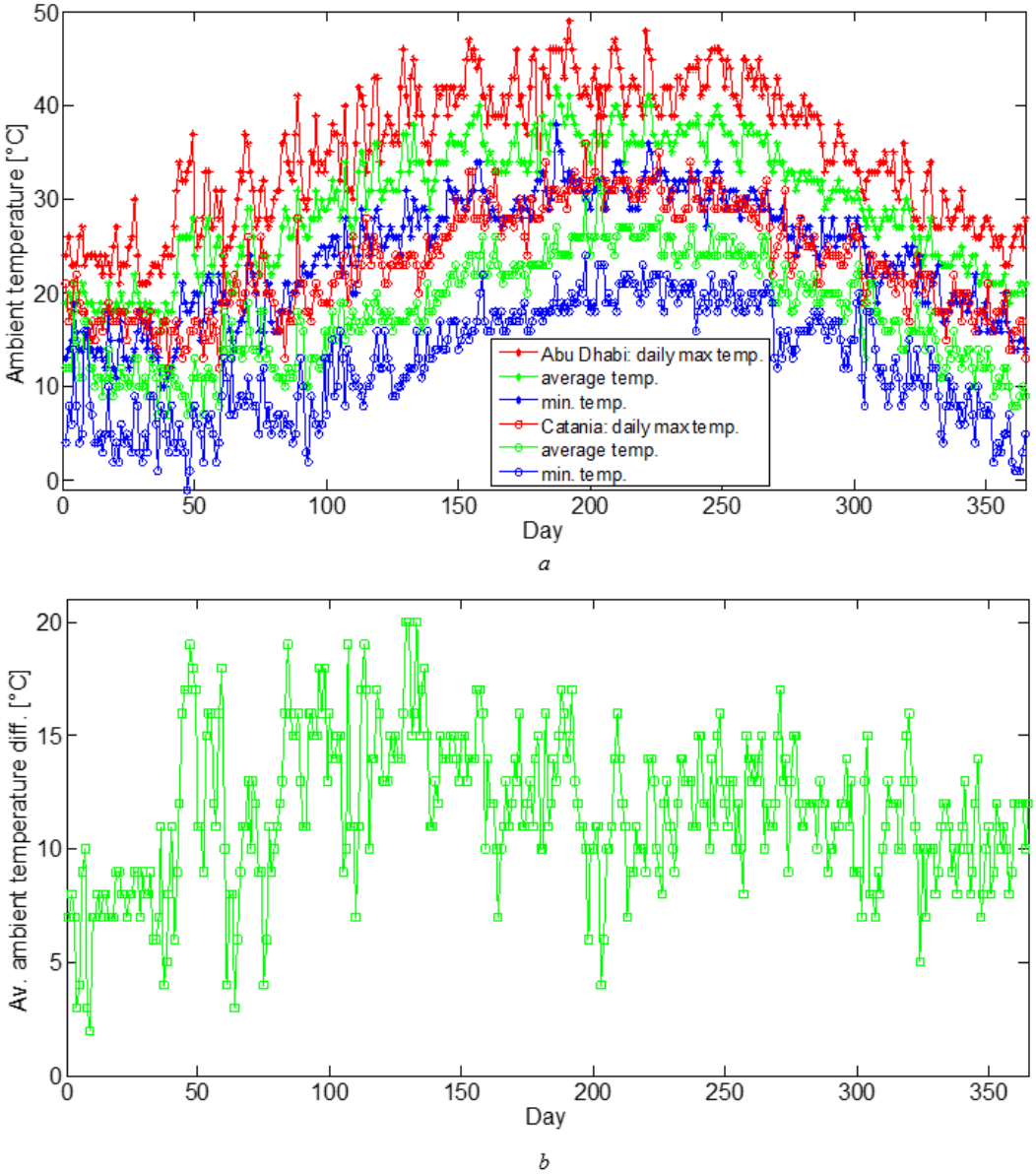

Fig. 4.2 – a. daily maximum, minimum and average ambient temperature trends for the year 2018, in Catania (Italy) and Abu Dhabi (United Arab Emirates) (Source: [74]*); b. difference between the daily average ambient temperature trends in a.*

We have considered (see Fig. 4.2 a) the daily maximum, minimum and average ambient temperature trends for the year 2018 (data available in public databases [74]), for two different geographical

locations: Catania (latitude: 37°26'32" N, longitude: 15°3'47" E, i.e. the location where the outdoor experiments described in chapter 3 were performed) and Abu Dhabi (United Arab Emirates, latitude: 24°27'17.2" N, longitude: 54°39'05.9"E).

As we note at a first glance from Fig. 4.2, the ambient temperature values in Abu Dhabi are significantly higher than those in Catania. If we consider for example the spring period, the daily average temperature in Abu Dhabi achieves values up to 20 °C higher than those in Catania (see Fig. 4.2 b).

We can assume that such ambient temperature difference determines an equal difference of the solar cell maximum operating temperature. Under this assumption, by considering the same PV device installed in Catania and in Abu Dhabi, based on the power conversion efficiency increases observed in Catania, we can extrapolate the power conversion efficiency increase observable during a day in Abu Dhabi, through the graph of Fig. 4.1. So, if in Catania the observed cell maximum operating temperature was of about 47 °C, in Abu Dhabi cell maximum operating temperatures near to 70 °C will be observable. To the latter temperature value corresponds a remarkable power conversion efficiency growth for a tandem PV module of the order of 13% (see Fig. 4.1), which is significantly higher than that observed in Catania (of the order of 3.8%, at the maximum cell temperature of 47 °C).

This fact shows clearly that in hot climate regions the electrical performance of tandem a-Si / μc-Si PV modules can be significantly better than those in cooler climate regions, by making their installation more convenient for electricity generation in hot climates.

CHAPTER 5 STATE OF THE ART ON MODELING OF BIFACIAL PV DEVICE PERFORMANCE AND BEHAVIOUR

This chapter concerns a state of the art on the modeling of performance of bifacial photovoltaic devices and their behavior. The first section (5.1) is focused on the main models so far proposed in the scientific literature. Firstly (see subsection 5.1.1), the relevance of accurately predicting the electrical performance of the mentioned devices and the fundamental structure of the mentioned models are highlighted. Then (see subsections 5.1.2, 5.1.3), an overview regarding the optical, thermal and electrical modeling of bifacial solar devices is provided, as proposed in different studies in the literature. Finally (subsection 5.1.4), the accuracy so far achieved by the main models in the literature is briefly discussed. The last section (5.2) summarizes the main findings in the literature concerning the behavior of bifacial PV devices, by varying the main parameters which affect their performance (see subsection 5.2.1) and recent initial attempts to deal with the performance optimization of the mentioned devices (see subsection 5.2.2).

5.1 Modeling of bifacial PV devices

5.1.1 General considerations

As mentioned in the introductory chapter 1, about the bifacial PV devices, two main questions are currently open, namely the lack of a standard methodology for the electrical characterization of such devices and an accurate knowledge of their performance in real operating conditions, through which one can individuate the optimal installation conditions, for maximizing the performance of these devices. From the necessity to tackle such relevant questions, the need to develop models to accurately predict the electrical performance of bifacial PV devices is born, for the dual purpose of analyzing the behavior of such devices and determining the installation conditions which allow to optimize their performance. Considering the increasing attention paid by the scientific community and the industrial context for such important matters, recently many authors (for instance, see [38],[49],[54], [75],[76],[77],[78],[79]) have made relevant efforts to propose and validate mathematical and physics-based models useful to forecast and optimize the performance of bifacial PV systems. Essentially, 3D (see as examples [76],[54],[38]) and 2D (for instance, see [80],[81]) models of bifacial PV devices currently exist. Albeit the first ones are typically more complex by adopting a three – dimensional approach, they can lead to more accurate results, since they generally allow to fully take into account the main aspects which influence the

performance of a bifacial PV system. Therefore, in the present chapter we will focus on the main 3D models so far proposed in the literature.

Essentially, the latter models have the fundamental structure schematized in Fig. 5.1. As we can see from such schematic representation, the mentioned models are typically complex, by including three key modeling parts, namely: the optical model, the thermal model and the electrical one.

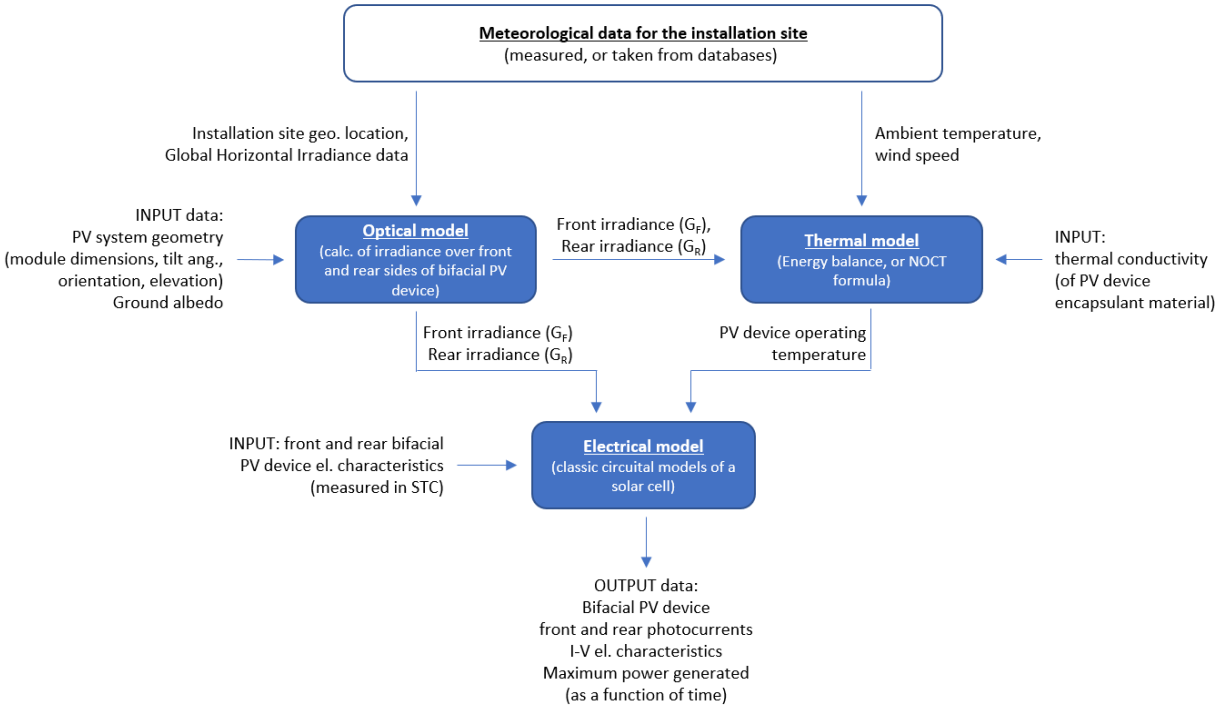

Fig. 5.1 – Schematic of the fundamental structure of the mathematical and physics-based models for predicting bifacial PV device performance.

Basically, the optical model allows to calculate (by implementing irradiance models proposed in the literature, see subsection 5.1.2 for further details), the irradiance over the bifacial device front and rear sides, by using the main input data specified in Fig. 5.1 (namely: the geographical coordinates of the installation site, the global horizontal irradiance data, measured or otherwise obtained for this site, the PV system geometry and the ground albedo). The thermal model allows to determine the bifacial PV device operating temperature and it requires, as main inputs, the time resolved meteorological data for the installation site (in general, the ambient temperature profile and the wind speed), the front and rear bifacial PV device irradiance data (as previous calculated by the optical model) and in some cases (when the thermal model consists of an energy balance) also the thermal conductivity of the encapsulant material used for the bifacial PV device. Finally, the output data provided by the optical and thermal models are used as inputs for the electrical model, which generally use the equations of the classic circuit

models of a solar cell [82] to determine the front and rear photocurrents and the electrical characteristics of the bifacial PV device, hence the maximum power generated, as a function of time.

In the next subsections 5.1.2 and 5.1.3, the main solutions proposed in the literature by different authors for the optical, thermal and electrical modeling will be described.

5.1.2 Optical modeling

For the optical modeling, basically several authors proposed to consider the direct, diffuse and reflected components of the solar radiation to estimate the total irradiance reaching the front and rear surfaces of a bifacial PV module, by using different irradiance models proposed in the literature.

The study [49] represents one of the earliest attempts made for accurately modeling the performance of a bifacial PV module, by considering a calculation method of the ground reflected radiation reaching the module rear surface. The optical model proposed in such study needed of irradiance data, acquired by available on-line databases (from GeoModel Solar Company – SolarGIS), which include global horizontal (GHI), diffuse horizontal (DHI) and beam normal irradiance (BNI) values, as well as data related to the sun position (with a time resolution of 15 min). Firstly, the direct irradiance at the tilted module front surface was determined by considering the sun position and BNI data. For the estimation of the diffuse irradiance and the albedo contribution for the PV module front surface, two well-known irradiance models proposed in the literature were used (namely, the Perez model [83], for calculating the diffuse irradiance and the model in [84], for determining the albedo contribution on a tilted surface, as a function of GHI, the albedo coefficient, α and the PV module surface tilt angle, β). Consequently, the overall irradiance reaching the module front surface was calculated by adding the aforementioned three components of the irradiance. Regarding the estimation of the overall irradiance reaching a bifacial PV module rear surface, basically it was calculated in the same way used for determining the overall irradiance at the front surface, except for the calculation of the ground-reflected irradiance (which is the primary source of irradiance for the rear surface). Actually, the latter calculation generally represents one of the most complex part of the bifacial PV device modeling and it is the one which need major accuracy, being of crucial importance for determining the performance of a bifacial PV device. The approach, which was proposed in [49] for this calculation, was based on the consideration of the so-called view factor (VF). Essentially, such a factor is a geometric entity which denotes the fraction of the radiation emitted from a generic surface (A_1), which is received by another surface (A_2). The VF can be expressed by the general equation below [76]:

$$VF_{A1\rightarrow A2} = \frac{1}{A_1}\int_{A2}\int_{A1}\frac{\cos\theta_1\cos\theta_2}{\pi S^2}dA_1\,dA_2 \tag{5.1}$$

where: A_1 and A_2 are two generic areas, divided into differential areas dA_1 and dA_2, respectively, S is the distance between the center of such areas; θ_1, θ_2 are angles which take into account the mutual

orientation of the mentioned areas (i.e. the angles formed between the normal vectors of these areas and the line joining them). As clearly explained in [76] (where the view factor approach previously proposed in [49], was further clarified), the reflected radiation achieving the rear side of a bifacial module can be estimated by considering that it comes from two different zones of the ground, i.e. the ground area (R_s) which is shaded (for the shading projected by the PV module) and the not shaded ground area (R_{ns}), as schematically depicted in fig. 5.2.

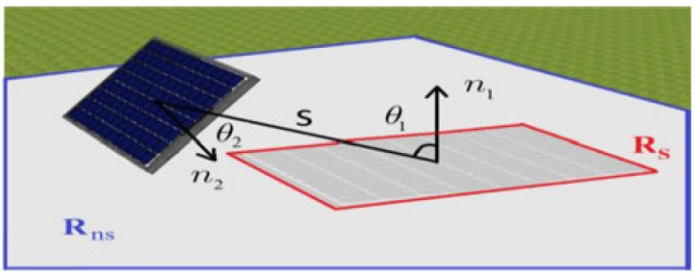

Fig. 5.2 – Schematic of the shaded (Rs) and not shaded (Rns) areas considered for determining the reflected radiation achieving the rear side of a bifacial PV module. The parameters shown are used to calculate the view factor (VF, as expressed by equation 5.1). Source: [76].

By using the equation 5.1, the view factors $VF_{Rs \rightarrow module\ area}$ and $VF_{Rns \rightarrow module\ area}$ can be determined, by considering the sun position and the parameters in Fig. 5.2. Once these factors are calculated, by assuming that the ground has an albedo coefficient α and a Lambertian character, the total reflected irradiance received by the module rear surface ($E_{Albedo,rear}$) can be determined through the equation:

$$E_{Albedo,rear} = \alpha \cdot GHI \cdot VF_{Rns \rightarrow module\ area} + \alpha \cdot DHI \cdot VF_{Rs \rightarrow module\ area} \quad (5.2)$$

where the symbols have the meaning previously specified.

It should be noted that in both studies [49] and [76], the angle-of-incidence dependent transmission of the irradiance from both module surfaces to the surface of the solar cells (hence, angle-of-incidence dependent reflection losses, related to the cell encapsulation within the PV module) was accounted too. However, the study [76] included an important upgrade of the model previously presented in [49], namely the consideration of the uneven distribution of the irradiance at the bifacial PV module rear side. In fact, in [76] the authors considered that each bifacial solar cell making up the module has a different distance from the areas R_{ns} and R_s, as well as different VFs corresponding to such areas, hence, each cell receives a different intensity of reflected irradiance. As underlined by these authors, since such an aspect affects considerably a bifacial PV module performance, it was considered for determining the spatial distribution of the irradiance at the PV module rear side.

Sometime after that the view factor approach was proposed for the irradiance calculation at the rear side of a bifacial PV device, other authors used the same approach, such as in [54], [78].

More recently, the authors in [38] proposed an optical modeling for some aspects different and more complex from the one so far described, although with a similar fundamental approach. In particular, in the latter work the proposed optical modeling comprised two main parts: the first one was the geographic and temporal irradiance model integrated with the NASA meteorological database, the second one was the geometric and analytical light-collection model which allowed to calculate the integrated light collection by a solar module arising from each irradiance component. Regarding the irradiance model, initially the position of the sun (namely, the sun path, solar zenith and azimuth angles) was calculated at any arbitrary time and geographical location, by using the NREL's solar position algorithm [85]. Then, the GHI intensity was estimated (on a minute-by-minute basis) through the Haurwitz clear-sky model proposed in the literature [86],[87], by using as input the predetermined solar path. Since such a model assumes an idealized atmospheric condition (existing only for certain locations and weather conditions), to fully account for geographic and climatic factors for a more accurate GHI evaluation, in [38] available on-line meteorological data, taken from the NASA Surface Meteorology and Solar Energy database, were used too. Once GHI was determined, its main components DHI and BHI were empirically estimated by using another well-known model proposed in the literature, i.e. the Orgill and Hollands model [88], which essentially is based on the consideration (as an input) of the so-called "sky clearness index" (defined as the ratio: $K_T = GHI/(I_0 \cdot cos\theta_z)$, being: *GHI* the global horizontal irradiance, I_0 the extraterrestrial irradiance on a horizontal surface, θ_z the solar zenith angle). Finally, the anisotropic character of the diffuse irradiance was also considered (by modeling the angular contributions of DHI), through the aforementioned Perez model. Regarding the analytical light-collection model, used in [38] for the evaluation of the irradiance achieving a bifacial PV module front and rear surfaces (arising from each irradiance component), essentially a similar (though more complex) approach to that previously described was used. Basically, this approach was focused on the consideration of the angle of incidence of the solar radiation over the PV module front and rear surfaces (calculated by taking into account the sun position and the PV module tilt and azimuth angles), view-factors, reflection losses (empirically estimated as proposed in [89]) and module self-shading effects.

5.1.3 Electrical and thermal modeling

As previously mentioned, a thermal model is needed essentially to determine the bifacial PV device operating temperature, which is then used as an input by the electrical model, in order to determine the electrical characteristics of the bifacial PV device. The main approaches proposed in the literature for such modeling are described below.

One of the most widespread approach for the thermal modeling (for instance used in [49], [54],[76]) is based on the use of the well-known NOCT formula [90], to determine the PV module operating

temperature (T_{module}), from the ambient temperature ($T_{ambient}$) profile at the module installation site and the timely resolved irradiance over the module plane (G):

$$T_{module} = T_{ambient} + \frac{NOCT - 20\,°C}{800\,W/m^2} G \tag{5.3}$$

To apply the eq. (5.3), the Nominal Operating Cell Temperature (NOCT)[12] for the bifacial PV device considered must be known. It is generally provided by manufacturers of PV modules[13].

An alternative approach to the use of the NOCT formula, for estimating the bifacial PV module operating temperature, was proposed in [77], where the consideration of a simple thermal balance was suggested: essentially, the power of the front and rear irradiance achieving the PV module, corrected for the reflection and the electric power delivered by the PV module, must be equal to the rate of heat conducted to the ambient (by considering that the PV module operating temperature is higher than the ambient temperature, as a result of the module irradiation). To implement such a thermal balance, an estimation of the module heat conductivity (which generally depends on the module installation conditions and on the thermal conductivity properties of the materials covering the PV module front and rear sides) was necessary, together with the knowledge of the wind speed values at the module installation site.

Other similar approaches proposed in the literature (such as in [91]), which allow to determine the module operating temperature as a function of the ambient temperature, the module irradiance and the wind speed through semi-empirical formulas, were used for instance in [38].

For the electrical modeling of a bifacial PV module, one of the most usual approach is that proposed in [76]. Basically, according to this approach, one of the classic circuit models of a solar cell (generally, the one or two-diode models [82]) is used to fit in the current - voltage (I-V) electrical characteristics, separately measured in Standard Test Conditions (STC) for the front and rear sides of a bifacial solar cell. The photocurrents generated by the front and rear sides of a bifacial solar cell are modeled as two current sources electrically in parallel to each other, hence they are added to each other to determine the overall photocurrent of the bifacial cell. The front and rear photocurrents are scaled individually based on the corresponding irradiance reaching the front and rear surfaces of the bifacial PV device.

In [54], the authors used an approach substantially similar to the aforementioned one. In particular, combining the simulated total front and rear side irradiances and the electrical parameters measured indoor at STC for separate front and rear side illumination, the short circuit currents and open circuit voltages for the front and rear sides of a bifacial PV module were determined separately, for given module operating conditions (by considering that in general the short circuit current of a solar device

[12] The NOCT is generally defined as the temperature of the PV module, under an irradiance of 800 W/m^2, at the ambient temperature of 20 °C, and wind speed of 1 m/s.
[13] For example, for commercial monocrystalline Silicon glass on glass bifacial PV modules, NOCT values typically range from 44 °C to 47 °C (as it can be seen from PV module datasheets, available on the web sites of different manufacturers).

depends linearly on the incident irradiation, while its open circuit voltage depends on the mentioned irradiation according to a logarithmic dependency). Consequently, such electrical parameters were used to determine the overall short circuit current (Isc) and the open circuit voltage (Voc) of the bifacial module, consistently with the method proposed in [52] (where the one-diode circuit model was considered for the assessment of the mentioned electrical parameters, from the front and rear parameters separately measured at STC for the front and back sides of a bifacial solar device). Finally, the maximum output power (P_{mpp}) of the bifacial PV module was evaluated by using the equation:

$$P_{mpp} = FF \cdot (\mathrm{Voc}\ \mathrm{Isc}) \cdot (1 + \alpha_{mpp} \cdot (T_{module} - 25°\mathrm{C})) \tag{5.4}$$

where: Voc and Isc represent the module open circuit voltage and short circuit current values calculated as above described, α_{mpp} is the temperature coefficient of the module P_{mpp}, T_{module} is the module operating temperature (estimated via the eq. (5.3)), FF is the module fill factor. As specified by the authors, for the FF in eq. (5.4) was used, as a simplification, the value of this parameter referred to the STC; this approximation determines a P_{mpp} underestimation for low levels of actual irradiance (lower than 1000 W/m^2, for which the STC are defined) and a P_{mpp} overestimation for high levels of actual irradiance (greater than 1000 W/m^2).

A slightly different method (for some aspects simpler than that above described), to estimate the total output power (P_{PV}) of a bifacial PV module, was suggested by the authors in [38], where the use of the following equation was proposed:

$$P_{PV} = I_{PV(Front)} \cdot \eta_{Front} + I_{PV(Rear)} \cdot \eta_{Rear} \tag{5.5}$$

being: $I_{PV(Front)}$ and $I_{PV(Rear)}$ the simulated illumination intensities (as determined through the optical modeling), respectively at the front and rear surfaces of the bifacial module, η_{Front} and η_{Rear} the power conversion efficiency values, respectively of the front and rear sides of the bifacial module. The latter values were determined, as a function of: the power conversion efficiency values for the front and rear sides of the considered PV module, measured in STC (denoted as $\eta_{Front(STC)}$ and $\eta_{Rear(STC)}$, respectively and taken from the datasheet of a commercial bifacial PV module), the efficiency temperature coefficient (as retrieved from the mentioned datasheet), the module operating temperature (calculated through the empirical approach proposed in [91]). It is important to note (as remarked by the authors of [38]) that the use of the eq. (5.5) for the estimation of P_{PV} implies that power losses due to the spatially nonuniform illumination of the PV module rear side[14] are neglected, despite they should be

[14] Such output power losses are ultimately due to an effect of electrical mismatch of the solar cells making up a bifacial PV module, which is induced by the unevenness distribution of the irradiance at the module rear side and which leads to different values of the photocurrents generated by the rear sides of these cells.

considered for a more accurate estimation of a bifacial PV module output power (as it was highlighted for instance in [76]).

To estimate the bifacial PV module total output power, the authors in [79] proposed a similar approach to that used in [38] (as above described) with the following main difference: in [79], some correction factors were considered for a combined adjustment to front irradiance from solar spectrum changes, reflections and soiling over the module surface and possible obstructions near the module rear surface. The latter obstructions, such as junction boxes, or module wiring, may partially shade the bifacial PV module rear side from the irradiance source, by ultimately leading to a reduction of the module electrical performance.

5.1.4 Modeling accuracy

In order to verify the accuracy of the bifacial PV device models proposed, some authors presented the main validation results of such models, by comparing simulated results with experimental ones.

For instance, in [54] the model proposed was validated, by comparing the results provided by the model for the exact configuration of a test PV system installed in the TUB (Technische Universität Berlin) campus in El Gouna, Egypt (latitude 27° N) and the experimental results obtained by measurements performed on the mentioned PV system during different months in 2014. The test PV system consisted of two adjacent PV modules, one bifacial and one mono-facial, mounted at a tilt of 20° and a height of 1.2 m, over a ground having a measured mean albedo equals to 0.3. The authors compared the values simulated by the model proposed with the experimental ones of the monthly bifacial gain (BG) (i.e. the gain in terms of electricity supplied, obtained by using a bifacial PV module, compared to a mono-facial one in the same installation conditions). The validation results which were obtained are reported in Fig. 5.3.

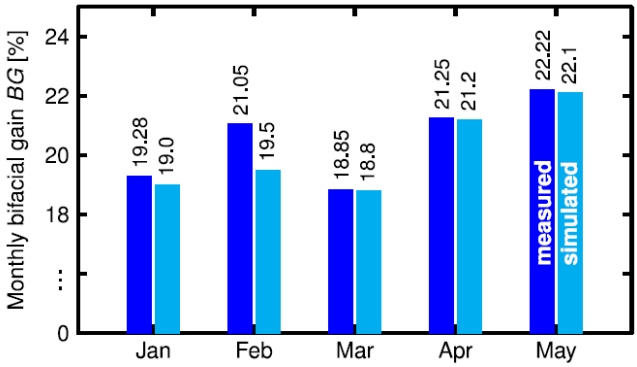

Fig. 5.3 – Validation results of the model proposed in [54].

From Fig. 5.3 appears evident that the simulated results are in general in good agreement with the experimental ones (with deviations within 1.5%), except for February 2014, where a larger deviation (model underestimation) was observed compared to the other months. As possible cause of this, the authors indicated that, in order to obtain the simulated results, they used for the year 2014 (when the above mentioned experiments were performed), diffuse irradiance factor (f_D) data referred to the year 2005 (being such data available only for the latter year), to estimate the diffuse hor. irradiance DHI needed for the simulation tool; although they checked that f_D is relatively constant over the years, they speculated that the actual value of f_D for February 2014 could be considerably different from the value used for the simulations, by leading to the aforementioned larger deviation.

In [79], the authors showed the accuracy of their model, by performing measurements on a bifacial PV module installed on an adjustable rack, in Albuquerque, NM, USA, for different days in the summer of 2016. They compared simulated and experimental data, both of maximum power generated by the bifacial module and of irradiance at the module rear surface. The main validation results of the model proposed, related to the module maximum output power (Pmp), are reported in Fig. 5.4.

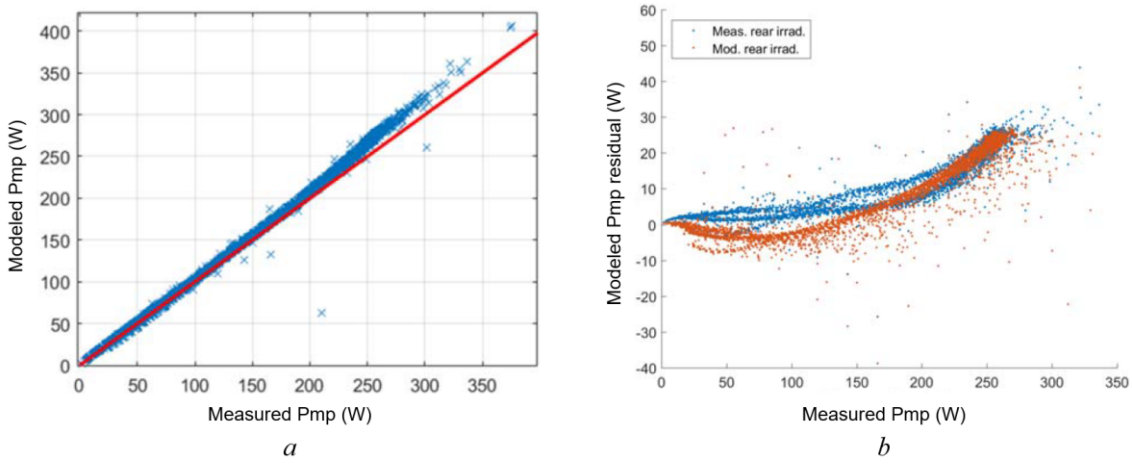

Fig. 5.4 – Main validation results of the proposed model, as obtained in [79]*: a. modeled and measured output maximum power (Pmp) values of a bifacial PV module (indicated by the blue markers.*

The red line represents the 1:1 ratio. The modeled values were obtained by using as input for the electro-thermal model proposed irradiance experimental values at the module front and rear surfaces, measured via ref. solar cells adequately positioned); b. residual of modeled Pmp, obtained using measured (blue markers) and modeled (orange markers) rear irradiance, vs. measured Pmp.

From Fig. 5.4 a appears evident that, by using, as input data for the electro-thermal model proposed, irradiance experimental values at the module front and rear surfaces, this model provides results in good agreement with the experimental ones, with a deviation of 2% approx., except for high Pmp values, when a significant higher deviation (model Pmp overestimation of about 7-8%) is observable. Moreover, the graph reported in Fig. 5.4 b. was used by the authors to validate their model also for the case (see orange markers) that modeled cell-by-cell irradiance values at the module rear surface were used as input for the electro-thermal part of the model to estimate Pmp. From the latter graph, we see clearly that, at full sun conditions, for both cases of utilization of measured and modeled irradiance values as input data for the mentioned model part, a model Pmp overestimation exists (equals to the highest percentage amount above specified). To explain the deviation higher values detected, the authors indicated two possible causes: 1. the electrical model proposed does not account for the module solar cell mismatch losses (which are most prominent during clear skies periods at midday, when irradiance is high and shadows on the ground are well-defined); 2. a non-linear dependence of the bifacial module maximum power on irradiance and/or temperature. In [79], the deviations obtained among simulated and experimental data of irradiance at the rear side of a bifacial PV module were also presented, by showing that the results predicted by the cell-by-cell rear irradiance model used generally followed the experimentally trends during the day, even if a maximum deviation of about 6% (model underestimation) was observable around midday.

In [38], the model proposed was validated by comparing the results provided by this model for different geographical locations and PV system installation conditions, with the ones provided by the model in [76] and with experimental results obtained in some others works in the literature. In particular, such a comparison was conducted by considering the absolute differences among the percentage values of bifacial gain (BG) obtainable through a stand-alone bifacial PV module as predicted by the model proposed and the ones presented in other scientific works. The authors of [38] remarked that, though their model assumed idealities such as infinite-size ground reflectors and obstruction-free shading (i.e. absence of shading from objects near the module, like a tree or a chimney), the model proposed provided results in good agreement with the ones presented in other works in the literature. For instance, by comparing their simulated results with the ones obtained in [76], they observed for the BG absolute differences within 6.4%. While comparing their simulated results with the experimental ones obtained in some other works in the literature, they detected absolute differences in terms of BG ranging from a minimum value of 0.3% to a maximum of 4.4%.

5.2 Bifacial PV devices performance prediction and optimization: main findings in the literature

Several authors focused on the analysis of the performance of bifacial PV devices, by using the results predicted by the models proposed to study the behavior of such devices and to find installation conditions which can optimize the mentioned performance. In the following subsections the most relevant findings of the studies of some of such authors will be illustrated.

5.2.1 Main parameters affecting the bifacial devices performances

As remarked in the literature, the main parameters able to sensibly affect a bifacial PV device performance are essentially: the elevation of the PV device from the ground, its orientation and tilt angle and the ground albedo.

In [76] an in-depth analysis of the effect produced on a stand-alone bifacial PV module performance by the variation of such parameters was carried out, on the basis of the simulation results provided by the model proposed (in which, as previously underlined in the paragraph 5.1.2, also the uneven distribution of the irradiance at the module rear surface was considered, as an important aspect for accurately predicting a bifacial PV module performance). In such work, the problem of the uneven spatial distribution of the irradiance achieving the bifacial module rear side was analyzed firstly, by showing that such a distribution varies when the module elevation from the ground changes. In particular, as clearly shown in Fig. 5.5, by considering two different elevation of the module from the ground (namely a height of the lowest side of the module from the ground equal to 1 m or 10 cm), a considerably larger rear irradiance nonuniformity was simulated for the lowest elevation considered (see Fig. 5.5 c., d. vs. a., b.). In fact, intuitively we can understand that when the distance of the module from the ground is increased, an effect of module self-shading reduction occurs, by leading to a more uniform distribution of the irradiance reaching the module rear side. Moreover, as it appears evident from the results reported in Fig. 5.5 e., a higher estimated average irradiance at the module rear side for the module located at the higher elevation was found. This can be explained considering that by increasing the module elevation, the area of the back diffuser seen by a PV module rear side increases too, by leading to an increase of the irradiance, reflected by the ground, which achieves the module rear surface. However, it is important to note (as it will be further explained and illustrated in the following chapter 6) that such a behavior is verifiable in the ideal case of a single bifacial PV module located over an ideally not confined back diffuser; instead, in the real case of a bifacial PV module within a PV field, where actually in general the back diffuser area is limited by the presence of other PV modules in proximity to the module considered, one should expect a different behavior. In fact, by increasing the

elevation over a confined back diffuser, the distance from the irradiance source growths too, by leading ultimately to a reduction of a bifacial module rear photocurrent.

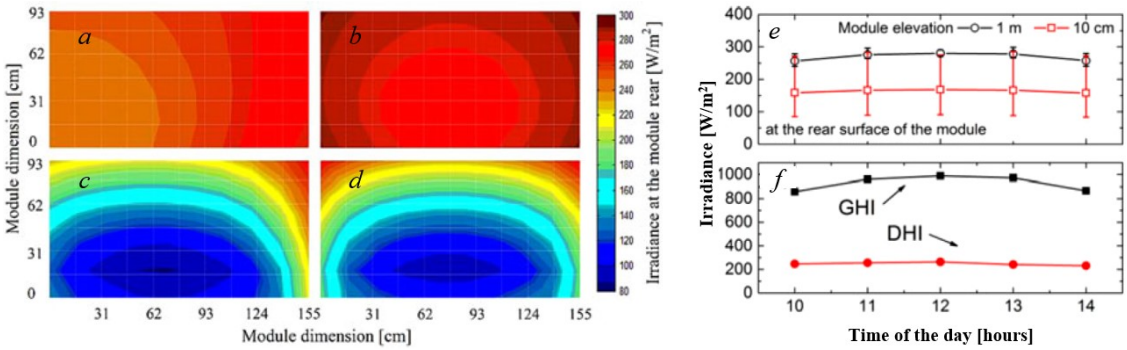

Fig. 5.5 – Simulated results obtained in [76] *for analyzing the distribution of the irradiance at the rear surface of a south-facing bifacial PV module: a., b. irradiance distrib. at the module elevation of 1 m from the ground, in the morning and at noon, respectively; c., d. irradiance distrib. at the module elevation of 10 cm from the ground, in the morning and at noon, respectively; e. trend of irradiance at the module rear surface, for the two elevations considered, during a summer day in Cairo, with the insolation profile in f. An albedo coefficient of 0.5 was considered.*

Consistent results with the ones obtained in [76] and shown in Fig. 5.5 were obtained with reference to a stand-alone bifacial PV module by the authors in [53], where a sensitivity analysis was performed (by means of an irradiance open-source software in the literature [92] and previously validated by the mentioned authors), to evaluate the effect of different parameters on the irradiance distribution and intensity at the rear side of a bifacial PV module. However, the most relevant aspect of the analysis in [53] is that the authors also focused on the case that a bifacial module is inserted in a PV field. For this specific case, the authors showed the results reported in Fig. 5.6. This figure clearly shows that the case of a bifacial module in a PV field is very different from the case of a stand-alone module, since the presence of neighboring modules (and consequent shadows projected on the ground) leads to a reduction of the rear irradiance and an increase of the rear irradiance spatial nonuniformity.

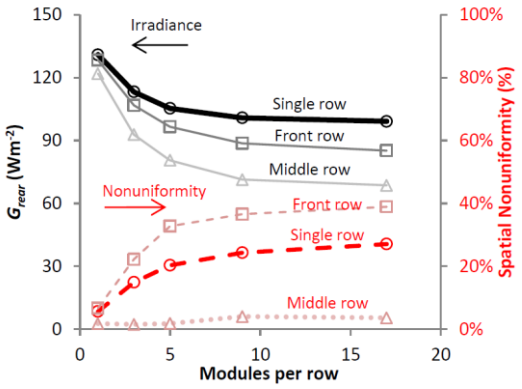

Fig. 5.6 – Rear irradiance intensity (G_{rear}) and its spatial nonuniformity (SN), for different multiple bifacial PV module configurations, as obtained through simulations in [53]. *Three PV field config. were*

considered: a single row of modules, two module rows, three sequential module rows. Simulations considered a variable n. of modules (37° tilted) per row (from 1 to 17). The G_{rear} and SN values were reported for the middle of each row. For the config. with two rows, the mentioned values were referred to the front row; for the config. with three rows, the mentioned values were referred to the middle row.

It is noteworthy that, for the case of a stand-alone bifacial PV module, the authors in [53] studied also the effect on the module rear irradiance (G_{rear}) due to variations of the ground albedo and of the module transparent area percentage (related to the possible presence of interstices among the module solar cells, which can involve a rear irradiance increase due to the light at the front side transmitted through the module, which is then reflected by the ground). Regarding the variation of the latter parameter, it was found that the module transparent area has an impact on G_{rear} (although sensibly more limited, compared to the one of the others parameters here mentioned) only for the case of module near to the ground, while it affects slightly the G_{rear} for module mounted sufficiently far from the ground (module elevation of about 1 m, or higher). Regarding the effect of the ground albedo, the simulations proved that a substantial linear relationship exists between the ground albedo and G_{rear} which increases sensibly, by increasing the ground reflectance (as shown in Fig. 5.7).

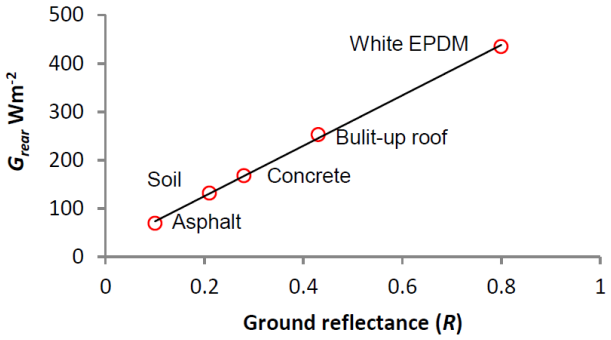

Fig. 5.7 - Effect of the ground reflectance (by considering different material types) on the G_{rear} value, for a single bifacial module at the elevation of 1 m from the ground, as simulated in [53].

Regarding the effects which the elevation from the ground of a bifacial PV device produces on its electrical performance, in [76] the authors highlighted that an optimum module elevation can be found to maximize the annual energy yield[15] of a bifacial module, depending on the geographical location, as for instance it is clearly shown in Fig. 5.8, for an optimally tilted south-facing stand-alone bifacial PV module, in Cairo, Egypt (latitude: 30.5 N, longitude: 31.23 E) and Oslo, Norway (latitude: 59.95 N, longitude: 10.76 E). Moreover, as we can see from this figure, as the modules are elevated higher, initially the annual energy yield increases (as a result of the suppression of the self-shading effect and better utilization of the reflective surface); however, as the module elevation exceeds a certain height

[15] Such a parameter was determined as the ratio between the yearly energy produced by the bifacial module and the power at STC under front illumination only.

(e.g., 1 m in Cairo), the View Factor (as defined in subsect. 5.1.2) from the reflective surface to the module begins to decrease significantly, leading to a lesser amount of the reflected radiation achieving the module rear surface, hence to a drop in annual energy yield.

Regarding the dependence of a bifacial PV module performance on the tilt angle, the results in [76] led to observe that, for each module elevation from the ground, a specific optimal tilt angle exists, which allows to maximize the annual energy yield of the module, as shown in Fig. 5.9.

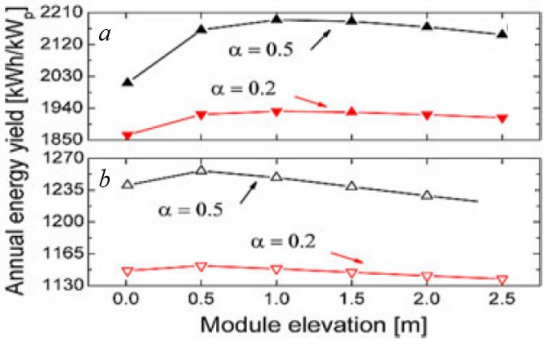

Fig. 5.8 - Annual energy yield of optimally tilted south-facing bifacial PV module, as a function of module elevation from the ground, as obtained through simulations in [76]*, for the locations of: a. Cairo, Egypt and b. Oslo, Norway. Two different albedo coefficients of the rear diffuser*[16] *were considered for the simulations (α = 0.5 and α = 0.2, by neglecting seasonal albedo variations).*

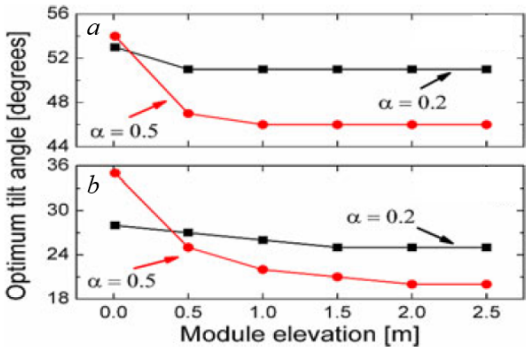

Fig. 5.9 – Trends of a bifacial PV module optimal tilt angle, as a function of the module elevation from the ground, for the two albedo coefficients indicated, as simulated in [76]*, by considering the locations of: a. Oslo, b. Cairo.*

Finally, regarding the influence of the ground albedo on a PV module electrical performance, in [76] it was demonstrated a linear relation between the bifacial gain (BG, see subsect. 5.1.4 for its definition) and the ground albedo coefficient (α): considerable BG growths were observed for increasing ground

[16] To obtain the results shown in this figure, for the rear diffuser (on the ground, under the PV module) was considered a rectangular reflective area considerably greater than the geometric module area (93x155 [cm x cm]). Such a rectangular area was defined by considering: a length L = 10 m for the rectangle base; for the other dimension of the rectangle, a length equals to L/2 behind the PV module (computed from the vertical projection of the center of the module on the ground), while in front of the PV module, the reflective area extends up to the line beyond which no more ground reflected radiation can achieve the module rear surface.

albedo values, consistently with the increases of irradiance at the rear module surface previously shown in Fig. 5.7. In [38], it was observed that the increase of the ground albedo from 0.25 to 0.5 can boost, for ground-mounted PV modules, the BG parameter from about 10% to about 20%, globally, by leading to the conclusion that, such an increase of BG encourages the development of cost-effective artificial ground reflectors to be overlapped to the natural groundcovers.

5.2.2 Performance optimization analysis attempts

In [38], the authors presented a simulation study, based on the results provided by their model, mainly aimed to propose a method for the performance optimization of a single bifacial PV module, on a global scale. It is important to remember that, as it was mentioned before, for such study the authors assumed, as a main ideality, the consideration of an infinite-size ground reflector.

Regarding the method suggested for the mentioned optimization, essentially a set of empirical equations was derived by the authors, based on the simulation results obtained. Such a method starts from the assumption that three fundamental design parameters have to be considered to optimize the electricity yield of a bifacial PV module, namely: its elevation from the ground (E), the module azimuth angle (γM), and the module tilt angle (β). Since such design parameters are in general mutually dependent to each other (in particular, optimal module azimuth and tilt angles are a function of elevation), the rational optimization approach proposed by the authors was to vary a single parameter at a time, while the remain parameters were keep constrained: 1. firstly, the E parameter was varied, to determine an optimum module elevation; 2. subsequently, γM was varied at fixed module tilt and elevation, to individuate its optimum; 3. finally, β was varied for fixed E and γM, to individuate its optimum. As conclusive step, on the basis of the simulation results, the aforementioned set of empirical equations was obtained, to analytically estimate the optimal value of each design parameter, for any arbitrary location in the world.

By analyzing performance variations of a bifacial module, when the module elevation E is changed, the authors in [38] highlighted that (see Fig. 5.10 a.): also if the yearly electricity production increases by increasing E (consistently with the findings of other works in the literature, as summarized in subsect. 5.2.1), a threshold elevation always exists (denoted as E_{95}), which represents the minimum elevation to achieve 95% of the maximum energy production without module self-shading. Such a threshold elevation depends on the installation site latitude and on the ground albedo, as shown from the simulation results reported in Fig. 5.10 b. As remarked by the mentioned authors, the knowledge of the E_{95} value is important for the installers, in order to minimize the installation costs (which obviously depend on the module elevation too[17]), while a convenient amount of electricity generation is ensured. Based on such findings, a first set of empirical equations was determined, useful to estimate the value

[17] the higher is the elevation of a PV system above the ground, the greater will be installation costs, essentially related to manpower and material requested.

of the E_{95} parameter, as a function of the latitude (of the geo. location considered), the ground albedo (α), and a PV module dimension (i.e. its height, H). It is noteworthy that however, such equations do not consider any additional cost due to the installation of the bifacial module at a certain elevation from the ground.

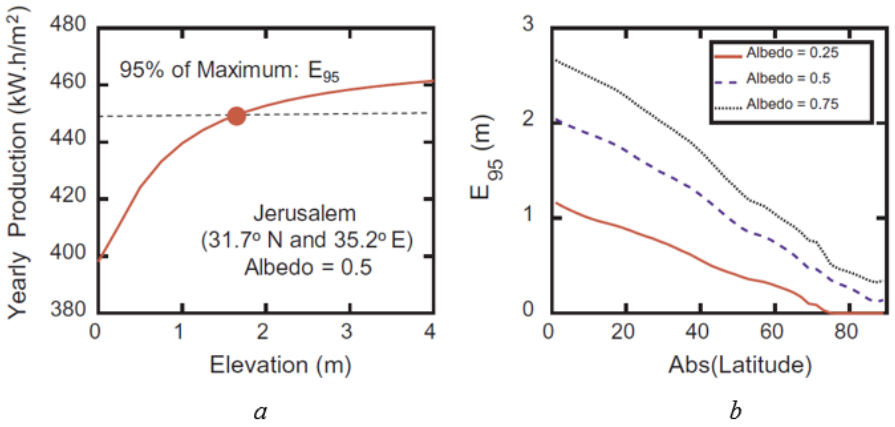

Fig. 5.10 – Simulation results obtained in [38]*, by analyzing the effect on bifacial PV module performance due to the variation of the module elevation above the ground: a. yearly electricity production of an optimally oriented and tilted bifacial module at Jerusalem, as a function of its elevation above the ground (with albedo 0.5): a threshold elevation (E_{95}) value is indicated (see main text for its definition); b. trend of E_{95}, as a function of the latitude (its absolute value is considered), for the different ground albedo values in the legend.*

Concerning the effect produced by the module azimuth angle on the performance of a bifacial PV module, the simulation results in [38] indicated that the optimal azimuth angle is given by two module alternative orientations, namely: the south-north orientation (denoted as Bi_{SN}), or the east-west (denoted as Bi_{EW}) vertical (i.e. with module tilt angle equal to 90°) orientation. While for the Arctic and Antarctic zones it was found that the performance of a bifacial PV module are substantially independent by the module azimuth angle, for the rest of the world the optimal module orientation (Bi_{SN} or Bi_{EW}, which leads to the module performance maximization) depends essentially on the latitude, module elevation and ground albedo. About the latitude, it was remarked that a critical latitude (denoted as Lat_{Cri}) exists, above which the Bi_{SN} orientation is more productive (i.e. it leads to optimize a bifacial module electricity generation) than the Bi_{EW} vertical one, while below which the contrary occurs. Such a critical latitude depends on the module elevation and ground albedo, as depicted in Fig. 5.11. Essentially, the graph in this figure is consistent with the findings summarized here below. When the module elevation equals to zero (i.e. when the module lowest side is in contact with the ground) and for high ground albedo values (typically, equal or higher to 0.5), the Bi_{EW} vertical orientation can lead to a greater electricity generation (up to 15%, globally) than the Bi_{SN} orientation, for locations with latitudes within 30° from the equator. This can be explained by considering that for high ground albedo values, the contribution of albedo light is comparable to diffuse and direct light and, while the electricity generation by a bifacial module

oriented in the south-north direction (Bi_{SN}) is more penalized by the module self-shading, the performance of a vertical mounted bifacial module oriented in the east-ovest direction (Bi_{EW}) is less influenced by the module self-shading, therefore the latter orientation results more favorable than the first one[18]. Instead, for geographical locations with higher latitudes (greater than 30°), for the Bi_{SN} orientation there will be a rapid growth of the module optimal tilt angle, by leading to a decrease of the module self-shading effects and, consequently, the Bi_{SN} orientation becomes the optimal one for these latitudes. Moreover, if the module elevation above the ground is increased to values higher than 1 m, also in this case, the module self-shading effects will be reduced and the optimal orientation will result the Bi_{SN} one, globally. Finally, at a module elevation equals to the above defined threshold elevation E_{95}, to which corresponds minimal self-shading, practically the optimal orientation will result always the Bi_{SN} one, globally. Based on these findings, a second set of empirical equation was obtained by the authors of [38], for determining the critical latitude as a function of the module elevation above the ground, E, the module height, H and the ground albedo, α. Therefore, once the optimal elevation is founded (by using the aforementioned first set of empirical equations), then, through the latter set of equations, the value of Lat_{Cri} and hence the module optimal azimuth angle can be found.

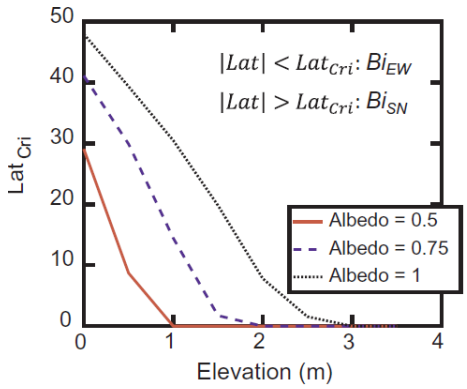

Fig. 5.11 – Critical latitude parameter (Lat_{Cri}) trends as a function of the module elevation, for different ground albedo values, as simulated in [38]. *The value of Lat_{Cri} allows to determine a bifacial PV module optimal azimuth angle (module with south – north, Bi_{SN}, or east-west, Bi_{EW} vertical orientations), based on the latitude ($|Lat|$) of the installation site (according to the relations specified in the legend).*

Finally, concerning the effect of the module tilt angle variation on a bifacial module electricity generation, the following aspects were pointed out. While for the east – west module orientation an optimal module tilt angle of 90° (vertical installed module) was found (as it has been remarked previously), for the south – north orientation, the simulation results reported in Fig. 5.12 were obtained.

[18] For the case of low ground albedo, it was found that conversely, the Bi_{SN} orientation is more favorable than the Bi_{EW} vertical orientation, since the direct light achieving the PV module is prevalent, compared to the contribution of the albedo light, and overall an optimal tilted PV module with Bi_{SN} orientation is able to collect more direct light than that collected by a vertical installed PV module with Bi_{EW} orientation.

From this figure, appears evident that, as expected, the optimal tilt angle for a bifacial module oriented in the south – north direction (i.e. the tilt angle value which maximize its electricity output) increases by increasing the latitude of the module installation site, similarly to what occurs for a traditional mono-facial PV module, although for a bifacial PV module the optimal tilt angle results always slightly greater than the one of a mono-facial module. Essentially, such a greater optimal tilt angle for a bifacial module allows to improve the albedo radiation collection from the module rear side. As we see from Fig. 5.12, the optimal tilt angle for a bifacial module depends also on the ground albedo and the module elevation above the ground. Based on the above mentioned dependences, a third and last set of empirical equations was determined in [38], to estimate the optimal tilt angle for a stand-alone bifacial PV module (as a function of the aforementioned parameters E, H, α, by taking into account the module self-shading effect), once its optimal elevation from the ground and orientation were found.

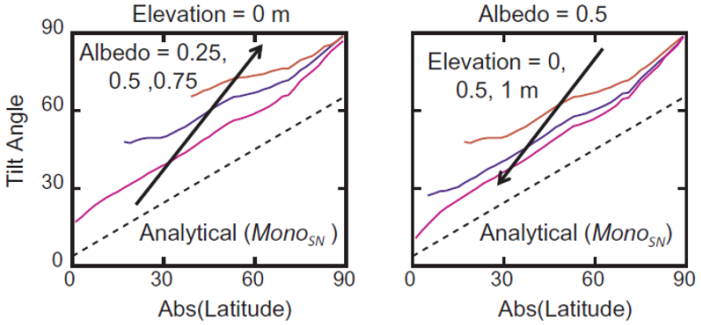

Fig. 5.12 – Optimal tilt angle trends for a bifacial PV module oriented in south-north direction (at latitudes greater than the critical latitude, Lat_{Cri} in Fig. 5.11), as a function of the installation site latitude: a. at the module elevation of 0 m (ground-installed PV module), for increasing values of ground albedo (as indicated in the legend, according to the arrow direction); b. for the fixed ground albedo of 0.5, for increasing values of module elevation above the ground (as indicated in the legend, according to the arrow direction). The discontinuous straight line indicates the optimal tilt angle trend, as calculated for a mono-facial PV module. Source: [38].

At last but not least, it is worth recalling that all the mentioned empirical roles were obtained by the authors of [38] with reference to the ideal case of a stand-alone bifacial module, under the idealities that an infinite-size ground reflector was present beyond the module and shadings due to nearby objects were not present. As underlined by the same authors, in the case that a bifacial PV module is inserted within a PV field, the shading due to neighboring modules (in addition to the self-shading of a single module) will reduce the overall performances, hence affecting their optimization. For example, in this concern, a higher value of the threshold elevation (E_{95}) was expected, in order to mitigate the effect of mutual shading of module rows.

CHAPTER 6 DEVELOPMENT AND EXPERIMENTAL VALIDATION OF A NOVEL MODEL TO PREDICT BIFACIAL PV MODULES PERFORMANCE: MAJOR VALIDATION AND SIMULATION RESULTS

This chapter is focused on the activities of development and experimental validation of a novel model for predicting the performance of bifacial photovoltaic modules. Firstly, in the section 6.1, the model proposed will be described. Afterwards, in the section 6.2, the experimental activities carried out for the validation of such model will be described. In particular, after a description of the devices and experimental method used for the mentioned validation activities (see subsect. 6.2.1), the main validation results obtained will be illustrated and discussed (see subsect. 6.2.2), by highlighting the very good agreement observed among the simulated results and the experimental ones. Contextually, we will show the behavior peculiarities of a bifacial PV module when the main parameters affecting its electrical performance (namely, the module elevation from the ground, the module tilt angle, and the ground reflectivity) are changed. A comparison among the results provided by the model proposed and the experimental ones, in terms of both global horizontal irradiance and module operating temperature, will be presented too. Finally, in section 6.3 the main conclusions of this chapter will be summarized.

6.1 Description of the model proposed

The analytical model which we propose is suitable for any geographical location. It has been implemented in Matlab environment [93]. The beam, diffuse and reflected components of the solar radiation has been considered, as it was described in detail in [94]. The well-known parametric ASHRAE model[19] (which was presented in [95]) is integrated in the model here proposed for estimating the horizontal irradiance (I_H). Moreover, the extraterrestrial radiation (expressed as a function of geographical coordinates and solar time) is determined according to [96]. Through the general equation below reported, the global irradiance on an inclined surface (I_β) has been estimated, by taking into account in this way the effect on the irradiance due to the module tilt angle (β) [94]:

$$I_\beta = I_{b,\beta} + I_{d,\beta} + I_r \tag{6.1}$$

[19] This is a simple model, whose use is widespread in the engineering and architectural communities. It allows the estimation of the global irradiance on a horizontal surface, by determining its components (namely, the beam normal irradiance on a horizontal surface and the diffuse one), based on three constants having different estimated values for different months of the year.

being $I_{b,\beta}$, $I_{d,\beta}$ and I_r the direct, diffuse and reflected components of the aforementioned I_β, respectively.

We consider that the diffuse component of the solar radiation, evaluated by means of the isotropic Liu and Jordan's model [97], strikes the surface of the PV device.

Fig. 6.1 shows the trends of the different components of the solar radiation, integrated for the duration of a solar year, over a tilted surface oriented toward south, as predicted by the model used for the latitude of Catania, Italy (37° 26' 32'' N). In such figure, the solar radiation on a horizontal surface (see the red curve) and the global radiation on a tilted surface (see the green curve), as calculated by the mentioned model, are reported too.

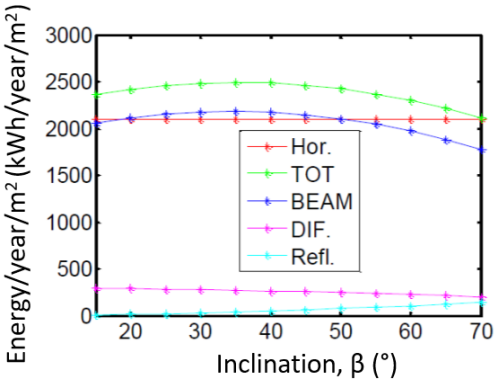

Fig. 6.1 - Trends of the different components (beam, diffuse and reflected) of the solar radiation, integrated for the duration of a solar year, over an inclined surface (of an angle β, respect to the horizontal plane) oriented toward south, as predicted by the model used for the latitude of Catania, Italy. The green curve represents the total solar radiation over the mentioned surface (as calculated by adding the aforementioned components). The red curve represents the solar radiation over a horizontal surface.

To estimate the solar radiation achieving the rear side of a bifacial PV device, basically, the solid angle of incidence of the radiation is taken into account as illustrated in Fig. 6.2, according to a method similar to that presented in [76],[54] and herein described in detail in the previous chapter 5 (see subsect. 5.1.2). In particular, we consider that each point of the not shaded soil is illuminated by the radiation of intensity I_H. The soil element of area dA_s acts as a light source which isotropically diffuses on 2 π sr a radiation equal to $(dA_s \cdot I_H \cdot \alpha)$, being α the ground albedo. Therefore, if the element of module rear surface dA_m sees dA_s under the solid angle $d\Omega$, the corresponding optical power will be $(dA_s \cdot I_H \cdot \alpha) \cdot (d\Omega/2\pi)$. Consequently, by computing the integral over the soil whole area (As), the incident radiation over the bifacial PV device rear surface (I_{rear}) is obtained.

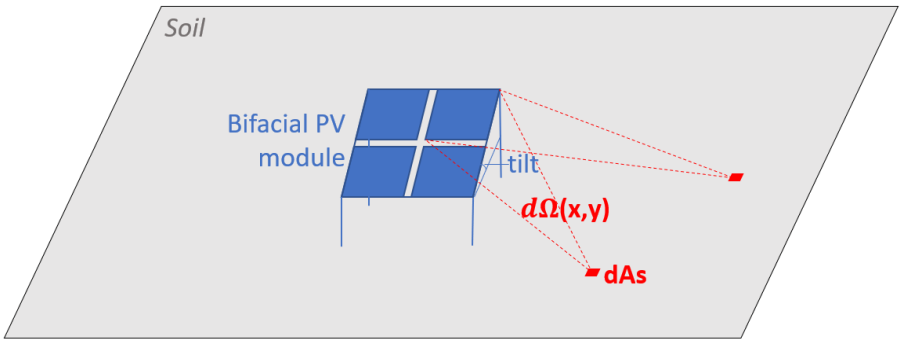

Fig. 6.2 - Schematic drawing of solid angles considered for the estimation of the solar radiation achieving the rear side of a bifacial PV device: a soil differential element (of area dA_s), at the generic location (x,y), sees a solar cell under the solid view angle $d\Omega(x,y)$.

By multiplying by the External Quantum Efficiency measured for the cell front and rear sides (EQE_{front} and EQE_{rear}, respectively), the short circuit currents of both sides ($I_{SC,front}$ and $I_{SC,rear}$, respectively) of each solar cell is obtained, through the equations here below:

$$I_{SC,front} = A \cdot \cos\gamma \cdot \int_{\lambda_{Gap}}^{0} EQE_{front}(\lambda) \cdot I_{\beta} \cdot d\lambda \tag{6.2}$$

$$I_{SC,rear} = \int_{A_s} (d\Omega(x,y) \,/\, 2\pi) \cdot shadow(x,y) \cdot dA_s \cdot \int_{\lambda_{Gap}}^{0} \alpha(\lambda) \cdot EQE_{back}(\lambda) \cdot I_H \cdot d\lambda \tag{6.3}$$

being: A the cell area, γ the incidence angle of the radiation, λ_{Gap} the cell semiconductor material bandgap wavelength, I_{β} and I_H the incident solar spectrum (for a given air mass) over a bifacial module front surface (as evaluated through the equation (6.1)) and over a horizontal surface, respectively, *As* the soil total area below the cell (divided into differential elements of area dA_s), $d\Omega(x,y)$ the solid angle (depending on the coordinates x, y of the soil point considered, see Fig. 6.2) under which the considered solar cell sees the soil element of area dA_s at the position (x,y), $shadow(x,y)$ a function (of the considered soil point) which represents the shadow projected by the cell (equal to 0, if the soil area is shadowed, 1 otherwise), $\alpha(\lambda)$ the ground albedo. According to the equations (6.2) and (6.3), the mentioned calculation is carried out as a function of the wavelength (λ), to take into account the dependence on λ of the soil reflectivity and of the solar cell quantum efficiency. The normal incidence reflectivity was measured in the 300-1100 nm wavelength range, for the materials over which the bifacial solar devices were located, to obtain the ground albedo.

The overall photocurrent of each PV cell is determined by adding the currents calculated through the equations (6.2) and (6.3). The electrical characteristics of each cell are calculated according to the classic single-diode circuit model [82]. Consequently, the bifacial solar module current vs. voltage characteristics (for different hours of a given day) are determined by the characteristics of its cells electrically in series. The module temperature is evaluated by means of the well-known NOCT formula

(see equation (5.3) reported herein, chapter 5), as a function of the ambient temperature and then compared to experimental data.

It is important to remark that the use of eq. (6.3) for evaluating the photocurrent of each solar cell rear side implies the full consideration of the effect of irradiance uneven distribution at the bifacial PV module rear side on its electrical characteristics. In fact, the solar cells of the module will have in general different values of $I_{SC,rear}$ and the overall module rear photocurrent will be practically equal to the minimum value among the photocurrents generated by the rear sides of its cells electrically in series. As an example, Fig. 6.3 shows the electrical characteristics of the four solar cells in series of a bifacial PV module (near optimally tilted at the latitude of Catania, Italy) and the resulting electrical characteristics of such module, as calculated by the model here presented, at midday of the day 281 of the year 2018.

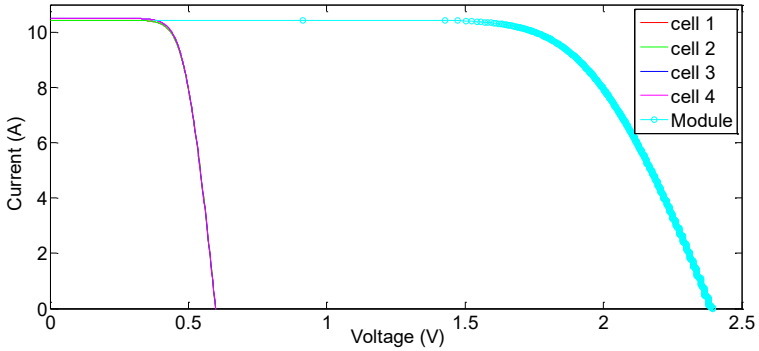

Fig. 6.3 – Electrical characteristics of the solar cells making up a bifacial PV module (near optimally tilted at the latitude of Catania) and resulting electrical characteristics of such module, as calculated by the model here proposed, at midday of the day n. 281 of 2018.

Moreover, it is noteworthy that in the model here proposed, for the evaluation of the useful (i.e. exploitable to be converted into electricity) solar radiation collected by a bifacial PV module, we also consider the following. A fraction of the available radiation achieving the module surface does not penetrate inside the solar cells, since it is reflected by such surface, in dependence of the material type used to incapsulate the module solar cells. As it is well-known, when the incident light on a surface is very grazing, the reflectivity tends to 100%. In particular, for the specific case of an interface air – glass, from the Fresnel equations [98] can be derived that the reflectivity is 50% approximately for an incidence angle of radiation equal to 80°. Therefore, with reference to glass – glass bifacial PV modules, we have considered that for incidence angles equal or higher than $\theta_{crit.}$ = 80°, the incident radiation is reflected by the module surfaces, hence not collected by the solar cells. To understand the influence of considering the critical incidence angle $\theta_{crit.}$ on the estimation of the useful solar radiation collected by a bifacial module rear side, we can consider the schematic representation in Fig. 6.4. From such schematic drawing, we clearly note as follows. Considering the soil area in front of the PV module, the soil area seen by the module rear surface, which actually contributes to the useful solar radiation

collected by such surface, is practically limited by $\theta_{crit.}$; instead, considering the soil area behind the module, in the ideal case of an unconfined back diffuser, the soil area seen by the module rear surface, contributing to the useful radiation collected by the module rear surface, is theoretically not limited by the existence of $\theta_{crit.}$ Obviously, it is so only for the mentioned ideal case of an unconfined back diffuser over which is located a single PV module; in fact, in the real case of a bifacial module within a PV field, the soil area seen by the module rear side is in general limited by the presence of other neighbors modules, as it has been mentioned in the previous chapter and it will be further explained in the following, within the present chapter.

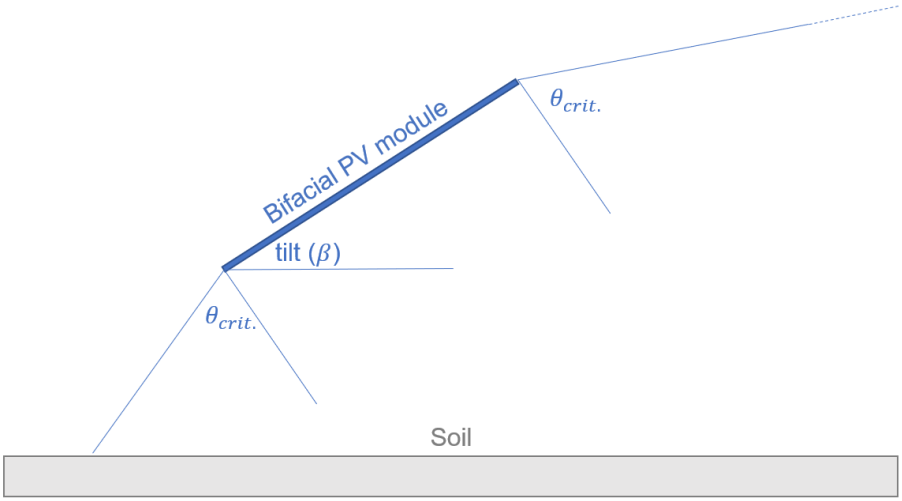

Fig. 6.4 – Schematic representation of the critical incidence angle ($\theta_{crit.}$) which has to be considered to accurately estimate the useful solar radiation collected by the rear surface of a bifacial PV module.

The model proposed and above described has been subsequently upgraded to allow the electrical performance prediction for strings of PV modules, both in presence of solar tracker and without solar tracker, as it will be further discussed in the next chapter 7.

6.2 Experimental validation of the model

6.2.1 Devices and experimental method

To validate the model proposed, a significant number of outdoor tests were performed on a glass-glass bifacial solar module, oriented toward south. The tested PV module is composed by four PERT[20] monocrystalline silicon bifacial PV cells, electrically in series.

A schematic representation of such solar cells (substantially similar to that illustrated and described herein, see section 1.4, Fig. 1.6 a.) was shown in [99]. Each of the mentioned cells has the main features summarized in Tab. 6.1. A picture of both sides of a sample of such cells is shown in Fig. 6.5.

Geometric area [cm^2]	235.75
Thickness [μm]	~200
Front side	SiNx anti-reflection coatings, n. 4 silver busbars, n. 100 fingers
Rear side	silver/aluminum soldering pads, n. 110 fingers

Tab. 6.1 – Main features of each of the four PERT monocrystalline silicon bifacial solar cells making up the tested PV module.

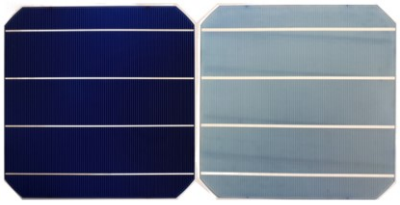

a *b*

Fig. 6.5 – Picture of the a. front and b. rear sides of a sample of the solar cells making up the tested PV module.

Fig. 6.6 shows the electrical characteristics of a sample of the solar cells making up the tested PV module, as measured at the solar simulator[21] by illuminating separately its front and rear sides at 1 SUN with AM1.5G spectrum and by keeping its temperature at 25°C. Moreover, Fig. 6.7 shows the measured External Quantum Efficiency curves of the front and rear sides of the same sample.

The power conversion efficiency of the front side of the solar cells in question is equal to 16.3%, their bifaciality factor is 77% (calculated as the ratio $(I_{sc,front}/I_{sc,rear}) \cdot 100$) and the power temperature coefficient is equal to – 0.44%/°C.

[20] PERT is the acronym of passivated emitter, rear totally diffused.
[21] (by using the tools for indoor measurements presented herein, see section 3.2.1).

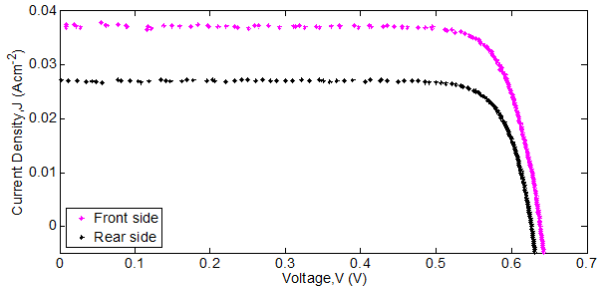

Fig. 6.6 - Electrical characteristics (short circuit current density, J vs. voltage, V curves) of front and rear sides of a sample of the solar cells making up the tested PV module, detected by illuminating separately the front and rear sides of the sample at the solar simulator, at 1 SUN with AM1.5G spectrum and by keeping its temperature at 25°C.

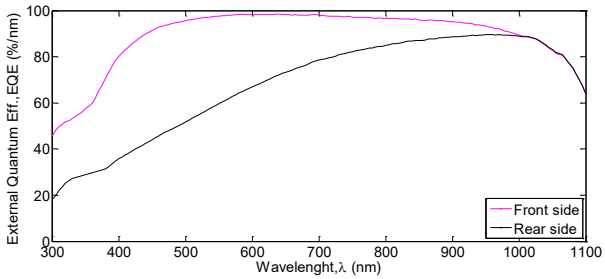

Fig. 6.7 – External Quantum Efficiency measured trends of front and rear sides of a sample (the same whose electrical characteristics are reported in Fig. 6.6) of the solar cells making up the tested PV module.

Concerning the experimental method applied for all the outdoor validation tests on the aforementioned bifacial PV module, such tests were carried out in Catania, Italy (latitude: 37°26'32" N, longitude: 15°3'47" E), in clear sky condition (over the course of the year 2018), by changing one by one the most important parameters having an effect on the electrical performance of a bifacial device, namely: the module elevation from the soil; the module tilt angle; reflectivity of the soil over which the module was located. In more detail, the module tested was located over either a wide asphalt area (as depicted in Fig. 6.8 a.), or a white square back diffuser (consisting of plastic material, with area of 1 m^2) surrounded by asphalt, by changing the module location (as it is illustrated in Fig. 6.8 b.).

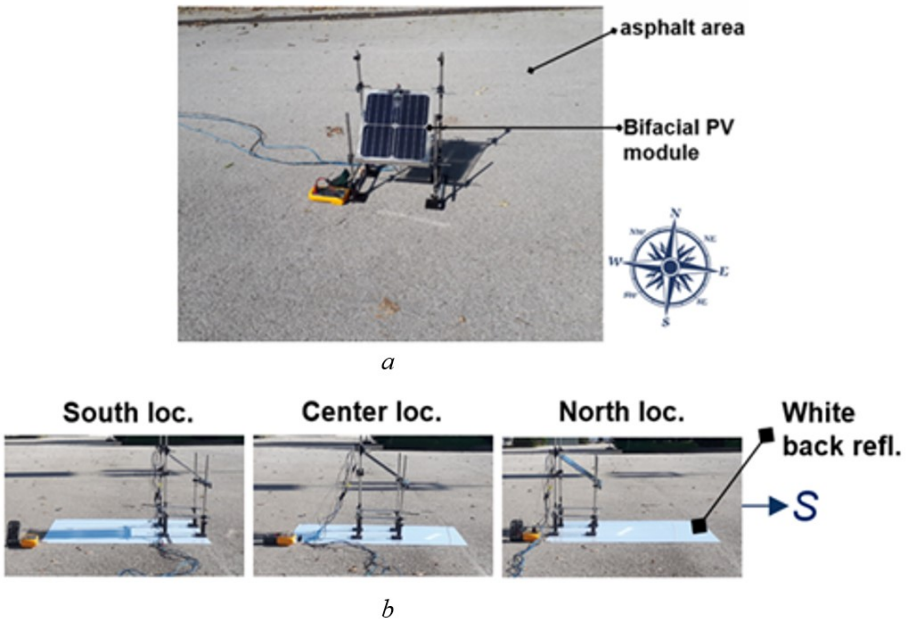

Fig. 6.8 - Pictures of the experimental set up used for the outdoor validation tests: a. with a large asphalt area as back diffuser; b. with a white square back diffuser (1 m^2) surrounded by asphalt, by varying the module location respect to such back diffuser.

Fig. 6.9 shows the normal incidence reflectivity curves of some samples of the aforementioned materials (i.e. the asphalt and the white plastic material, used as back diffusers, for the outdoor experimental tests in question), as measured in the 300-1100 nm wavelength range[22].

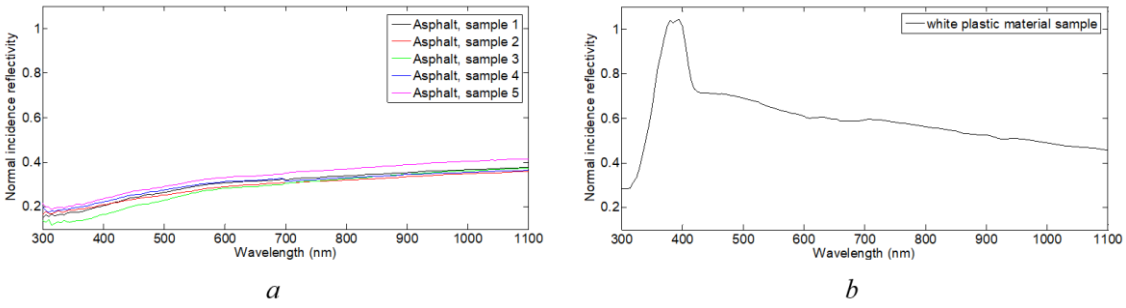

Fig. 6.9 - Normal incidence reflectivity measured for some samples of asphalt and of a white plastic material. Both such materials were used as back diffusers for the outdoor experimental tests performed for the validation of the model proposed. The normal incidence reflectivity values here shown were used as inputs for the mentioned model.

In each outdoor test, several measurements of the current (I) vs. voltage (V) module characteristics were carried out, at different times (hence, for different solar irradiance conditions). During each test, the horizontal solar irradiance was monitored by using a reference c-Si PV cell (whose characteristics

[22] To perform such measurements, a standard equipment (essentially, a Bentham TMc300 monochromator), available at CNR-IMM labs., was used.

have been specified herein, see Tab. 3.2, chapter 3), suitably connected to an electrometer, while the tested PV module front and rear side temperature values were measured through two thermocouples, adequately in contact with the module glass external surfaces, connected to two digital multimeters.

The temperature experimental values of the module external surfaces (as measured via the aforementioned thermocouples) were used to estimate the module operating temperature (by considering the glass thermal conductivity and the incident solar power density on the mentioned module), to be compared to that predicted by the proposed model based on the NOCT formula.

Fig. 6.10 shows a schematic of the experimental set up used for such measurements.
Essentially, according to the schematic in Fig. 6.10, the tested bifacial PV module electrical characteristics were measured by adopting a suitable 4-wires detection (voltamperometric) system which included a digital multimeter (Keithley 196) and a Source Meter (Keithley 2651A). Moreover, the measured characteristics were acquired (via a data acquisition board) and saved on a PC (where the LabVIEW 8.2 software was preinstalled).

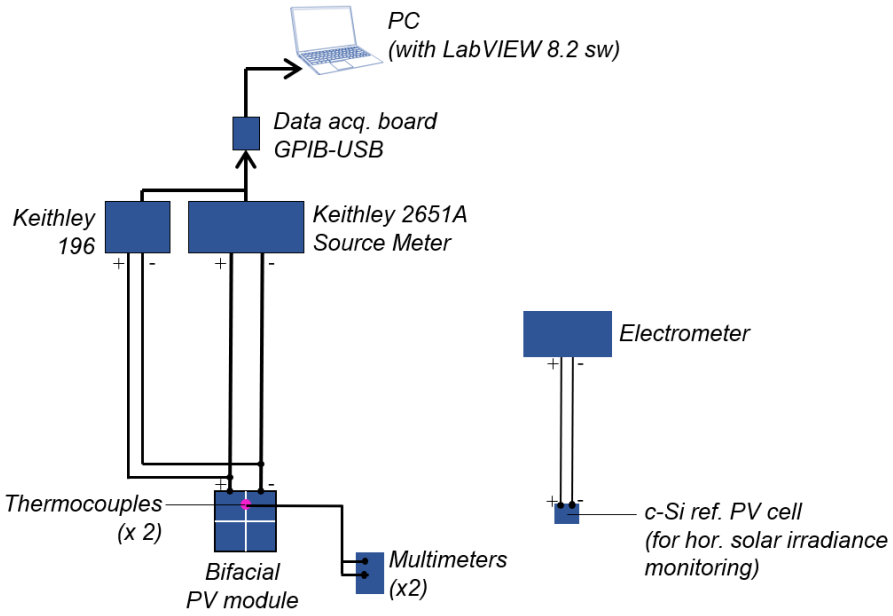

Fig. 6.10- Schematic of the experimental set up used for the outdoor validation tests.

6.2.2 Main validation results

This section is dedicated to the main validation results of the model presented in the previous section, by comparing the experimental results with the simulated ones and commenting in detail the accuracy of the model. Firstly (see subsect. 6.2.2.1), a focus on the accuracy of the global horizontal irradiance (I_H) values, as predicted for different latitudes by the ASHRAE model (which, as mentioned previously, is integrated in the model for bifacial device performance prediction here proposed), is presented, as an aspect able to affects the model overall accuracy. Subsequently (see subsect. 6.2.2.2), the validation results related to the module operating temperature are presented, as a crucial aspect which influences the estimation of a bifacial PV module output power. Finally, the following subsections (from 6.2.2.3 to 6.2.2.5), are focused on the validation results by varying the module elevation from the ground, the module tilt angle and the ground albedo, by illustrating the very low deviations observed among the experimental results and the simulated ones and remarking the peculiarities of a bifacial module electrical behavior when the aforementioned parameters are changed.

6.2.2.1 Global horizontal irradiance prediction accuracy

The accuracy of the global horizontal irradiance (I_H) yearly values predicted by the aforementioned ASHRAE model has been checked by comparing, with reference to different geographical locations (chosen by the northern hemisphere, from near to the equator to near to the Arctic Circle), such values with the ones retrieved by a well-known irradiance database, namely the available online GLOBAL SOLAR ATLAS database [100]. Tab. 6.2 summarizes the results of this comparison.

Location	**latitude**	**longitude**	**I_H** (calc. through ASHRAE model) [kWh/m^2/year]	**I_H** (retrieved by [100]) [kWh/m^2/year]
Abu Dhabi, United Arab Emirates	24° 27' 17.2" N	54° 39' 5.9" E	2427	2172
Be'er Sheva, Israel	31° 15' 8.3" N	34° 47' 32.1" E	2268	2083
Catania, Italy	37° 26' 32" N	15° 3' 47" E	2097	1760
Freiburg im Breisgau, Germany	48° 00' 33.7" N	7° 50' 4.6" E	1761	1197
Aarhus, Denmark	56° 18' 26.9" N	10° 37' 40.7" E	1479	1018

Tab. 6.2 – Comparison among global horizontal irradiance (I_H) values per year calculated by the ASHRAE model used in this work and the ones retrieved by the GLOBAL SOLAR ATLAS database [100]*, at the different geographical locations specified.*

As we can clearly see from the I_H values reported in Tab. 6.2, actually the ASHRAE model in general produces an overestimation of I_H. This overestimation results overall relatively small (order of 10%) for low latitudes (see locations near to the equator), instead it results quite heavy for high latitudes (see locations very far from the equator). This is probably due to the fact that for the latter latitudes, the ASHRAE model is not able to provide an accurate prediction of I_H, since evidently at high latitudes the effects on I_H values induced by the environmental conditions (such as cloud cover, perceptible water content, and atmospheric turbidity), of which fundamentally the ASHRAE parametric model does not account for, are not negligible. Actually, ss it was underlined in [94], the so-called parametric models for the irradiance estimation, to which the ASHRAE model [95] used in the present work belongs, should be integrated with specific information about the aforementioned environmental conditions to obtain more accurate irradiance estimation.

6.2.2.2 PV module operating temperature: simulated vs. experimental data

Considering that the estimation of a PV module operating temperature represents one of the crucial aspects to accurately predict its output power, we checked also that the estimation of a bifacial PV module operating temperature via the aforementioned NOCT formula [90] provided reliable results. Therefore, we compared the module operating temperature estimated by means of such formula, with experimental data (according to the method described in the previous subsect. 6.2.1). The main results of such a comparison are reported in Fig. 6.11, with reference to a test day in October 2018. Similar results were observed also in other test days.

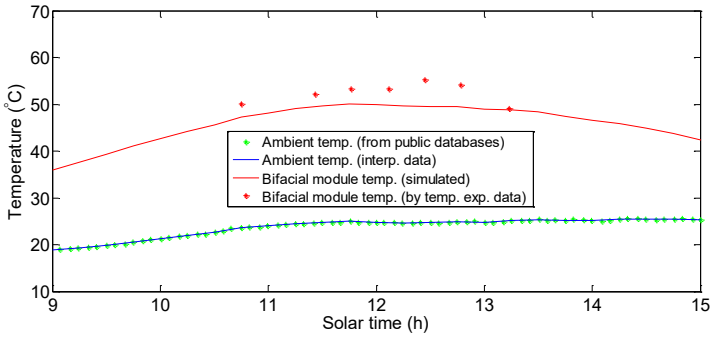

Fig. 6.11 – Comparison between simulated (as calculated by the model proposed, by using the NOCT formula [90]*) and experimental (as obtained from the measured temperature values of the tested bifacial PV module front and rear sides) trends of the tested bifacial PV module operating temperature, during a test day in October 2018. The ambient temperature trend during the mentioned test day (as taken from a public database* [74]*) is shown too.*

As we see from the graph in such figure, a good agreement was found among the experimental and simulated data of the tested PV module operating temperature, with a deviation of about 6% around midday.

6.2.2.3 Results by varying the module elevation

By varying the module average elevation from the soil (see Figs. 6.12, 6.13), the model ensures a very good forecasting of the experimental results (with deviations under 0.5% referred to the module short circuit current and 0.7% approx. with reference to its maximum power density). It should be noted that the forecasting of the power density is more arduous if compared to the PV device photocurrent prediction. Actually, for the photocurrent estimation, the ground albedo contribution represents the only critical aspect. Instead, the PV device maximum power point estimation is a trickier task, by needing an accurate estimation of both the photocurrent and the PV device temperature (as mentioned before, in subsect. 6.2.2.2). However, the model herein proposed has allowed a good reproduction of the experimental results, both in terms of the module photocurrent and its maximum power density.

It is important to note that the results obtained from the model proposed by varying the PV module elevation depend strongly on the reflection characteristics of the back-diffuser, that is, whether the area of the back-diffusing ground is confined, as typically occurs in a PV field with a high PV module density, or not. If the area is confined, the optimal module elevation is much lower compared to the case in which the back-diffuser is not confined, as it is easy to deduce by observing Figs. 6.12 and 6.14. Actually, from Fig. 6.12 a. and b., we note that, in the case of an unconfined back-diffuser, by increasing the module average elevation, initially the module short circuit current tends to grow, as well as the mean value of the short circuit currents generated by the rear sides of the module solar cells. As it is well-known from the literature (for instance, see [76]) and it has been underlined herein (see chapter 5, section 5.2.1), this fact is essentially due to the increasing reflective area which is seen by the module rear side when the module elevation increases, in addition to a reduction of the module self-shading effect which involves a better utilization of the reflecting surface. However, if we consider a confined back-diffuser, our model predicts that (see Fig. 6.14) when the module elevation increases, a reduction of the module short circuit current values and of the mean value of the short circuit currents generated by the cells rear sides is expected. This is reasonable, considering that by increasing the module elevation an increase of the distance from the source of the reflected light and a decrease of the solid view angles (as defined in Fig. 6.2) occur and such facts lead to an overall reduction of the module back photocurrent in the case of a confined back-diffuser [101].

Furthermore, it is noteworthy that, as we can observe from both Figs. 6.12 c. and 6.14 c., when the module elevation from the ground increases, a significant decrease of standard deviation of the short circuit currents generated by the cell rear sides occurs, as a consequence of reduction of illumination unevenness level of the module rear side (consistently to the study in [76]).

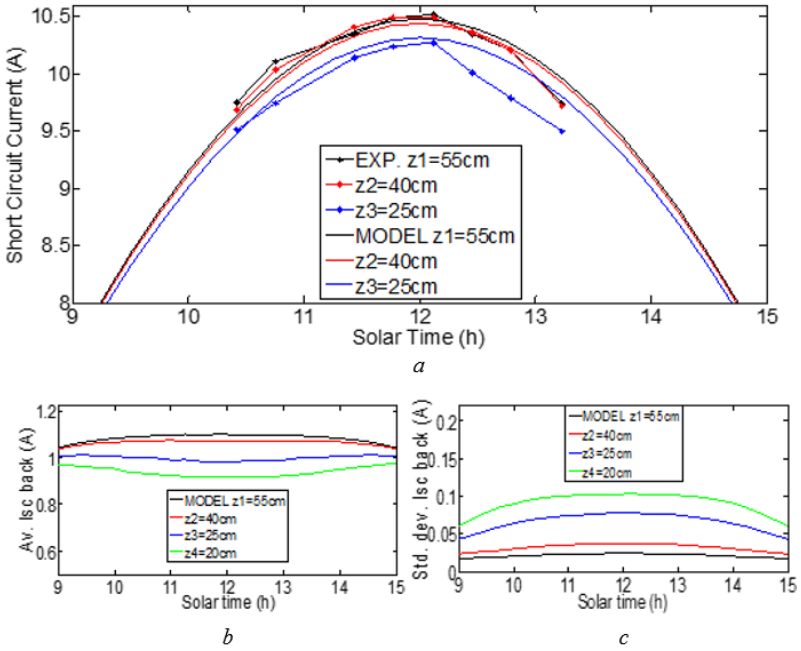

Fig. 6.12 - Results by changing the module average elevation from the soil (considering a not limited back-diffuser): a. simulated vs. experimental data (module short circ. current); simulated trends of b. mean value of the short circuit currents of the module cell rear sides, c. standard deviations of these currents.

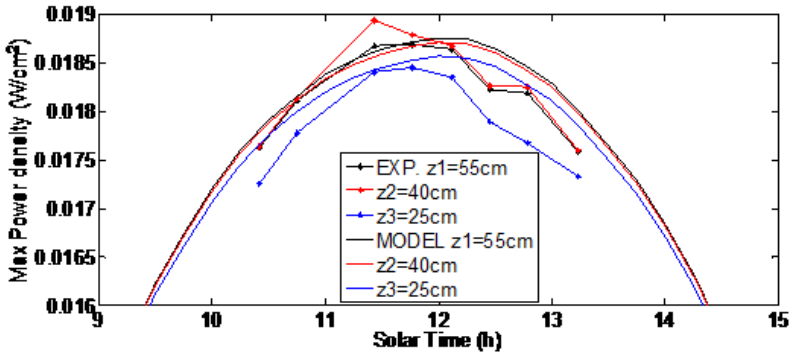

Fig. 6.13 - Simulated vs. experimental data of the module maximum power density, by changing the module average elevation from the soil.

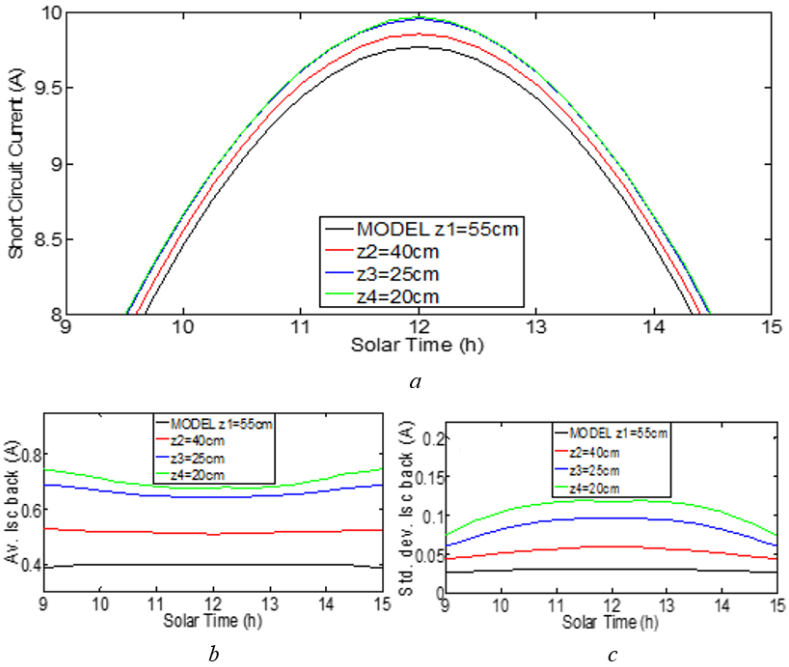

Fig. 6.14 - Simulated trends, as predicted by the model here proposed considering different module average elevations from the soil and a confined back-diffuser (made of a square asphalt area equal to 1 m^2), of: a. module short circuit current, b. mean value of the short circuit currents of the module cell rear sides, c. standard deviations of these currents.

6.2.2.4 Results by varying the module tilt angle

Fig. 6.15 shows the main validation results of the proposed model, in terms of both module short circuit current and maximum power density trends, when the module tilt angle is varied. As we can observe, also in this case a good agreement between the experimental and simulated (i.e. as calculated by our model) results was obtained. In particular, at midday and for 20° module tilt angle, maximum deviations of about 1.3% and 1.8% are observable, for the module short circuit current and maximum power density, respectively.

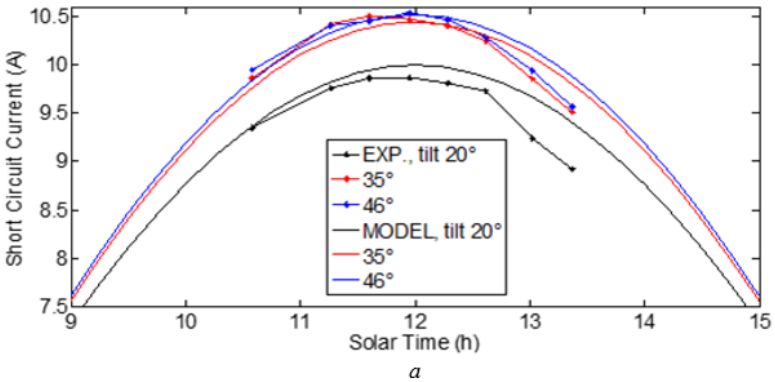

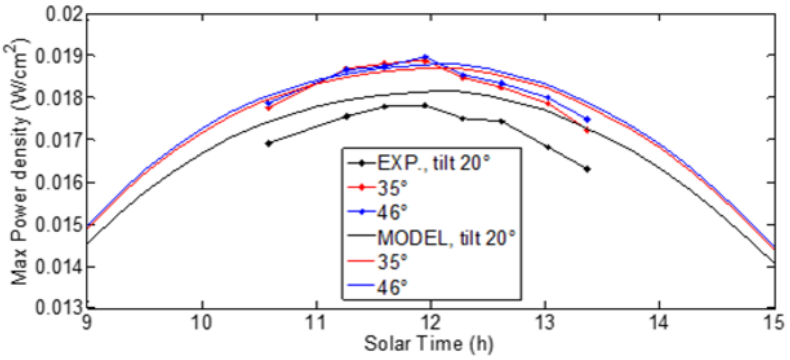

b

Fig. 6.15 - Comparison, by varying the module tilt angle, between simulated and experimental data of: a. module short circuit current, b. module maximum power density.

6.2.2.5 Results by varying the ground reflectivity

In order to validate the model presented in this work when the soil reflectivity changes, we have performed experimental tests by varying the bifacial module location respect to a white square back diffuser (with area equal to 1 m^2) surrounded by asphalt, as illustrated in Fig. 6.8 b. In Fig. 6.16, the comparison among experimental and simulated trends of module short circuit current and module maximum power density are presented with reference to the latter case.

The simulated trends shown in Fig. 6.16 (see continuous curves) were obtained by considering in the model proposed a suitable albedo matrix. This matrix considers the normal incidence reflectivity trends, measured in the 300-1100 nm wavelength range, of the materials over which the bifacial module is placed (as they have been illustrated in Fig. 6.9).

Also in the latter case, from Fig. 6.16 we note that the trends simulated by the model are quite near to the experimental ones, even if a deviation of the order of 1% is observable [101].

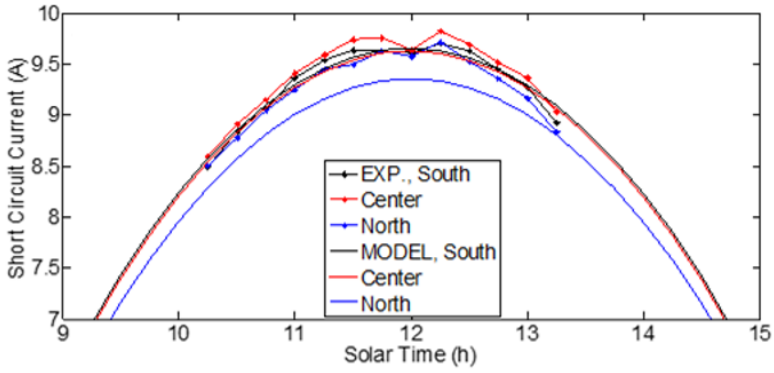

a

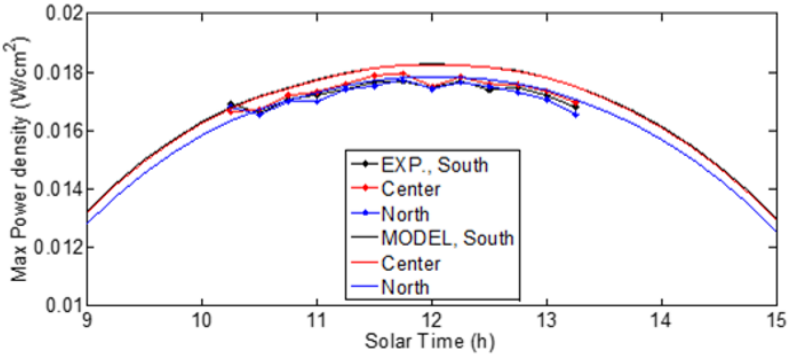

b

Fig. 6.16 - Main results, by varying the soil reflectivity: comparison among simulated and experimental data of a. module short circuit current and b. module maximum power density (by changing the module location, as shown in Fig. 6.8 b.).

6.3 Summary and conclusions

In this chapter the activities of development and experimental validation of a novel model for predicting the performance of bifacial photovoltaic modules have been presented. Initially, the model proposed has been thoroughly described, by highlighting its main features. It should be recalled here that the mentioned model is implemented in Matlab and it allows to predict a bifacial PV module performance for any geographical location. Moreover, in the model the effect of the uneven distribution of the irradiance at the PV module rear side is fully considered, as an important aspect to accurately forecast a bifacial solar device performance. The experimental activities carried out for the validation of the proposed model has been also duly described and the main validation results have been illustrated and discussed. In this regard, a very good agreement among the simulated and experimental data has been observed (with very low deviations of the order of 1-2%), both in terms of short circuit current and maximum power density of a bifacial PV mini - module, tested in Catania. The accurate prediction of the module maximum power density, which generally depends also on the module operating temperature, was obtained thanks to a sufficiently accurate prediction of such temperature (as proved by the comparison with experimental data). Contextually, the behavior peculiarities of a bifacial PV module have been shown, when the main parameters (module elevation from the ground, module tilt angle, and ground reflectivity) affecting its electrical performance are changed. In particular, the different behavior of a bifacial device by changing its elevation from the ground, in the cases of a confined and unconfined rear diffuser, has been highlighted. In the ideal case of an unconfined rear diffuser, the bifacial PV module short circuit current and the mean value of the back photocurrents of the module solar cells tends to grow by increasing the module elevation over the ground. This occurs essentially because the soil area seen by the module rear side, contributing to the light collected by such side, increases too. Conversely, when the soil area behind the module is confined, as it typically occurs in the real case of a module inserted into a PV field, the model predicts a decrease of the aforementioned

short circuit current and the mean value of the rear photocurrents of the module PV cells. This is reasonable explained by considering that actually, when the module elevation over a confined rear diffuser is increased, the distance from the light source increases too, ultimately leading to a performance decrease of a bifacial PV module.

CHAPTER 7 PERFORMANCE PREDICTION OF BIFACIAL PV STRINGS WITH AND WITHOUT UNIAXIAL HORIZONTAL SOLAR TRACKER: ANALYSYS OF PERIMETER EFFECTS AND INFLUENCE OF THE LATITUDE

The present chapter focus on the prediction of energy generation of PV strings with and without uniaxial horizontal solar tracker, installed at different geographical locations. Initially (see section 7.1), some general considerations will be made on the importance of analyze the perimeter effects, to accurately predict a bifacial PV string performance. Furthermore, we underline the relevance of evaluating the influence of the mentioned type of tracker on such performance, also in relation to the latitude. Subsequently (see section 7.2), the model used for the analyses in this chapter will be described in detail as well as the main assumptions made to conduct these analyses. Finally, the most relevant results provided by such model will be illustrated and thoroughly discussed, by highlighting the perimeter effects able to influence a bifacial PV string performance (see section 7.3) and the effect induced by the latitude on the performance of bifacial and mono-facial PV strings (see section 7.4). Contextually, we will discuss the convenience of adopting uniaxial horizontal solar tracker for the mentioned PV strings.

7.1 General considerations

As mentioned previously (see chapter 5, herein), essentially to date 3D (see as examples [76],[54],[38]) and 2D (for instance, see [80],[81]) models of bifacial PV devices exist. The first ones, despite their typical complexity due to their three – dimensional approach, can lead to more accurate results, since they generally allow to fully consider the main aspects affecting a bifacial PV system performance. The model herein proposed (whose development and validation have been described in detail in the previous chapter 6) is a 3D model. Substantially, as partially remarked in the previous chapter 6, it is very relevant to consider the light hitting the module surface also with relatively grazing light incidence angles, namely the diffuse light coming from soil zones far from the module; in fact, in such way it is possible to accurately model the effects on the module performance due to variations of the module elevation from the soil, consistently with the experimental data. Since the mentioned model, by adopting a three-dimensional approach, is suitable to accurately predict the light collected by the rear side of bifacial solar cells (hence, ultimately their performance), we have recently upgraded such model

to forecast the performance of bifacial PV strings, in order to analyze the role of perimeter zones on the mentioned performance. This is a very interesting subject which till now has not received enough attention. For this purpose, as it will be clarified below (see sections 7.2 and 7.3), PV strings consisting of 30 or 60 modules have been considered, for both the cases of a fixed installation (with PV modules near optimally tilted) and of a PV string equipped with uniaxial horizontal solar tracker (i.e. one of the most widespread in real PV systems). It should be noted that the latter study case for a bifacial PV string appears of great interest to us. In fact, although till now several studies in the literature analyzed the effect due to solar trackers on the performance of traditional mono-facial PV systems and solar collectors (for instance, see [102–115]), currently few recent studies exist (see [116–118]) about similar analysis for bifacial PV systems. Therefore, further studies seem to be needed, also considering the latitude effect on the latter system performance. In this perspective, by means of the aforementioned upgraded model, we have also analyzed the influence of the latitude on the energy production of PV strings, both bifacial and mono-facial ones (by comparing their performance at the same installation conditions), as we will discuss in depth in section 7.4.

7.2 Model used to predict the performance of PV strings: description and main assumptions

To address the problem of modeling a bifacial PV string behavior, for the aims of the study in question (as highlighted in the previous section 7.1), for the case of PV string with uniaxial horizontal solar tracker we have considered the module placement geometry schematized in Fig. 7.1. According to such schematic representation, the PV string consists of two module rows parallel to each other and parallel to the tracker rotation axis, oriented along the meridian passing through the geographical location considered. The considered PV strings consist of 30 or 60 modules; hence, each row can contain 15 or 30 modules.

For the other case considered in this study, namely the one of a fixed PV string (i.e. in absence of solar tracker), the geometry is substantially like the one schematized in Figure 7.1, with the only difference that the fixed string is rotated of 90 degrees, compared to the string with solar tracker in such figure. For the fixed string, the PV modules are considered inclined on the horizontal plane of an angle (the module tilt angle) equal to the latitude of the geographical location considered and oriented towards south (since we consider only the northern terrestrial hemisphere).

Concerning the notation to individuate the PV modules within the string, we indicate with x the direction along the meridian and with y the direction along the parallel passing through the geographical location considered, and the corresponding module indices are named ix and iy, respectively. Therefore, for the case of string with tracker, ix varies between 1 and 15 (or 30) and iy varies between 1 and 2. Instead, for the fixed string, ix varies between 1 and 2 and iy varies between 1 and 15 (or 30).

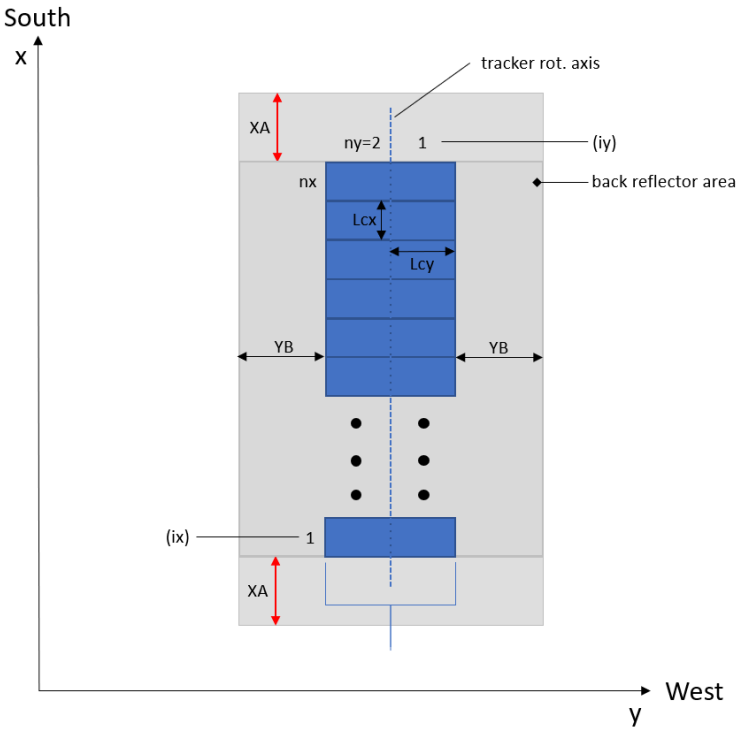

Fig. 7.1 - Schematic drawing of the module placement geometry for the case of PV string with uniaxial horizontal solar tracker considered in this study. For the case of a fixed PV string, the same geometry is considered, although the fixed string is rotated of 90 degrees compared to the string with solar tracker here shown. XA and YB are the parameters used in this study to identify the soil zone (acting as back reflector for the bifacial PV devices) dimensions considered for the calculations. nx represents the total number of string PV modules along the x direction. Similarly, ny indicates the total number of string PV modules along the y direction.

Regarding the 3D model here used for the study in question, as mentioned before, the model described in the previous chapter 6 has been recently upgraded, to allow the performance prediction for PV strings both without (fixed string) and with uniaxial horizontal tracker. In particular, the calculation of the short circuit current values of the front ($I_{sc,front}$) and rear ($I_{sc,rear}$) sides of a bifacial solar cell (and consequently of its current vs. voltage electrical characteristics) is carried out according to the procedure described in detail in chapter 6 (see equations (6.2) and (6.3), respectively). Strictly speaking, such procedure should be repeated cell by cell for each bifacial PV module (as actually it had been considered in chapter 6). However, since for the study now in question we have considered relatively large strings of 30 or 60 PV modules, each one composed by 72 cells (hence, for a total number of cells per string equal to 2160 or 4320), to simplify the modeling, we have neglected the difference among the cells within the same module and the electrical characteristics of a PV module are evaluated by considering that its cells are illuminated in the same way. Nevertheless, the uneven distribution of illumination at the rear side is considered among the different modules making up the considered PV strings. Note that

it seems to be reasonable, since actually the differences of solid angle (see chapter 6 for its definition) are more relevant among neighboring modules within a PV string, rather than neighboring solar cells.

As an example, Fig. 7.2 shows the trend of the solid angle under which each soil element sees the central solar cell of the module at the location ix = 2, iy = 7 (approximately, the central position) of the considered fixed string of 30 modules. In such figure, we see also the shadow projected by the string, as calculated at the latitude of Catania, Italy, at 4 p.m. of the day number 47 of the year 2018.

The bifacial solar cells making up the strings here considered are those whose characteristics have been specified in the previous chapter 6. Each bifacial PV module consists of 72 of such cells, its dimensions are 1 m x 2 m and its maximum power at the Standard Test Conditions (STC) is equal to 326 W.

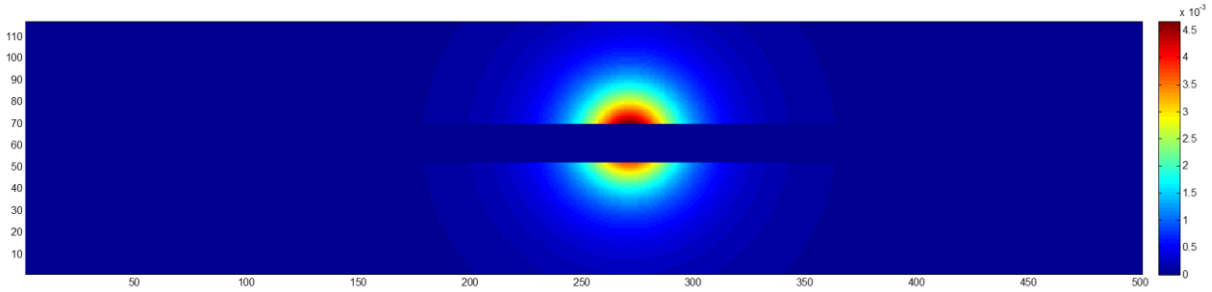

Fig. 7.2 - Trend of the solid angle (values indicated by the multicolor bar on the right), under which each soil element sees the central solar cell of the module at the location ix = 2, iy = 7 (approx. the center) of the fixed PV string of 30 modules. The shadow projected by such string, at the latitude of Catania, Italy, at 4 p.m. of the day n. 47 of 2018, as simulated by the proposed model, is shown too. On the abscissa and on the ordinate, the y and x coordinates, respectively, of Fig. 7.1 are reported.

The evaluation of the PV module operating temperature (T_{module}) has been carried out through the NOCT formula (introduced in chapter 5, see equation (5.3)), by considering the ambient temperature profiles and the irradiance at the module front surfaces. For all the geographical locations considered in this study, the ambient temperature profiles have been retrieved by the already cited available online public database [74]. The irradiance at the module front surfaces have been evaluated by the equation (6.1) (see chapter 6).

Finally, once the current vs. voltage (I-V) electrical characteristics of all PV modules are determined (under the simplification described previously), the I-V electrical characteristics of the considered string are determined, by calculating numerically the series of all modules of the string. Figure 7.3 shows some examples of module I-V characteristics (see red curves) and the corresponding electrical characteristics of string (see blue curves), as calculated at time intervals of 1 hour, between 7 a.m. and 5 p.m. of the day n. 180 at the latitude of Catania, Italy, for both the cases of a fixed string (see Fig. 7.3 a.) and a string with uniaxial horizontal solar tracker (see Fig. 7.3 b.) of 30 modules. As we can see from the

graphs in such figure, concerning the current values, the characteristics are almost overlapped between the morning and the afternoon at symmetrical times respect to midday. In other words: at low voltages, the current values for example at 9 a.m. are similar to the ones at 3 p.m. However, near the open circuit voltage (Voc), the characteristics are sensibly different to each other, as a result of variations of module operating temperatures. For instance, such temperatures are lower at 9 a.m. compared to the ones at 3 p.m., therefore, the Voc value results higher at 9 a.m. compared to the one at 3 p.m.

Furthermore, we note that the I-V characteristics of the strings exhibit quite high slopes at low voltages. This is due to the illumination unevenness of the rear surfaces of the string PV modules and the consequent different values of $I_{sc,rear}$ of such modules. For the cases of Fig. 7.3, such an effect is clearly more evident for the fixed string.

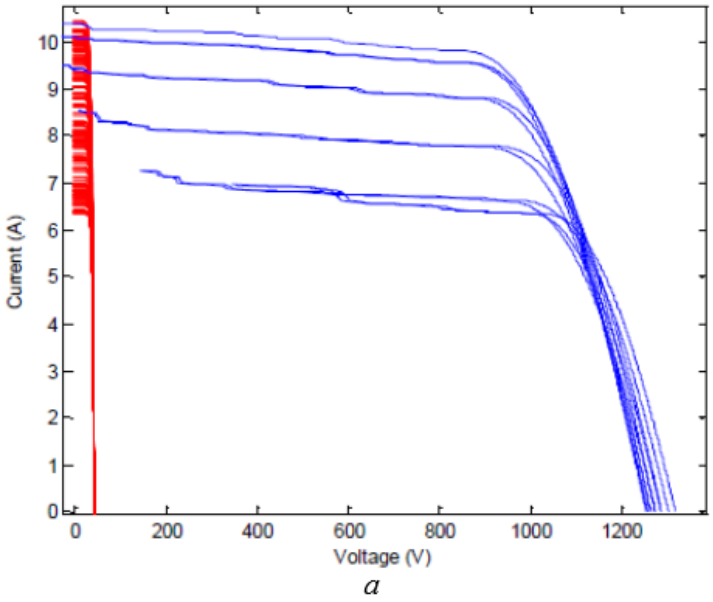

a

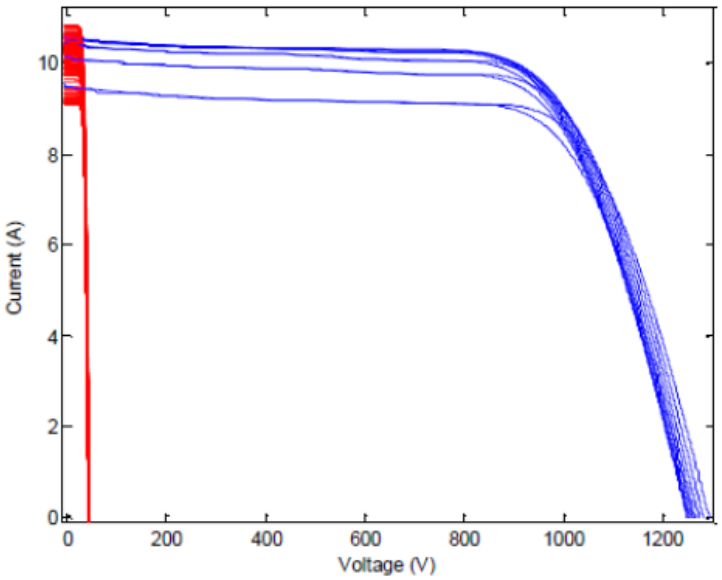

b

Fig. 7.3 - Examples of module I-V characteristics (red curves) and the corresponding electrical characteristics of a string of 30 modules (blue curves), as calculated at time intervals of 1 hour, between 7 a.m. and 5 p.m. of the day n. 180 at the latitude of Catania, Italy, for both the cases of: a. fixed string, and b. string with uniaxial horizontal solar tracker.

7.3 Perimeter effects: main results and discussion

As mentioned previously, the proposed model carries out a 3D calculation. Therefore, it has been used for the relevant purpose to understand the role of the soil zone extent contributing to the light collected by the string (hence contributing to the photocurrent generated by the string). Obviously, such extent is actually limited by the critical incidence angle ($\theta_{crit.}$, introduced in chapter 6). In fact, the incidence angle of the radiation coming from a soil element very far from the bifacial PV devices tends to 90°, therefore such radiation is reflected and ultimately not collected by the PV string.

As an example, Fig. 7.4 shows the short circuit currents generated by the rear sides of the different PV modules (30 modules) of the string, for the case of fixed string, at the latitude of Catania, Italy, at 10 a.m. of the day n. 79 of the considered year, with module tilt angle of 35° (i.e. near to the optimal tilt angle for the mentioned latitude), with XA = 5 m and YB alternately equal to 0 m, 5 m, 10 m, and 20 m (for the definition of the parameters XA and YB, see Fig. 7.1). From this figure, we clearly see that by increasing YB (according to the row direction in Figure 7.4), the photocurrent values of the modules at the string extremities (for instance, see the modules at the locations identified by iy = 1 and iy = 15) increase. This is intuitively expected, since the soil zone contributing to the PV string rear side illumination increases too. Moreover, we observe a saturation, namely the photocurrent values corresponding to YB equal to 10 m and 20 m are practically the same (as we see from the upper curves

in Fig. 7.4, which are substantially overlapped for the cases of YB = 10 m and YB = 20 m). In general, it appears evident that the perimeter effects are important, anyway.

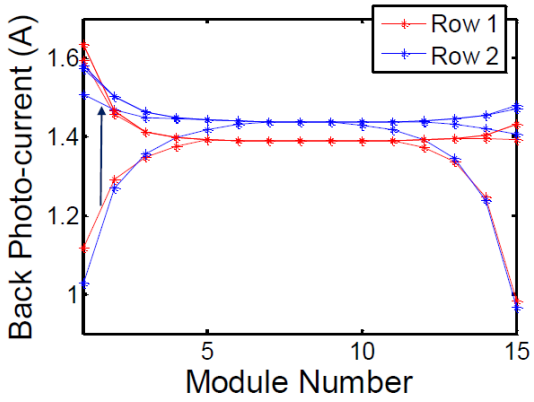

Fig. 7.4 - Short circuit currents generated by the rear sides of the different PV modules (30 modules) of the string, for the case of fixed string, at the latitude of Catania, Italy, at 10 a.m. of the day n. 79 of the considered year, with module tilt angle of 35° (i.e. near to the optimal tilt angle for the mentioned latitude), XA = 5 m and YB alternately equal to 0 m, 5 m, 10 m, and 20 m (for the definition of the parameters XA and YB, see Fig. 7.1). The arrow (in the graph, near to the curves) represents the direction of increasing YB.

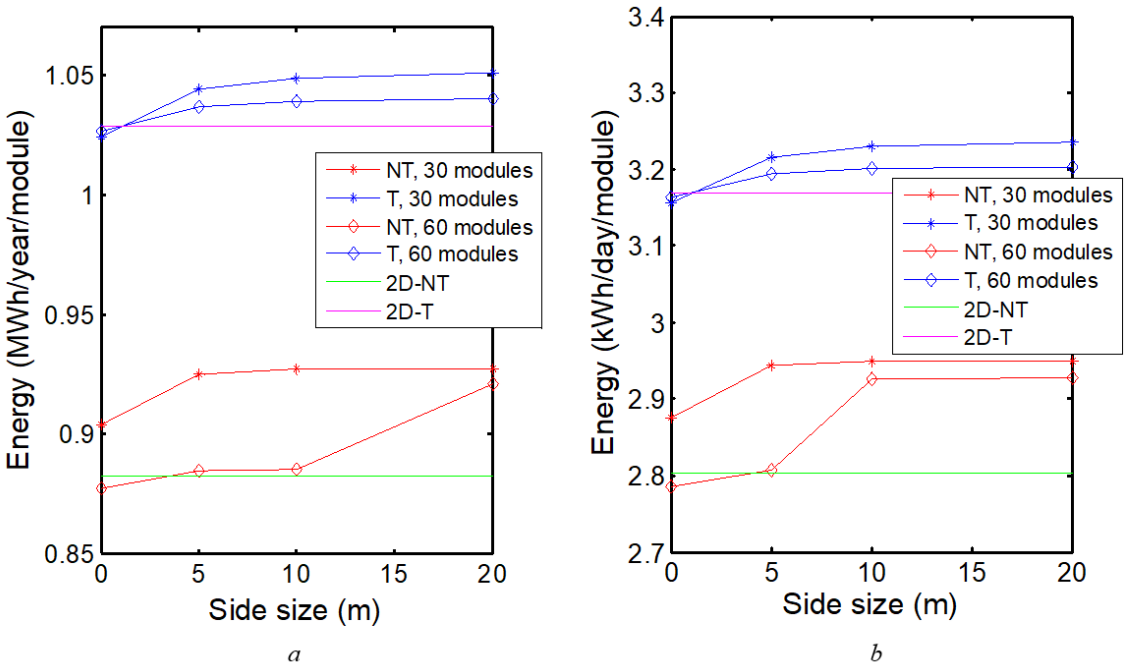

Fig. 7.5 –Perimeter effect on the energy normalized per module generated by the PV string, for the cases of fixed PV string (see NT symbol in the legend, acronym of no tracker) and of PV string with uniaxial horizontal solar tracker (see symbol T in the legend, acronym of tracker), formed by 30 or 60 modules, at the location of Catania, Italy: (a) specific energy per year trends, as calculated by the proposed model (considering the year 2018), (b) specific energy per day trends, as calculated by considering the day n. 79 (spring equinox) of the year 2018. The generated energy is shown as a function of the parameter XA (for fixed YB = 5 m) for the case of string with tracker, or of the parameter YB (for fixed XA = 5 m) for the case of fixed string. Note that the magenta and green continuous lines represent the energy values which would be

estimated under the 2D approximation, i.e. the values obtained at the limit for $nx \to \infty,\ ny = 2,$ $XA = 0$ *(see Fig. 7.1) for the case of string with tracker, and for* $ny \to \infty,\ nx = 2,\ YB = 0$ *for the case of fixed string. The PV string behavior for* $nx\ (or\ ny) \to \infty$ *was simulated by considering the behavior of the central modules (i.e. the ones at the locations* $ix\ (or\ iy) = 30$*) of the 60 module PV string (with, or without tracker).*

Fig. 7.5 shows the perimeter effect on the energy generated by the PV string, normalized for the number of modules, for the cases of fixed PV string (with modules near optimally tilted for the considered location) and of PV string with uniaxial horizontal solar tracker, formed by 30 or 60 modules, as obtained by the proposed model for the location of Catania, Italy. In Fig. 7.5 a., the specific energy per year is shown, while in Fig. 7.5 b., the specific energy per day is shown, by considering the day n. 79 (spring equinox) of the year 2018. In the graphs of Fig. 7.5, the lowest three curves are referred to the case of strings without solar tracker (i.e. the fixed strings), the upper three curves are referred to the case of strings with tracker. As we clearly see from such figure, with tracker an increase of the energy produced of about 10% is achievable. Moreover, we note that in the case of strings of 30 modules, the generated specific energy results higher than that generated by the strings of 60 modules. This can be explained by considering that, with a lower number of modules for PV string, the ratio between the soil area diffusing the light and the string total area increases, hence the photocurrent generated by the string rear side increases and consequently the overall produced energy grows too. As it has already been intuited by observing the data of Fig. 7.4, by increasing the considered side size, the string rear photocurrent, and hence also the energy produced by the string, increases, but a saturation level is achieved for a side size of about 20 m. From Fig. 7.5, such a saturation is evident for the case of PV string of 30 modules (for both the cases of fixed PV string and of string with tracker), but it is not clear for the case of PV string of 60 modules. However, we have checked that also in the latter case a saturation level of the produced specific energy is achieved, at practically the same condition above specified (side size ~20 m).

Moreover, we have evaluated the specific energy values which would be estimated under the 2D approximation (see green and magenta continuous lines of Fig. 7.5). Such values have been obtained as specified in detail in the caption of Fig. 7.5. As we clearly see, under the 2D approximation, the produced energy is underestimated; it is reasonable, by considering that with this approximation the contribute due to the soil perimeter zones is not computed, as instead it is made through the 3D modeling.

7.4 Influence of the latitude: main results and discussion

The effect of the latitude, on the specific energy produced by mono-facial and bifacial PV strings of 30 modules, with uniaxial horizontal solar tracker or without tracker (fixed string), have been evaluated, by considering five different geographical locations of the northern hemisphere, from near to the equator to near to the Arctic Circle. In particular, as installation sites for the mentioned PV strings, we have considered the locations listed below:

- Abu Dhabi, United Arab Emirates (latitude: 24° 27' 17.2" N, longitude: 54° 39' 5.9" E);
- Be'er Sheva, Israel (latitude: 31° 15' 8.3" N, longitude: 34° 47' 32.1" E);
- Catania, Italy (latitude: 37° 26' 32" N, longitude: 15° 3' 47" E);
- Freiburg im Breisgau, Germany (latitude: 48° 00' 33.7" N, longitude: 7° 50' 4.6" E);
- Aarhus, Denmark (latitude: 56° 18' 26.9" N, longitude: 10° 37' 40.7" E).

Fig. 7.6 shows the energy produced as a function of the latitude, normalized for the number of modules, for the aforementioned PV stings, as calculated by the proposed model. On the left (see Fig. 7.6 a.) the specific energy per year is shown, while on the right (see Fig. 7.6 b.) the specific energy per day is shown, by considering the day n. 79 (spring equinox) of the year 2018. For the cases of fixed PV string and of string with tracker, the parameters YB and XA, respectively, were set equal to 10 m (which, according to the results of Fig. 7.5, substantially represents the saturation condition of the perimeter effects, for the case of 30 module PV strings).

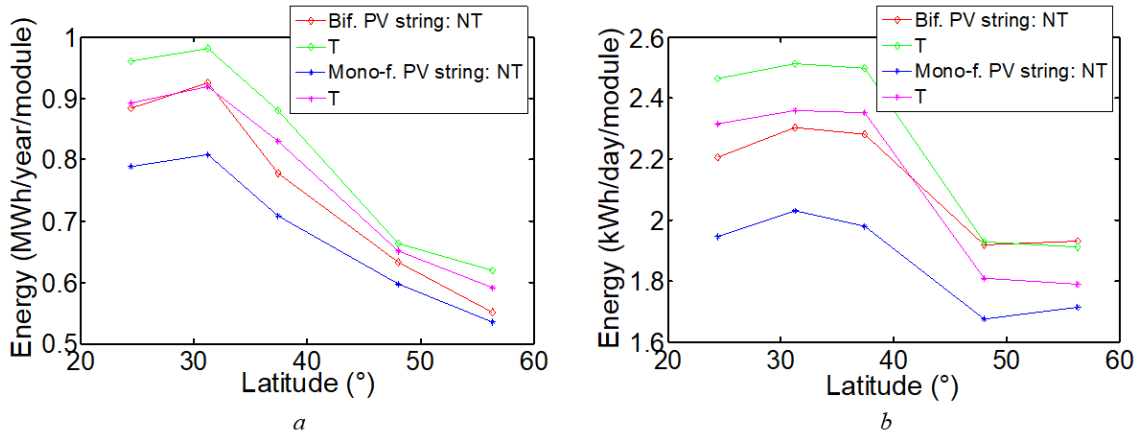

a *b*

Fig. 7.6 - Energy produced as a function of the latitude, normalized per module, for the cases of mono-facial PV stings (i.e. illuminated only from the front side) and bifacial PV strings, consisting of 30 modules, with uniaxial horizontal solar tracker (see T symbol in the legend) or without solar tracker (fixed string, with module tilt angle equal to the considered latitude) (see NT symbol in the legend), as calculated by the proposed model (considering the five locations specified in the main text): a. specific energy per year, b. specific energy per day, by considering the day n. 79 (spring equinox) of the year 2018. For the cases of fixed PV string and of string with tracker, the parameters YB and XA, respectively, were set equal to 10 m (saturation condition of the perimeter effects).

It should be noted that our model most likely leads to an overall overestimation of the energy generated by the considered PV strings, more relevant at high latitudes, essentially as a result of the overestimation of the global horizontal irradiance yearly values due to the use of the ASHRAE model, as previously discussed (see subsect. 6.2.2.1 of chapter 6). Therefore, in order to provide a more precise estimation of the energy generated by the PV strings, we have corrected the string energy values provided by our model, by taking into account the Global Horizontal Irradiance values retrieved for the geographical locations here considered by the Global Solar Atlas database [100]. The energy values reported in Fig. 7.6 consider such a correction.

By observing Fig. 7.6, we see clearly that the bifacial PV system produces significantly more energy than the mono-facial one. Moreover, the considered type of solar tracker gives a clear advantage in terms of generated energy, compared to the fixed PV system. However, such an advantage decreases, by increasing the latitude. This fact is consistent with the findings of the study [113], referred to the case of PV systems equipped with traditional mono-facial PV modules. Moreover, by further observing Fig. 7.6, we note that the energy gains achievable by using the considered solar tracker is greater for the case of mono-facial PV string, compared to the case of bifacial PV string, consistently with the results obtained in [116]. However, in this regard, it is strongly important to note that the model proposed and used in the present work is based on a tracking algorithm which considers the irradiance optimization only on the module front side (i.e. the so-called azimuth optimization), rather than the optimization of the irradiance on both front and rear surfaces of the bifacial modules. By changing the tracking algorithm, so that an irradiance optimization also on the rear sides of bifacial PV models can be obtained, it is possible that the energy produced by a bifacial PV system with tracker can be increased [119].

It should be noted that, according to the results of Fig. 7.6, for a given PV string, the values of energy produced at high latitudes result in some cases near or greater than the ones at lower latitudes, despite generally for these latter latitudes (typical of locations near to the equator) very high global horizontal irradiance values are observable. Obviously, this occurs as a result of the module operating temperatures which typically are significantly higher (by penalizing the module performance) at locations near to the equator (as for instance, Abu Dhabi), compared to the ones at locations far from the equator (as for instance, Freiburg), consequently to the considerable different ambient temperature profiles among such geographical locations (as for instance, it can be checked from the meteorological data in [74]).

Concerning the convenience to install a uniaxial horizontal solar tracker with the purpose of increasing the energy production of a fixed PV system, a cost – benefit analysis should be carried out case by case. However, by critically interpreting the data illustrated in Fig. 7.6, it seems reasonable to speculate that for geographical locations at high latitudes, in order to obtain an increase of energy produced compared to a fixed mono-facial PV system, it could be convenient to install a fixed bifacial PV system, rather than adopting the mentioned type of solar tracker.

Finally, it is should be noted that, in order to check the reliability of the results provided by the model here proposed and used, we have performed a comparison among the experimental results obtained in [114] for two test PV systems and the results provided by the mentioned model, by considering the same installation conditions. In particular, in [114] the authors carried out an experimental study to compare the performance (on a monthly scale) of a mono-facial fixed PV system (with modules oriented towards south, near optimally tilted, in relation to the latitude of the installation site) and another mono-facial PV system with the same geometrical characteristics of the fixed one, but equipped with uniaxial horizontal solar tracker (with rotation axis oriented along the north – south direction). Both such systems were installed near to each other, at the Florida Atlantic University (Boca Raton, FL, USA, latitude: 26.21° N, longitude: 80.04° W). As mentioned previously, we have compared the experimental results (in terms of monthly energy gains due to the uniaxial horizontal tracker) obtained by the mentioned authors, with the ones simulated by our model, with reference to the same geographical coordinates of the installation site and geometrical characteristics of the PV systems considered in the work above cited. Obviously, as input for the model, the ambient temperature profile at the geographical location considered in [114] has been used, as retrieved by the meteorological database in [74]. Fig. 7.7 shows the results of the mentioned comparison. As it is evident from the graph in such figure, overall the results provided by the model here proposed (see the blue continuous line in the graph) are on average quite near to the ones experimentally obtained in [114] (see the red starred line), albeit some deviations are observable with reference to some months.

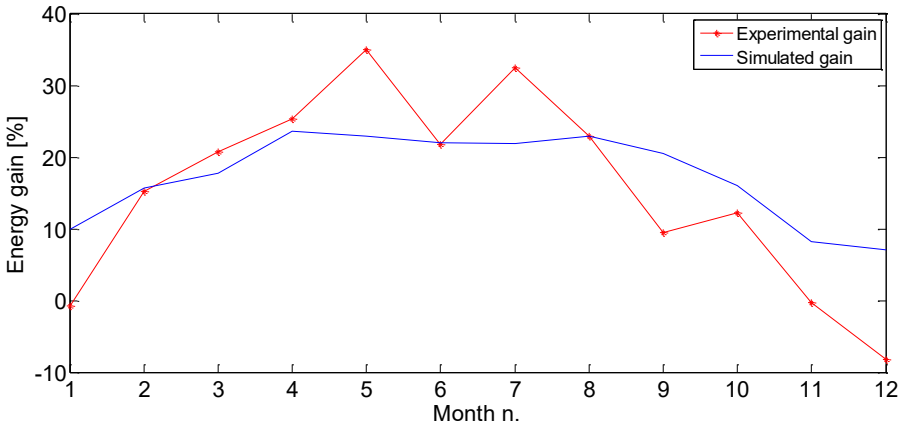

Fig. 7.7 - Percentual monthly energy gain due to uniaxial horizontal solar tracker, compared to an optimal tilted mono - facial fixed PV system in Boca Raton, Florida, USA. The dotted red curve indicates the energy gain, as experimentally obtained in [114]*. The blue continuous line represents the simulated energy gain, obtained by the mathematical model proposed in the present thesis work.*

7.5 Summary and conclusions

This chapter has been focused on the prediction of PV string energy generation, with and without uniaxial horizontal solar tracker, at different geographical locations.

The first section of the chapter has been dedicated to general considerations on the importance of analyze the perimeter effects, to accurately predict a bifacial PV string performance. Here, we have also underlined the relevance of evaluating the influence of the mentioned type of tracker on such performance, also in relation to the latitude.

The second section of this chapter has concerned the in-depth description of the model used for the analyses carried out as well as the main assumptions made. Here, we have to remember the following. Essentially, for the aim of these analyses, the model presented in chapter 6 was upgraded to allow the prediction of bifacial PV strings, under the main simplifying assumption here below. The difference among the cells within the same module has been neglected and the electrical characteristics of a PV module have been evaluated by considering that its cells are illuminated in the same way. Nevertheless, we have fully considered the uneven distribution of illumination at the rear side among the different modules of a PV string.

In the last part of the chapter, the most relevant results of the mentioned analyses have been illustrated and thoroughly discussed. In this regard, we have firstly highlighted that the perimeter effects are able to significantly influence a bifacial PV string performance. In particular, our results have clearly shown the following. By increasing the soil perimeter zones near to the string extremities, the string rear photocurrent, and hence also the energy produced by the string, initially increases, but a saturation level of such an effect is achieved, over which the string output energy remains practically constant by further increasing the mentioned perimeter zones. According to our results, such a saturation level is achieved for a soil perimeter zone having a width of the order of 10-20 m for a 30 module PV string. Finally, the effect induced by the latitude on the performance of bifacial and mono-facial PV strings has been thoroughly studied, by contextually discussing the convenience of adopting uniaxial horizontal solar tracker for these PV strings. In this regard, we remember the following main findings. A bifacial PV string allows to produce significantly more energy than a mono-facial one, at the same installation conditions. The adoption of the mentioned type of tracker determines a clear advantage in terms of generated energy, compared to the fixed PV string. But such an advantage decreases by increasing the latitude (as also proved by different studies in the literature). Furthermore, the results presented in this chapter have shown that the energy gains achievable through the considered solar tracker are greater for a mono-facial PV string, compared to a bifacial PV string. However, it should be underlined that our model considers a tracking algorithm based on the irradiance optimization only on the module front side; by changing the tracking algorithm, so that an irradiance optimization also on the rear sides of bifacial PV models can be obtained, it is possible that the energy produced by a bifacial PV system with

tracker is increased. On the convenience to install a uniaxial horizontal solar tracker to increase the energy generated by a fixed PV system, a cost – benefit analysis should be performed case by case. Based on our results, we can speculate that for geographical locations at high latitudes, it could be convenient to install a fixed bifacial PV system, rather than adopting the mentioned type of solar tracker, to increase the electricity generated by a fixed mono-facial PV system.

CHAPTER 8 GENERAL CONCLUSIONS

The present chapter, as conclusive section of this Doctoral thesis, is dedicated to a synthesis of the most relevant findings of such Ph.D. work, on the basis of the global set of the experimental research activities carried out, as herein illustrated and thoroughly discussed. At the end, some possible future developments of this work will be highlighted.

Basically, main object of the mentioned Ph.D. work was the performance optimization of thin film Silicon and bifacial photovoltaic (PV) devices, through an in-depth study of their behavior by varying the outdoor variables affecting their electrical performance.

The first part of such work was focused on the study of performance instability phenomena affecting tandem amorphous/microcrystalline Si mini - modules under variable working conditions, instead the second part was focused on the study of the behavior of bifacial PV systems and on the optimization of their performance.

Concerning the first part, the major conclusions have already been highlighted carefully herein (see chapter 4). Here, in summary, it should be remembered the following most relevant facts. The experimental tests performed on not stabilized specimens of the aforementioned type of PV mini - modules allowed to confirm that the application of DC reverse bias stresses under illumination determine considerable performance recovery/improvement of such devices (as it was seen in the literature, prevalently on single solar cells of the type in question). However, since a considerable energy consumption (of the order of 1 kWh/m^2, given the quite long stress time needed of the order of hours) is requested to perform these stresses, practically such a technique is not convenient for recovering/improving the mentioned PV device performance. In addition, no performance improvement was observed on stabilized specimens (namely, subjected to a 1000 hours light soaking before our stress tests) of the same type of mini – modules, under the abovementioned stresses. Nevertheless, the tests performed outdoor on the latter stabilized specimen, exclusively working in Maximum Power Point condition, allowed to observe interesting instability phenomena, whose causes were thoroughly analyzed. Substantially, performance worsening phenomena during the morning followed by performance improvements during the afternoon were observed on a daily scale, systematically. The careful study of the mentioned causes led us to conclude that the mini – module operating temperature variations play a fundamental role on the performance instability observed. In particular, we demonstrated the following. Subsequently to the light induced degradation occurring evidently during the morning, actually a thermal annealing at moderate temperatures (of the order of 40-50 °C) around midday was to be considered the main cause of the mini – module performance improvement observed in the afternoon. In fact, an annealing of the defects formed during the morning light induced degradation

phase was substantially associated to the mentioned thermal annealing around midday. Instead, it was proved that the solar spectrum variations, observed over the course of the day, had a marginal role. Moreover, it was observed that the higher was the maximum temperature achieved by the solar cells during their operation (namely, the more intense was the solar cell thermal annealing), the higher the observable power conversion efficiency growth became. Therefore, despite the Staebler-Wronski effect certainly is a limiting factor for the studied PV device performance, it is also true the following. If such devices, during their operation in MPP, achieve moderately high maximum temperatures (of the order above reported) even for short time intervals (of the order of one hour), some efficiency recovery will occur, as a result of the defect annealing. In our experiments, we observed an efficiency recovery of the order of 2-3%, but higher recoveries are expected for higher cell maximum temperatures. Such an important finding has allowed to support the concept that the thin film tandem amorphous / microcrystalline Si PV devices are particularly suitable for the use in hot climate regions, where significant benefits can be obtained in terms of electricity generation, by exploiting the specific thermal behavior of such devices.

With reference to the second part of this Ph.D. work, the most important aspects and conclusions are detailed here below. For the purpose of carefully studying the performance and behavior of bifacial PV devices, a novel analytical 3D model to accurately predict the electrical performance of bifacial PV modules, usable for any geographical location, was developed and proposed and its accuracy validated through a significant number of experimental tests outdoor. This allowed, on one hand, to analyze in-depth the behavior of bifacial devices and their performance optimization, by varying the main outdoor variables affecting such performance in real operating conditions. On the other hand, it has been possible to predict the electricity generation of bifacial PV strings, both fixed ones (i.e. in absence of solar tracker, with PV modules near optimally tilted at the location considered for their installation) and equipped with uniaxial horizontal solar tracker, by considering different geographical locations (from near to the equator to near to the Arctic Circle). In particular, initially, a first version of the mentioned model was developed for accurately foreseeing the performance of a single bifacial PV module, by taking into account the uneven distribution of the irradiance at its rear side (as an important aspect to obtain accurate performance prediction of bifacial devices, according to the recent scientific literature on the subject in question). We performed a careful comparison among the results provided by this model and the experimental ones, obtained through tests outdoor on a bifacial PV module (having four PERT bifacial solar cells connected in series), by varying the main parameters able to affect the performance of a bifacial PV module (namely, its elevation from the soil, its tilt angle and the ground reflectivity). This comparison allowed to observe a very good agreement among such results (with very limited deviations, of the order of 1-2%, referred to the module short circuit current and output power density). We observed that for a good modeling of the effects on the module performance due to variations of the module

elevation from the soil (consistently with the experimental data), the following relevant aspect has to be considered: the light hitting the module surface also with relatively grazing light incidence angles, namely the diffuse light coming from soil zones far from the module. The mentioned model first version was upgraded to allow the performance prediction of bifacial PV strings, with the main purpose of studying the role played by perimeter zones on the mentioned performance, as a very interesting subject which till now had not received enough attention in the literature. The upgraded model version, even if based on the simplification of not accounting for the irradiance uneven distribution at the rear side of each module of a PV string, anyway it allowed to consider the illumination uneven distribution at the string rear side. Indeed, the different illumination of the different modules of a PV string was fully considered. This, together to the fact which the model herein proposed adopts a three-dimensional approach to fully consider the main aspects affecting a bifacial PV system performance, allowed to highlight that actually the soil perimeter zones have significant effects (hence, not negligible in general) on the performance of a bifacial PV string. It was found that a saturation condition exists for the perimeter effects, in terms of a side size of the soil zone near to the PV string extremities. Such a saturation condition resulted of the order of 10-20 m for a 30 module PV string. In other words, it was noted that, by increasing the considered side size, the string rear photocurrent, and hence also the energy produced by the string, initially increases, but a saturation level of such an effect is achieved, over which the string output energy remains practically constant by further increasing the soil perimeter zones near to the string extremities, so that the perimeter effects become negligible. Moreover, by means of the mentioned upgraded model version, the latitude effects on bifacial and mono-facial PV strings, both fixed and with uniaxial horizontal solar tracker, were studied. We considered that such a study was a very interesting one, since, although in the literature several studies analyzed in-depth the tracker effects on the performance of traditional mono-facial PV system, only very few recent works tackled a similar analysis with reference to bifacial PV systems and further analysis on such an important subject were needed. Concerning the latter effects, the results of our study showed the following relevant facts. A bifacial PV string allows to produce significantly more energy than a mono-facial one, at the same installation conditions. Moreover, the adoption of the aforementioned type of solar tracker determines a clear advantage in terms of generated energy, compared to the fixed PV string. However, such an advantage decreases, by increasing the latitude (as consistent with the findings of other studies in the literature). According to our results, the energy gains achievable by using the considered solar tracker is greater for the case of a mono-facial PV string, compared to the case of a bifacial PV string. However, in this regard, it is important to recall that our model considers a tracking algorithm based on the irradiance optimization only on the module front side; by changing the tracking algorithm, so that an irradiance optimization also on the bifacial PV module rear sides can be obtained, it is possible that the energy produced by a bifacial PV system with tracker is increased. Finally, about the convenience to

install a uniaxial horizontal solar tracker to increase the energy production of a fixed PV system, a cost – benefit analysis is recommended case by case. However, based on the results presented in this work, it seems reasonable to speculate that for geographical locations at high latitudes, it could be convenient to install a fixed bifacial PV system, rather than adopting the mentioned type of solar tracker, to increase the energy produced compared to a fixed mono-facial PV system.

Regarding possible future development of this Ph.D. work, it should be noted that, among the relevant research activities thoroughly presented and discussed herein, currently those performed on bifacial PV devices are of great interest. In fact, at the moment such devices are having a considerable and fast development, and both the scientific community and the PV industry are showing an increasing interest toward the study of the bifacial PV system performance and behavior, aimed to clearly individuate installation conditions for the optimization of such performance. Actually, such a study represents an open field for research. In this context, although important results have already been achieved, we can individuate the following possible future development: on one hand, the refinement of the existing models for predicting the bifacial PV system electrical performance, so that their accuracy are further improved; on the other hand, the study, through adequate experimental tests, of the performance of real bifacial PV systems (both in absence and in presence of solar trackers), also with a view to further validate the mentioned models. Furthermore, as it was remarked before, an aspect studied in detail in the thesis first part concerned the instability phenomena in hydrogenated amorphous silicon. As we observed, such phenomena are due to the combination of two effects. Firstly, the Staebler - Wronski negative effect, determining an increase of point defect concentration promoting a recombination of charge carriers, hence reducing the efficiency of the PV modules. In addition, the positive annealing effect of the mentioned defects, which instead leads to the opposite effect of increasing module efficiency. Similar effects could also occur in amorphous Si / crystalline Si heterojunction bifacial PV cells and modules, which are a study subject at the CNR-IMM in collaboration with Enel Green Power. Therefore, another future development of this thesis work may concern this aspect.

REFERENCES

[1] U. Nations, 'Decade of Sustainable Energy for All 2014-2024,' 2014.

[2] UNFCCC, 2015, Adoption of the Paris Agreement, Decision 1/CP.21, United Nations Framework Convention on Climate Change, Bonn, Germany (https://unfccc.int/resource/docs/2015/cop21/eng/ l09r01.pdf) accessed 26 September 2018.

[3] EEA, 2018, Renewable energy in Europe-2018 Recent growth and knock-on effects No 20/2018, European Environment Agency (https://www.eea.europa.eu/publications/renewable-energy-in-europe-2018) published 18 December 2018.

[4] Directive 2009/28/EC of the European Parliament and of the Council of 23 April 2009 on the promotion of the use of energy from renewable sources and amending and subsequently repealing Directives 2001/77/EC and 2003/30/EC.

[5] https://ec.europa.eu/programmes/horizon2020/.

[6] Directive (EU) 2018/2001 of the European Parliament and of the Council of 11 December 2018 on the promotion of the use of energy from renewable sources.

[7] Frankfurt School-UNEP, 2018, Global trends in renewable energy investment 2018, Frankfurt School-UNEP Centre, Frankfurt am Main, Germany.

[8] IRENA, 2018, Renewable capacity statistics 2018, International Renewable Energy Agency (IRENA) (http://www.irena.org/publications/2018/Mar/Renewable-Capacity-Statistics-2018), Abu Dhabi.

[9] A. Busacca, F. Cardona, M. Caruso, M. Cellura, A. Cino, R. Miceli, A. Parisi, R. Pernice, F. Ricco Galluzzo, and F. Viola, "Electrical characterization of low power CIGSSe photovoltaic modules," in *2015 International Conference on Renewable Energy Research and Applications (ICRERA)*, 2015, pp. 1597–1602.

[10] B. Burger, K. Kiefer, and others, "©Fraunhofer ISE: Photovoltaics Report, updated: 27 August 2018," Fraunhofer Institute for Solar Energy Systems, ISE, 2018.

[11] M. A. Green, Y. Hishikawa, E. D. Dunlop, D. H. Levi, J. Hohl-Ebinger, and A. W. Y. Ho-Baillie, "Solar cell efficiency tables (version 52)," *Prog Photovolt Res Appl*, vol. 26, no. 7, pp. 427–436, Jan. 2019.

[12] C. H. Henry, "Limiting efficiencies of ideal single and multiple energy gap terrestrial solar cells," *Journal of Applied Physics*, vol. 51, no. 8, pp. 4494–4500, 1980.

[13] W. Shockley and H. J. Queisser, "Detailed Balance Limit of Efficiency of p-n Junction Solar Cells," *Journal of Applied Physics*, vol. 32, no. 3, pp. 510–519, 1961.

[14] S. P. Philipps, F. Dimroth, and A. W. Bett, "Chapter I-4-B - High-Efficiency III–V Multijunction Solar Cells," in *McEvoy's Handbook of Photovoltaics (Third Edition)*, Third Edition., S. A. Kalogirou, Ed. Academic Press, 2018, pp. 439–472.

[15] B. Shin, O. Gunawan, Y. Zhu, N. A. Bojarczuk, S. J. Chey, and S. Guha, "Thin film solar cell with 8.4% power conversion efficiency using an earth-abundant Cu2ZnSnS4 absorber," *Prog. Photovolt: Res. Appl.*, vol. 21, no. 1, pp. 72–76, Jan. 2013.

[16] A. Bongiovanni, A. Parisi, A. Ficicchia, G. Palmisano, L. Curcio, G. Calogero, and others, "Fabrication and Characterization of Dye-Sensitized Solar Cells," in *11th Symposium of European Vacuum Coaters - Anzio 2014 - Program & Abstracts (pp.25-25)*, 2014.

[17] M. A. Green and A. Ho-Baillie, "Perovskite Solar Cells: The Birth of a New Era in Photovoltaics," *ACS Energy Letters*, vol. 2, no. 4, pp. 822–830, 2017.

[18] K. Yoshikawa, H. Kawasaki, W. Yoshida, T. Irie, K. Konishi, K. Nakano, T. Uto, D. Adachi, M. Kanematsu, H. Uzu, and K. Yamamoto, "Silicon heterojunction solar cell with interdigitated back contacts for a photoconversion efficiency over 26%," *Nature Energy*, vol. 2, p. 17032, Mar. 2017.

[19] A. Metz, D. Adler, S. Bagus, H. Blanke, M. Bothar, E. Brouwer, S. Dauwe, K. Dressler, R. Droessler, T. Droste, M. Fiedler, Y. Gassenbauer, T. Grahl, N. Hermert, W.Kuzminski, A. Lachowicz, T. Lauinger, N. Lenck, M. Manole, M. Martini, R. Messmer, C. Meyer, J. Moschner, K. Ramspeck, P. Roth, R. SchÃ¶nfelder, B. Schum, J. Sticksel, K. Vaas, M. Volk, and K. Wangemann, "Industrial high performance crystalline silicon solar cells and modules based on rear surface passivation technology," *Solar Energy Materials and Solar Cells*, vol. 120, no. Part A, pp. 417–425, 2014.

[20] N. S. Pujari, G. Cellere, T. Falcon, and others, "International Technology Roadmap for Photovoltaic (ITRPV) Results 2017 including maturity report 2018 Ninth Edition, September 2018," ITRPV, 2018.

[21] A. Scuto, C. Gerardi, A. Battaglia, and S. Lombardo, "Effect of illumination and electric field intensity on the efficiency improvement of amorphous silicon tandem solar cells," *Journal of Vacuum Science & Technology B*, vol. 35, no. 1, p. 01A106, 2017.

[22] X. Deng and E. A. Schiff, "Amorphous Silicon–based Solar Cells," in *Handbook of Photovoltaic Science and Engineering*, A. Luque and S. Hegedus, Eds. Wiley, 2003, pp. 505–565.

[23] D. L. Staebler and C. R. Wronski, "Reversible conductivity changes in discharge-produced amorphous Si," *Applied Physics Letters*, vol. 31, no. 4, pp. 292–294, 1977.

[24] D. L. Staebler, R. S. Crandall, and R. Williams, "Stability of n-i-p amorphous silicon solar cells," *Applied Physics Letters*, vol. 39, no. 9, pp. 733–735, 1981.

[25] H. Fritzsche, "Development in Understanding and Controlling the Staebler-Wronski Effect in a-Si:H," *Annual Review of Materials Research*, vol. 31, no. 1, pp. 47–79, 2001.

[26] A. Scuto, C. Gerardi, A. Battaglia, A. Canino, and S. Lombardo, "Effect of field and pump light wavelength during DC stress on the efficiency improvement of amorphous silicon single junction and tandem solar cells," in *2017 IEEE International Reliability Physics Symposium (IRPS)*, 2017, p. 2F–3.1.

[27] A. Scuto, M. Foti, C. Gerardi, A. Battaglia, and S. A. Lombardo, "Improvement of solar cell performance and reversibility of ageing effects in hydrogenated amorphous silicon solar cells under illumination and electric field stress: Role of TCO and substrate," *2016 IEEE International Reliability Physics Symposium (IRPS)*, pp. 3C–3–1–3C–3–7, 2016.

[28] D. Carlson and K. Rajan, "Evidence for proton motion in the recovery of light-induced degradation in amorphous silicon solar cells," *Journal of Applied Physics*, vol. 83, pp. 1726–1729, 1998.

[29] D. E. Carlson and K. Rajan, "The reversal of light-induced degradation in amorphous silicon solar cells by an electric field," *Applied Physics Letters*, vol. 70, no. 16, pp. 2168–2170, 1997.

[30] A. Scuto, L. Valenti, S. Pierro, M. Foti, C. Gerardi, A. Battaglia, and S. Lombardo, "Data supporting the role of electric field and electrode material on the improvement of the ageing effects in hydrogenated amorphous silicon solar cells," *Data in Brief*, vol. 4, pp. 518–523, 2015.

[31] A. Scuto, L. Valenti, S. Pierro, M. Foti, C. Gerardi, A. Battaglia, and S. Lombardo, "Role of electric field and electrode material on the improvement of the ageing effects in hydrogenated amorphous silicon solar cells," *Solar Energy Materials and Solar Cells*, vol. 141, pp. 203–209, 2015.

[32] F. Ricco Galluzzo, A. Scuto, C. Gerardi, A. Battaglia, A. Canino, and S. Lombardo, "Performance increase of tandem amorphous/microcrystalline Si PV devices under variable illumination and temperature conditions," *Microelectronics Reliability*, vol. 88–90, 2018.

[33] S. H. Liu, E. J. Simburger, J. Matsumoto, A. Garcia III, J. Ross, and J. Nocerino, "Evaluation of thin-film solar cell temperature coefficients for space applications," *Prog. Photovolt: Res. Appl.*, vol. 13, no. 2, pp. 149–156, Feb. 2005.

[34] A. Virtuani, D. Pavanello, and G. Friesen, "Overview of Temperature Coefficients of Different Thin Film Photovoltaic Technologies," in *25th European Photovoltaic Solar Energy Conference and Exhibition/5th World Conference on Photovoltaic Energy Conversion*, 2010, pp. 4248–4252.

[35] T. Nakada, “Microstructural and diffusion properties of CIGS thin film solar cells fabricated using transparent conducting oxide back contacts,” *Thin Solid Films*, vol. 480–481, no. Complete, pp. 419–425, 2005.
[36] A. Romeo, G. Khrypunov, S. Galassini, H. Zogg, and A. Tiwari, “Bifacial configurations for CdTe solar cells,” *Solar Energy Materials and Solar Cells - SOLAR ENERG MATER SOLAR CELLS*, vol. 91, pp. 1388–1391, 2007.
[37] R. Guerrero-Lemus, R. Vega, T. Kim, A. Kimm, and L. E. Shephard, “Bifacial solar photovoltaics – A technology review,” *Renewable and Sustainable Energy Reviews*, vol. 60, pp. 1533–1549, 2016.
[38] X. Sun, M. R. Khan, C. Deline, and M. A. Alam, “Optimization and performance of bifacial solar modules: A global perspective,” *Applied Energy*, vol. 212, pp. 1601–1610, 2018.
[39] L. Yang, Q. H. Ye, A. Ebong, W. T. Song, G. J. Zhang, J. X. Wang, and Y. Ma, “High efficiency screen printed bifacial solar cells on monocrystalline CZ silicon,” *Prog. Photovolt: Res. Appl.*, vol. 19, no. 3, pp. 275–279, Mar. 2011.
[40] J.-T. Lin, K.-Y. Ho, S. W. Haga, and W.-H. Chen, “Symmetrical and Crossed Double-sided Passivation Emitter and Surface Field Solar Cells for Bifacial Applications,” *IEEE Journal of the Electron Devices Society*, vol. PP, pp. 1–1, 2018.
[41] A. Čampa, A. Valla, K. Brecl, F. Smole, D. Muñoz, and M. Topič, “Multiscale Modeling and Back Contact Design of Bifacial Silicon Heterojunction Solar Cells,” *IEEE Journal of Photovoltaics*, vol. 8, no. 1, pp. 89–95, Jan. 2018.
[42] https://news.panasonic.com/global/press/data/2014/04/en140410-4/en140410-4.html. 2014.
[43] M. Taguchi, A. Yano, S. Tohoda, K. Matsuyama, Y. Nakamura, T. Nishiwaki, K. Fujita, and E. Maruyama, “24.7% Record Efficiency HIT Solar Cell on Thin Silicon Wafer,” *IEEE Journal of Photovoltaics*, vol. 4, pp. 96–99, 2014.
[44] A. Luque, A. Cuevas, and J. M. Ruiz, “Double-sided n+-p-n+ solar cell for bifacial concentration,” *Solar Cells*, vol. 2, no. 2, pp. 151–166, 1980.
[45] H. Ohtsuka, M. Sakamoto, K. Tsutsui, and Y. Yazawa, “Bifacial silicon solar cells with 21·3% front efficiency and 19·8% rear efficiency,” *Prog. Photovolt: Res. Appl.*, vol. 8, no. 4, pp. 385–390, Mar. 2000.
[46] D. Brearley, “Bifacial PV Systems,” *SolarPro*, no. 10.2, Mar. 2017.
[47] A. Cuevas, A. Luque, J. Eguren, and J. del Alamo, “50 Per cent more output power from an albedo-collecting flat panel using bifacial solar cells,” *Solar Energy*, vol. 29, no. 5, pp. 419–420, 1982.
[48] K. Sugibuchi, N. Ishikawa, and S. Obara, “Bifacial-PV power output gain in the filed test using ‘earthON’ high bifaciality solar cells,” *Proc. 28th European Photovoltaic Solar Energy Conference*, pp. 4312–4317, 2013.
[49] U. Alper Yusufoglu, T. H. Lee, T. Pletzer, A. Halm, L. Koduvelikulathu, C. Comparotto, R. Kopecek, and H. Kurz, “Simulation of Energy Production by Bifacial Modules with Revision of Ground Reflection,” *Energy Procedia*, vol. 55, 2014.
[50] H. Mori, “RADIATION ENERGY TRANSDUCING DEVICE,” U.S. Patent 3.278.811Oct-1966.
[51] A. Cuevas, “The Early History of Bifacial Solar Cells,” in *20TH, European photovoltaic solar energy conference; 2005; Barcelona, Spain*, 2005, p. 2DO.3.1.
[52] J. P. Singh, A. ABERLE, and T. Walsh, “Electrical characterization method for bifacial photovoltaic modules,” *Solar Energy Materials and Solar Cells*, vol. 127, pp. 136–142, 2014.
[53] C. Deline, S. MacAlpine, B. Marion, F. Toor, A. Asgharzadeh, and J. S. Stein, “Assessment of Bifacial Photovoltaic Module Power Rating Methodologies—Inside and Out,” *IEEE Journal of Photovoltaics*, vol. 7, no. 2, pp. 575–580, Mar. 2017.
[54] I. Shoukry, J. Libal, R. Kopecek, E. Wefringhaus, and J. Werner, “Modelling of Bifacial Gain for Stand-alone and in-field Installed Bifacial PV Modules,” *Energy Procedia*, vol. 92, pp. 600–608, 2016.
[55] S. Guha, “Multijunction Solar Cells and Modules,” in *Technology and Applications of Amorphous Silicon*, R. Street, Ed. Springer-Verlag Berlin Heidelberg, 1999, pp. 252–305.

[56] H. M. Branz, "Hydrogen collision model: Quantitative description of metastability in amorphous silicon," *Phys. Rev. B*, vol. 59, no. 8, pp. 5498–5512, Feb. 1999.
[57] H. Fritzsche, "A New Perspective on an Old Problem: The Staebler-Wronski Effect," *MRS Proceedings*, vol. 1245, pp. 1245–A14–01, 2010.
[58] R. Biswas and Y.-P. Li, "Hydrogen Flip Model for Light-Induced Changes of Amorphous Silicon," *Phys. Rev. Lett.*, vol. 82, no. 12, pp. 2512–2515, Mar. 1999.
[59] J. A. Reimer and M. A. Petrich, "Structural Heterogeneities in Device-Quality Amorphous Hydrogenated Semiconductors," in *Amorphous Silicon and Related Materials*, U. H Fritzsche (University of Chicago, Ed. WORLD SCIENTIFIC, 1989, pp. 3–27.
[60] R. E. I. Schropp and M. Zeman, "Metastability," in *Amorphous and Microcrystalline Silicon Solar Cells: Modeling, Materials and Device Technology. Electronic Materials: Science & Technology, vol 5.*, Springer, Boston, MA, 1998, pp. 99–113.
[61] H. R. Park, J. Z. Liu, and S. Wagner, "Saturation of the light-induced defect density in hydrogenated amorphous silicon," *Applied Physics Letters*, vol. 55, no. 25, pp. 2658–2660, 1989.
[62] A. Lambertz, F. Finger, R. E. I. Schropp, U. Rau, and V. Smirnov, "Preparation and measurement of highly efficient a Si:H single junction solar cells and the advantages of μc-SiOx:H n-layers," *Progress in Photovoltaics: Research and Applications*, vol. 23, no. 8, pp. 939–948, 2015.
[63] G. A. Swartz, "Reverse bias and heat treatment to improve performance of a-Si solar cells," *Applied Physics Letters*, vol. 44, no. 7, pp. 697–699, 1984.
[64] D. Carlson, G. Lin, and G. Ganguly, "Temperature dependence of amorphous silicon solar cell PV parameters," in *Proceedings of the 28th IEEE Photovoltaic Specialists Conference*, 2000, pp. 707–712.
[65] A. Kolodziej, "Staebler-Wronski effect in amorphous silicon and its alloys," *Opto-electronics Review*, vol. 12, pp. 21–32, 2004.
[66] J. A. del Cueto and B. von Roedern, "Temperature-induced changes in the performance of amorphous silicon multi-junction modules in controlled light-soaking," *Prog. Photovolt: Res. Appl.*, vol. 7, no. 2, pp. 101–112, Apr. 1999.
[67] R. Rüther, G. Kleiss, and K. Reiche, "Spectral effects on amorphous silicon solar module fill factors," *Solar Energy Materials and Solar Cells*, vol. 71, no. 3, pp. 375–385, 2002.
[68] R. Gottschalg, D. G. Infield, and M. J. Kearney, "Experimental study of variations of the solar spectrum of relevance to thin film solar cells," *Solar Energy Materials and Solar Cells*, vol. 79, no. 4, pp. 527–537, 2003.
[69] R. P. Kenny, A. Ioannides, H. Müllejans, W. Zaaiman, and E. D. Dunlop, "Performance of thin film PV modules," *Thin Solid Films*, vol. 511–512, pp. 663–672, 2006.
[70] T. Minemoto, M. Toda, S. Nagae, M. Gotoh, A. Nakajima, K. Yamamoto, H. Takakura, and Y. Hamakawa, "Effect of spectral irradiance distribution on the outdoor performance of amorphous Si//thin-film crystalline Si stacked photovoltaic modules," *Solar Energy Materials and Solar Cells*, vol. 91, no. 2, pp. 120–122, 2007.
[71] J. C. Liu, C.-C. Lin, Y. Chen, C. T. Wu, C.-M. Fan, Y.-M. Wang, and C.-Y. Kung, "Enhancing Light-Trapping Properties of Amorphous Si Thin-Film Solar Cells Containing High-Reflective Silver Conductors Fabricated Using a Nonvacuum Process," *International Journal of Photoenergy*, vol. 2014, pp. 1–5, 2014.
[72] A. E. Ghitas, "Studying the effect of spectral variations intensity of the incident solar radiation on the Si solar cells performance," *NRIAG Journal of Astronomy and Geophysics*, vol. 1, no. 2, pp. 165–171, 2012.
[73] F. Ricco Galluzzo, C. Gerardi, A. Canino, and S. Lombardo, "Reversible Efficiency Variation of Tandem Amorphous/Microcrystalline Si Photovoltaic Modules in Outdoor Operation," *Energies*, vol. 12, no. 15: 2876, 2019.
[74] https://www.wunderground.com/.

[75] L. Kreinin, N. Bordin, A. Karsenty, A. Drori, D. Grobgeld, and N. Eisenberg, “PV module power gain due to bifacial design. Preliminary experimental and simulation data,” in *2010 35th IEEE Photovoltaic Specialists Conference*, 2010, pp. 2171–2175.
[76] U. A. Yusufoglu, T. M. Pletzer, L. J. Koduvelikulathu, C. Comparotto, R. Kopecek, and H. Kurz, “Analysis of the Annual Performance of Bifacial Modules and Optimization Methods,” *IEEE Journal of Photovoltaics*, vol. 5, no. 1, pp. 320–328, Jan. 2015.
[77] G. J. M. Janssen, B. B. V. Aken, A. J. Carr, and A. A. Mewe, “Outdoor Performance of Bifacial Modules by Measurements and Modelling,” *Energy Procedia*, vol. 77, pp. 364–373, 2015.
[78] C. W. Hansen, R. Gooding, N. Guay, D. M. Riley, J. Kallickal, D. Ellibee, A. Asgharzadeh, B. Marion, F. Toor, and J. S. Stein, “A Detailed Model of Rear-Side Irradiance for Bifacial PV Modules,” in *2017 IEEE 44th Photovoltaic Specialist Conference (PVSC)*, 2017, pp. 1543–1548.
[79] C. W. Hansen, D. M. Riley, C. Deline, F. Toor, and J. S. Stein, “A Detailed Performance Model for Bifacial PV Modules,” in *33rd EU PVSEC*, 2017.
[80] T. Katsaounis, K. Kotsovos, I. Gereige, A. Basaheeh, M. Abdullah, A. Khayat, E. Al-Habshi, A. Al-Saggaf, and A. E. Tzavaras, “Performance assessment of bifacial c-Si PV modules through device simulations and outdoor measurements,” *Renewable Energy*, vol. 143, pp. 1285–1298, 2019.
[81] “PVSYST PHOTOVOLTAIC SOFTWARE. Available online: https://www.pvsyst.com/help/bifacial_systems.htm.” .
[82] W. Xiao, W. G. Dunford, and A. Capel, “A novel modeling method for photovoltaic cells,” in *2004 IEEE 35th Annual Power Electronics Specialists Conference (IEEE Cat. No.04CH37551)*, 2004, vol. 3, pp. 1950–1956 Vol.3.
[83] R. Perez, P. Ineichen, R. Seals, J. Michalsky, and R. Stewart, “Modeling daylight availability and irradiance components from direct and global irradiance,” *Solar Energy*, vol. 44, no. 5, pp. 271–289, 1990.
[84] P. Ineichen, O. Guisan, and R. Perez, “Ground-reflected radiation and albedo,” *Solar Energy*, vol. 44, no. 4, pp. 207–214, 1990.
[85] R. Ibrahim and A. Afshin, “Solar position algorithm for solar radiation applications,” NREL National Renewable Energy Laboratory, TP-560-34302, 2008.
[86] B. Haurwitz, “INSOLATION IN RELATION TO CLOUDINESS AND CLOUD DENSITY,” *Journal of Meteorology*, vol. 2, no. 3, pp. 154–166, 1945.
[87] M. J. Reno, C. W. Hansen, and J. S. Stein, “Global horizontal irradiance clear sky models: implementation and analysis,” SANDIA, SAND2012-2389, Mar. 2012.
[88] J. F. Orgill and K. G. T. Hollands, “Correlation equation for hourly diffuse radiation on a horizontal surface,” *Solar Energy*, vol. 19, no. 4, pp. 357–359, 1977.
[89] N. Martin and J. M. Ruiz, “Calculation of the PV modules angular losses under field conditions by means of an analytical model,” *Solar Energy Materials and Solar Cells*, vol. 70, no. 1, pp. 25–38, 2001.
[90] R. G. Jr. Ross, “Flat-plate photovoltaic array design optimization,” in *14th Photovoltaic Specialists Conference*, 1980, pp. 1126–1132.
[91] D. Faiman, “Assessing the outdoor operating temperature of photovoltaic modules,” *Progress in Photovoltaics: Research and Applications*, vol. 16, no. 4, pp. 307–315, 2008.
[92] G. J. Ward, “The RADIANCE Lighting Simulation and Rendering System,” in *the 21st Annual Conference on Computer Graphics and Interactive Techniques, ACM*, 1994.
[93] “https://it.mathworks.com/products/matlab.html.” .
[94] S. A. Mousavi Maleki, H. Hizam, and C. Gomes, “Estimation of Hourly, Daily and Monthly Global Solar Radiation on Inclined Surfaces: Models Re-Visited,” *Energies*, vol. 10, no. 1, 2017.
[95] R. American Society of Heating and A.-C. Engineers, *ASHRAE handbook, 1985 fundamentals: an instrument of service prepared for the profession containing technical information ..*, no. 1 v. (various pagings). Atlanta, Ga.: the Society, 1985, p. 1 v. (various pagings).
[96] E. Lorenzo, “Energy Collected and Delivered by PV Modules,” in *Handbook of Photovoltaic Science and Engineering*, A. Luque and S. Hegedus, Eds. Wiley, 2003, p. 905.

[97] B. Liu and R. Jordan, “Daily insolation on surfaces tilted towards equator,” *ASHRAE J.; (United States)*, vol. 10, pp. 53–59, 1961.
[98] http://scienceworld.wolfram.com/physics/FresnelEquations.html.
[99] F. Fertig, S. Nold, N. Wöhrle, J. Greulich, I. Haedrich, K. Krauß, M. Mittag, D. Biro, S. Rein, and R. Preu, “Economic feasibility of bifacial silicon solar cells,” *Progress in Photovoltaics: Research and Applications*, vol. 24, 2016.
[100] GLOBAL SOLAR ATLAS. Available online: https://globalsolaratlas.info/.
[101] F. Ricco Galluzzo, A. Canino, C. Gerardi, and S. A. Lombardo, “A new model for predicting bifacial PV modules performance: first validation results,” in *46th IEEE Photovoltaic Specialists Conference (PVSC 46), CHICAGO, IL*, 2019.
[102] R. C. Neville, “Solar energy collector orientation and tracking mode,” *Solar Energy*, vol. 20, no. 1, pp. 7–11, 1978.
[103] S. Nann, “Potentials for tracking photovoltaic systems and V-troughs in moderate climates,” *Solar Energy*, vol. 45, no. 6, pp. 385–393, 1990.
[104] V. Poulek and M. Libra, “New solar tracker,” *Solar Energy Materials and Solar Cells*, vol. 51, no. 2, pp. 113–120, 1998.
[105] E. Lorenzo, M. Pérez, A. Ezpeleta, and J. Acedo, “Design of tracking photovoltaic systems with a single vertical axis,” *Progress in Photovoltaics: Research and Applications*, vol. 10, no. 8, pp. 533–543, 2002.
[106] S. Abdallah, “The effect of using sun tracking systems on the voltage–current characteristics and power generation of flat plate photovoltaics,” *Energy Conversion and Management*, vol. 45, no. 11, pp. 1671–1679, 2004.
[107] A. Al-Mohamad, “Efficiency improvements of photo-voltaic panels using a Sun-tracking system,” *Applied Energy*, vol. 79, no. 3, pp. 345–354, 2004.
[108] J. Bione, O. C. Vilela, and N. Fraidenraich, “Comparison of the performance of PV water pumping systems driven by fixed, tracking and V-trough generators,” *Solar Energy*, vol. 76, no. 6, pp. 703–711, 2004.
[109] K. S. Karimov, M. A. Saqib, P. Akhter, M. M. Ahmed, J. A. Chattha, and S. A. Yousafzai, “A simple photo-voltaic tracking system,” *Solar Energy Materials and Solar Cells*, vol. 87, no. 1, pp. 49–59, 2005.
[110] T. Tomson, “Discrete two-positional tracking of solar collectors,” *Renewable Energy*, vol. 33, no. 3, pp. 400–405, 2008.
[111] H. Mousazadeh, A. Keyhani, A. Javadi, H. Mobli, K. Abrinia, and A. Sharifi, “A review of principle and sun-tracking methods for maximizing solar systems output,” *Renewable and Sustainable Energy Reviews*, vol. 13, no. 8, pp. 1800–1818, 2009.
[112] C. S. Chin, A. Babu, and W. McBride, “Design, modeling and testing of a standalone single axis active solar tracker using MATLAB/Simulink,” *Renewable Energy*, vol. 36, no. 11, pp. 3075–3090, 2011.
[113] A. Bahrami, C. O. Okoye, and U. Atikol, “The effect of latitude on the performance of different solar trackers in Europe and Africa,” *Applied Energy*, vol. 177, pp. 896–906, 2016.
[114] H. Moradi, A. Abtahi, and R. Messenger, “Annual performance comparison between tracking and fixed photovoltaic arrays,” in *2016 IEEE 43rd Photovoltaic Specialists Conference (PVSC)*, 2016, pp. 3179–3183.
[115] S. D. Vaca J., F. Ordóñez, and C. Morales, “Improvements of Photovoltaic Systems by using Solar Tracking in Equatorial Regions,” in *33rd European Photovoltaic Solar Energy Conference and Exhibition*, 2017, pp. 2352–2357.
[116] A. Lindsay, M. Chiodetti, D. Binesti, S. Mousel, E. Lutun, K. Radouane, and J. Christopherson, “Modelling of Single-Axis Tracking Gain for Bifacial PV Systems,” in *32nd European Photovoltaic Solar Energy Conference and Exhibition*, 2016, pp. 1610–1617.
[117] S. A. Pelaez, C. Deline, P. Greenberg, J. S. Stein, and R. K. Kostuk, “Model and Validation of Single-Axis Tracking With Bifacial PV,” *IEEE Journal of Photovoltaics*, vol. 9, no. 3, pp. 715–721, May 2019.

[118] D. Berrian, J. Libal, M. Klenk, H. Nussbaumer, and R. Kopecek, “Performance of Bifacial PV Arrays With Fixed Tilt and Horizontal Single-Axis Tracking: Comparison of Simulated and Measured Data,” *IEEE Journal of Photovoltaics*, pp. 1–7, 2019.
[119] F. Ricco Galluzzo, P. Zani, M. Foti, A. Canino, C. Gerardi, and S. Lombardo, “Numerical Modeling of Bifacial PV String Performance: Perimeter Effect and Influence of Uniaxial Solar Tracker,” in course of submission in *Energies*, 2019.

APPENDIX A SCIENTIFIC PUBLICATIONS OF FABIO RICCO GALLUZZO DURING THE PhD PERIOD

A.1. Peer - Reviewed Publications

A.1.1. International Journals

- F. Ricco Galluzzo, P. Zani, M. Foti, A. Canino, C. Gerardi, and S. Lombardo, "Numerical Modeling of Bifacial PV String Performance: Perimeter Effect and Influence of Uniaxial Solar Tracker," in course of submission in *Energies*, 2019.

- F. Ricco Galluzzo, C. Gerardi, A. Canino, and S. Lombardo, "Reversible Efficiency Variation of Tandem Amorphous/Microcrystalline Si Photovoltaic Modules in Outdoor Operation," *Energies*, vol. 12, no. 15: 2876, 2019. Feature Paper and Cover of Energies published by CNR-IMM and EGP researchers. DOI: 10.3390/en12152876

- F. Ricco Galluzzo, A. Scuto, C. Gerardi, A. Battaglia, A. Canino, and S. Lombardo, "Performance increase of tandem amorphous/microcrystalline Si PV devices under variable illumination and temperature conditions," *Microelectronics Reliability*, vol. 88–90, pp. 1025–1029, 2018. DOI: https://doi.org/10.1016/j.microrel.2018.07.139

- A. Busacca, A. C. Cino, A. Parisi, R. Pernice, A. Salvini, A. Laudani, F. Ricco Galluzzo, and F. Riganti Fulginei, "One diode circuital model of light soaking phenomena in Dye-Sensitized Solar Cells," *Optik*, vol. 156, pp. 311–317, 2018. DOI: https://doi.org/10.1016/j.ijleo.2017.10.115

A.1.2. Conference Proceedings

- F. Ricco Galluzzo, A. Canino, C. Gerardi, and S. A. Lombardo, "A new model for predicting bifacial PV modules performance: first validation results," in *46th IEEE Photovoltaic Specialists Conference (PVSC 46), CHICAGO, IL*, 2019. To be published in IEEE *Xplore*. Conference program available online at: https://www.ieee-pvsc.org/PVSC46/program-technical.php

- F. Ricco Galluzzo, A. Scuto, C. Gerardi, A. Battaglia, A. Canino, and S. Lombardo, "Performance increase of tandem amorphous / microcrystalline Si PV devices under variable illumination and temperature conditions," in *ESREF 2018: 29TH EUROPEAN SYMPOSIUM ON RELIABILITY OF ELECTRON DEVICES, FAILURE PHYSICS AND ANALYSIS*, 2018. Conference program available online at: https://easychair.org/smart-program/ESREF2018/

- F. Ricco Galluzzo, L. Zumbo, G. Adamo, A. Parisi, M. Caruso, C. Gerardi, S. Lombardo, R. Miceli, and A. Busacca, "Electrical characterization of high-efficiency bifacial silicon solar cells," in *20th Italian National Conference on Photonic Technologies (Fotonica 2018)*, 2018. Conference program available online at:

https://convegni.aeit.it/fotonica/documenti/Fotonica2018_FinalProgramme.pdf. DOI: 10.1049/cp.2018.1678

- A. Parisi, R. Pernice, G. Adamo, R. Miceli, F. Ricco Galluzzo, A. C. Cino, and A. Busacca, "Anomalous electrical parameters improvement in Ruthenium DSSC," in *2018 Thirteenth International Conference on Ecological Vehicles and Renewable Energies (EVER)*, 2018. DOI: 10.1109/EVER.2018.8362353

- M. Caruso, R. Miceli, S. Guarino, F. Ricco Galluzzo, M. Roscia, and F. Viola, "Electrical characterization of CIGSSe photovoltaic modules," in *2017 6th International Conference on Clean Electrical Power (ICCEP)*, 2017. DOI: 10.1109/ICCEP.2017.8004788

- G. Adamo, A. Parisi, R. Pernice, F. Ricco Galluzzo, L. D. Noia, and A. C. Cino, "Laser Beam Induced Current measurements on Dye Sensitized Solar Cells and thin film CIG(S,SE)2modules," in *2017 6th International Conference on Clean Electrical Power (ICCEP)*, 2017. DOI: 10.1109/ICCEP.2017.8004810

A.2. Conferences

A.2.1. Invited Talk

- F. Ricco Galluzzo, L. Zumbo, C. Colletti, A. Canino, C. Gerardi, and S. Lombardo, "Bifacial Si heterojunction solar cells: impact of defects and optimization of bifaciality," *invited talk in Optical Microsystems OμS19*, 2019. Conference program available online at: https://www.europeanoptics.org/pages/events/capri/program/

- F. Ricco Galluzzo, A. Scuto, C. Gerardi, A. Battaglia, A. Canino, and S. Lombardo, "Performance improvement of tandem amorphous / microcrystalline si photovoltaic modules by voltage and temperature stress," *invited talk in FOTONICA 2018 AEIT – 20a Edizione CONVEGNO ITALIANO DELLE TECNOLOGIE FOTONICHE*, 2018. Conference program available online at: https://convegni.aeit.it/fotonica/documenti/Fotonica2018_FinalProgramme.pdf

A.2.2. Oral Presentations

- F. Ricco Galluzzo, A. Canino, C. Gerardi, and S. Lombardo, "Predictive Model of Bifacial PV Systems Performance," *in FisMat2019, University of Catania - September 30 - October 4*, 2019. Conference program available online at: https://eventi.cnism.it/fismat2019/submission/calendar

- F. Ricco Galluzzo, A. Scuto, C. Gerardi, A. Battaglia, A. Canino, and S. Lombardo, "Performance increase of tandem amorphous / microcrystalline Si PV devices under variable illumination and temperature conditions," in *ESREF 2018: 29TH EUROPEAN SYMPOSIUM ON RELIABILITY OF ELECTRON DEVICES, FAILURE PHYSICS AND ANALYSIS*, 2018. Conference program available online at: https://easychair.org/smart-program/ESREF2018/

- F. Ricco Galluzzo, L. Zumbo, G. Adamo, A. Parisi, M. Caruso, C. Gerardi, S. Lombardo, R. Miceli, and A. Busacca, "Electrical characterization of high-efficiency

bifacial silicon solar cells," in *20th Italian National Conference on Photonic Technologies (Fotonica 2018)*, 2018. Conference program available online at: https://convegni.aeit.it/fotonica/documenti/Fotonica2018_FinalProgramme.pdf. DOI: 10.1049/cp.2018.1678

A.2.3. Poster Presentations

- F. Ricco Galluzzo, A. Canino, C. Gerardi, and S. A. Lombardo, "A new model for predicting bifacial PV modules performance: first validation results," in *46th IEEE Photovoltaic Specialists Conference (PVSC 46), CHICAGO, IL*, 2019. Conference program available online at: https://www.ieee-pvsc.org/PVSC46/program-technical.php